Wrocław University of Technology
Centre of Advanced Materials and Nanotechnology

Materials Science

Nanotesting

Vol.21 • No. 3 • 2003

Oficyna Wydawnicza Politechniki Wrocławskiej

Materials Science is an interdisciplinary journal devoted to experimental and theoretical research into the synthesis, structure, properties and applications of materials.

Among the materials of interest are:

- glasses and ceramics
- sol-gel materials
- photoactive materials (including materials for nonlinear optics)
- laser materials
- photonic crystals
- semiconductor micro- and nanostructures
- piezo-, pyro- and ferroelectric materials
- high-T_c, superconductors
- magnetic materials
- molecular materials (including polymers) for use in electronics and photonics
- novel solid phases
- other novel and unconventional materials

The broad spectrum of the areas of interest reflects the interdisciplinary nature of materials research. Papers covering the modelling of materials, their synthesis and characterisation, physicochemical aspects of their fabrication, properties and applications are welcome. In addition to regular papers, the journal features issues containing conference papers, as well as special issues on key topics in materials science.

Materials Science is published under the auspices of the Centre of Advanced Materials and Nanotechnology of the Wrocław University of Technology, in collaboration with the Institute of Low Temperatures and Structural Research of the Polish Academy of Sciences and the Wroclaw University of Economics.

All accepted papers are placed on the Web page of the journal and are available at the address: http://MaterialsScience.pwr.wroc.pl

Editor-in-Chief

Juliusz Sworakowski

Institute of Physical and Theoretical Chemistry
Wrocław University of Technology
Wybrzeże Wyspiańskiego 27
50-370 Wrocław, Poland
sworakowski@pwr.wroc.pl

Associate **Editors**

Wiesław Stręk

Institute of Low Temperature
and Structure Research
Polish Academy of Sciences
P.O.Box 1410
50-950 Wrocław 2, Poland
strek@int.pan.wroc.pl

Jerzy Hanuza

Department of Bioorganic Chemistry
Faculty of Industry and Economics
Wrocław University of Economics
Komandorska 118/120
53-345 Wrocław, Poland
hanuza@credit.ae.wroc.pl

Scientific Secretary

Krzysztof Maruszewski
Intitute of Materials Science and Applied Mechanics
Wrocław University of Technology
Wybrzeże Wyspiańskiego 27
50-370 Wrocław, Poland
maruszewski@pwr.wroc.pl

Advisory Editorial Board

Michel A. Aegerter, Saarbrücken, Germany
Ludwig J. Balk, Wuppertal, Germany
Victor E. Borisenko, Minsk, Belarus
Mikhaylo S. Brodyn, Kyiv, Ukraine
Maciej Bugajski, Warszawa, Poland
Alexander Bulinski, Ottawa, Canada
Roberto M. Faria, São Carlos, Brazil
Reimund Gerhard-Multhaupt, Potsdam, Germany
Paweł Hawrylak, Ottawa, Canada
Jorma Hölsä, Turku, Finland
Alexander A. Kaminskii, Moscow, Russia
Wacław Kasprzak, Wrocław, Poland
Andrzej Kłonkowski, Gdańsk, Poland
Seiji Kojima, Tsukuba, Japan
Shin-ya Koshihara, Tokyo, Japan
Marian Kryszewski, Łódź, Poland
Krzysztof J. Kurzydłowski, Warsaw, Poland
Jerzy M. Langer, Warsaw, Poland
Janina Legendziewicz, Wrocław, Poland
Benedykt Licznerski, Wrocław, Poland
Tadeusz Luty, Wrocław, Poland
Joop H. van der Maas, Utrecht, The Netherlands
Bolesław Mazurek, Wrocław, Poland
Gerd Meyer, Cologne, Germany
Jan Misiewicz, Wrocław, Poland
Jerzy Mroziński, Wrocław, Poland
Robert W. Munn, Manchester, U.K.
Krzysztof Nauka, Palo Alto, CA, U.S.A.
Stanislav Nešpůrek, Prague, Czech Republic
Romek Nowak, Santa Clara, CA, U.S.A.
Tetsuo Ogawa, Osaka, Japan
Renata Reisfeld, Jerusalem, Israel
Marek Samoć, Canberra, Australia
Jan Stankowski, Poznań, Poland
Leszek Stoch, Cracow, Poland
Jan van Turnhout, Delft, The Netherlands
Jacek Ulański, Łódź, Poland
Walter Wojciechowski, Wrocław, Poland
Vladislav Zolin, Moscow, Russia

The journal is supported by the State Committee for Scientific Research

Editorial Office
Łukasz Maciejewski

Editorial layout
Hanna Basarowa

Printed in Poland

© Copyright by Oficyna Wydawnicza Politechniki Wrocławskiej, Wrocław 2003

Drukarnia Oficyny Wydawniczej Politechniki Wrocławskiej
Zam. nr 547/2003.

Contents

Nanotesting

J. Misiewicz, P. Sitarek, G. Sęk, R. Kudrawiec, Semiconductor heterostructures and device structures investigated by photoreflectance spectroscopy 263
J. Radojewski, P. Grabiec, Combined SNOM/AFM microscopy with micromachined nanoapertures 319
T. Gotszalk, P. Grabiec, I. W. Rangelow, Application of electrostatic force microscopy in nanosystem diagnostics 333
R. F. Szeloch, W. M. Posadowski, T. P. Gotszalk, P. Janus, T. Kowaliw, Thermal characterization of copper thin films made by means of sputtering 339
J. Kozłowski, J. Serafińczuk, A. Kozik, Wavelet shrinkage-based noise reduction from the high resolution X-ray images of epitaxial layers 345

Regular papers

N. V. Tristan, T. Palewski, H. Drulis, L. Folcik, S.A. Nikitin, Hydrogenation process of Gd_3Ni 357

Materials Science, *Vol. 21*, *No. 3*, *2003*

Semiconductor heterostructures and device structures investigated by photoreflectance spectroscopy

JAN MISIEWICZ[*], PIOTR SITAREK, GRZEGORZ SĘK, ROBERT KUDRAWIEC

Institute of Physics, Wrocław University of Technology,
Wybrzeże Wyspiańskiego 27, 50-370 Wrocław, Poland

In this review, we present the photoreflectance (PR) spectroscopy as a powerful tool for investigations of bulk semiconductors and semiconductor heterostructures. We discuss the application of PR technique to investigation of various properties of semiconductors, including the composition of multinary compounds, distribution of the built-in electric field and the influence of perturbations such as temperature, strain, pressure; low-dimensional structures such as quantum wells, multiple quantum wells and superlattices, quantum dots; and the structures of semiconductor devices like transistors and vertical/planar light emitting laser structures.

Key words: *photoreflectance; electric field; low-dimensional structures; semiconductor devices*

1. Introduction

Because of their novel physical properties and device applications, new materials and based on them semiconductor heterostructures such as quantum wells (multiple quantum wells, superlattices) and heterojunctions have been produced. To explore various physical properties of these materials and structures based on them, a number of characterisation methods, including photoluminescence (PL)[**], photoluminescence excitation (PLE) spectroscopy, transmission electron microscopy (TEM), X-ray techniques, Hall measurements, etc., have been applied. Most of the above-mentioned methods require special experimental conditions such as low temperatures (PL, PLE), or special sample preparation (TEM, Hall measurements). For practical applications, it is advantageous to use techniques, which are simple and at the same time provide a lot of valuable information. Such are electro-modulation spectroscopy techniques.

---

[*]Corresponding author, e-mail: Jan.Misiewicz@pwr.wroc.pl.
[**]See list of abbreviations, p. 301.

These methods were introduced in the sixties and were used in investigations of semiconductor band structure parameters in the seventies. We focus our attention on one particular contactless form of electric field modulation spectroscopy called photoreflectance (PR). Glembocki et al. in 1985 [1] reported the first application of photoreflectance to studies of semiconductor microstructures. Because of its extreme sensitivity to interband electronic transitions, many papers on this subject have been published since 1985. A number of review papers about the application of photoreflectance spectroscopy to the investigation of semiconductors and semiconductor structures have been published up to now [2–8].

In this paper, we present applications of the photoreflectance spectroscopy for investigations of bulk semiconductors, epilayers and low-dimensional semiconductor structures which provide studying and understanding the optical processes in semiconductor device structures. We start with a brief theoretical background to the technique and lineshape formulas associated with photoreflectance.

2. Principles of photoreflectance spectroscopy

Since its inception in the sixties, modulation spectroscopy has proven to be a powerful experimental technique for studying and characterization bulk semiconductors, reduced dimensional systems (surfaces, interfaces, quantum wells, wires and dots, etc.), actual device structures (transistors, lasers) and growth/processing. A derivative of an optical spectrum (i.e. of the reflectivity) with respect to some parameter is evaluated with any modulation spectroscopy. The measured optical signal depends on the joined density of states making this method sensitive to transitions at the critical point in the Brillouin zone of the material studied. The resulting spectrum has sharp, derivative-like features on a featureless background. Figure 1 shows the comparison of the reflectivity and electroreflectance spectra for bulk GaAs at 300 K [5, 9, 10]. While the reflectivity is characterized by broad features, the electroreflectance (ER) modulation spectrum is dominated by a series of very sharp lines with a zero signal as a baseline.

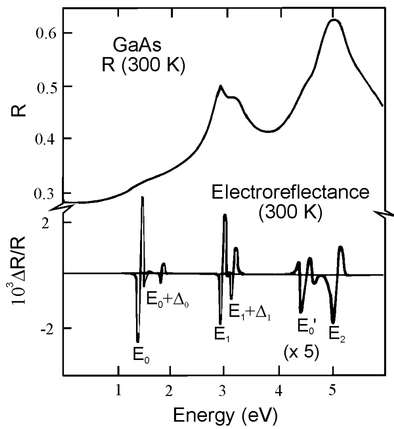

Fig. 1. Comparison of room-temperature reflectivity and electroreflectance of GaAs [5, 9, 10]

The modulation can easily be accomplished by varying some parameters, associated with the sample or the experimental system, in a periodic fashion and measuring the corresponding normalised change of the optical properties. It is possible to modulate a variety of parameters, i.e. the wavelength of light, temperature, stress applied or electric field in the sample studied. The electromodulation techniques are based on the modulation of the electric field. One of the electromodulation techniques is photoreflectance spectroscopy where the varying parameter is the internal (built in the structure) electric field.

In the PR, the modulation of the electric field in the sample is caused by photoexcited electron-hole pairs created by the pump source (usually laser) which is chopped with a given frequency. The photon energy of the pump source is generally above the band gap of the semiconductor being under study. There is a possibility to use a below band-gap modulation through the excitation of impurity or surface states [11]. The mechanism of the photo-induced modulation of the built-in electric field F_{DC} is explained in Fig. 2, for the case of an n-type semiconductor. Because of the pinning of the Fermi energy E_F at the surface, there exists a space-charge layer. The occupied surface states contain electrons from the bulk (Fig. 2a). Photoexcited electron–hole pairs are separated by the built-in electric field, with the minority carrier (holes in this case) being swept toward the surface. At the surface, the holes neutralize the trapped charge, reducing the built-in field from F_{DC} to F_{DC}-F_{AC}, where F_{AC} is a change in the built-in electric field (Fig. 2b).

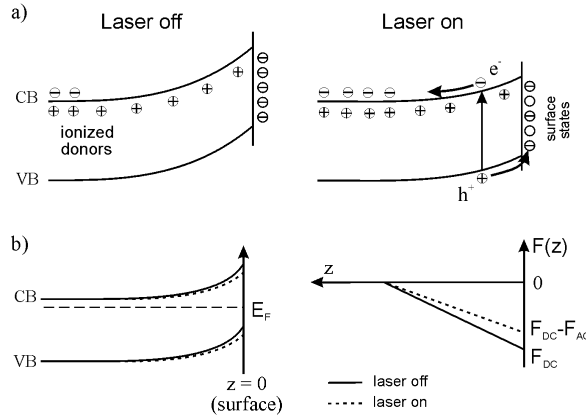

Fig. 2. Schematic representation of the photoreflectance effect (a), and the photoinduced changes in electronic bands and the surface bulit-in electric field (b), for an n-type semiconductor

In photoreflectance spectroscopy, relative changes in the reflectivity coefficient are measured. The changes we can define as

$$\frac{\Delta R}{R} = \frac{R_{\text{off}} - R_{\text{on}}}{R_{\text{off}}} \tag{1}$$

In the above expression R_{off} and R_{on} are the reflectivity coefficients, when the pump beam (laser) is off and on, respectively. These normalized changes can be related to the perturbation of the dielectric function ($\varepsilon = \varepsilon_1 + i\varepsilon_2$) expressed as [12]

$$\frac{\Delta R}{R} = \alpha(\varepsilon_1, \varepsilon_2)\Delta\varepsilon_1 + \beta(\varepsilon_1, \varepsilon_2)\Delta\varepsilon_2 \tag{2}$$

where α and β are the Seraphin coefficients, related to the dielectric function, and $\Delta\varepsilon_1$ and $\Delta\varepsilon_2$ are related by Kramers–Kronig relations.

We will discuss the lineshapes of the PR response in terms of electromodulation mechanisms. Electromodulation can be classified into three categories depending on the relative strengths of characteristic energies [13]. In the low-field regime $|\hbar\Omega| \le \Gamma$, where $\hbar\Omega$ is the electro-optic energy given by:

$$(\hbar\Omega)^3 = \frac{q^2\hbar^2F^2}{2\mu} \tag{3}$$

In the above equation, F is the electric field, μ is the reduced interband mass in the direction of the field. In the intermediate-field case, when $|\hbar\Omega| \ge \Gamma$ and $qFa_0 << E_g$ (a_0 is the lattice constant), the Franz–Keldysh oscillations (FKO) appear in the spectrum. In

the high-field regime the electro-optic energy is much greater than the broadening but $qFa_0 \approx E_g$ so that the Stark shifts are produced.

Recently, Pollak [5] as well as Glembocki and B.V. Shanabrook [2] provided a most detailed theoretical background of the photoreflectance technique.

2.1. Low field limit – third-derivative spectroscopy

Due to the modulation of the electric field, the perturbation destroys the translational symmetry of the crystal and hence can accelerate free charge carriers [14, 15]. In effect, under certain electric field conditions, the electromodulation results in sharp, third-derivative lineshapes.

For Lorenzian form of the dielectric function, low-field modulation, and under a parabolic band approximation, one can rewrite Eq. (2) as [13]

$$\frac{\Delta R}{R} = Re\left[A\,\mathrm{e}^{i\varphi}\left(E - E_g + i\Gamma\right)^{-m}\right] \tag{4}$$

where E_g is a band gap energy, Γ is the broadening parameter ($\Gamma \sim \hbar/\tau$), A and φ are the amplitude and phase factor, respectively. The parameter m in the lineshape factor of Eq. (4) depends on the type of the critical point. In a three-dimensional system, m equals 2.5, while for a two-dimensional critical point $m = 3$.

2.2. Low field limit – first-derivative spectroscopy

The perturbation due to the changes of the electric field does not accelerate charge carriers in their bound states such as excitons, quantum wells or impurities. These types of particles are confined in space which does not have a translational symmetry. For bound states, the photoreflectance lineshape has a first-derivative character [16], and the changes in the dielectric function may be expressed as

$$\Delta\varepsilon = \left[\frac{\partial\varepsilon}{\partial E_g}\frac{\partial E_g}{\partial F_{AC}} + \frac{\partial\varepsilon}{\partial\Gamma}\frac{\partial\Gamma}{\partial F_{AC}} + \frac{\partial\varepsilon}{\partial I}\frac{\partial I}{\partial F_{AC}}\right]F_{AC} \tag{5}$$

where F_{AC} is the change in the built-in electric field and I is the intensity of the optical transition. Equation (5) can be rewritten as [17]

$$\Delta\varepsilon_i = \left[A_E f_E^i + A_\Gamma f_\Gamma^i + A_I f_I^i\right]\frac{I}{\Gamma}F_{AC}, \quad i = 1, 2 \tag{6}$$

with

$$A_E = \frac{1}{\Gamma}\frac{\partial E_g}{\partial F_{AC}}, \qquad f_E^i = \frac{\partial \varepsilon_i}{\partial E_g}$$
$$A_\Gamma = \frac{1}{\Gamma}\frac{\partial \Gamma}{\partial F_{AC}}, \qquad f_\Gamma^i = \frac{\partial \varepsilon_i}{\partial \Gamma} \tag{7}$$
$$A_I = \frac{1}{I}\frac{\partial I}{\partial F_{AC}}, \qquad f_I^i = \frac{\partial \varepsilon_i}{\partial I}$$

Depending on the broadening mechanism (i.e. temperature), the unperturbated dielectric function can be either Lorenzian or Gaussian. For quantum wells, the dielectric function is excitonic, even at elevated temperatures. Thus for the quantum microstructures, the Lorenzian or Gaussian profiles of dielectric function are appropriate. The Lorenzian dielectric function can be written as [15]

$$\varepsilon = 1 + \frac{I}{E - E_g + i\Gamma} \tag{8}$$

The modulation terms of Eq. (6) are given by

$$f_E^1 = \frac{y^2 - 1}{\left(y^2+1\right)^2}, \quad f_\Gamma^1 = f_E^2, \quad f_I^1 = \frac{y}{y^2+1}$$
$$f_E^2 = \frac{-2y}{y^2+1}, \quad f_\Gamma^2 = -f_E^1, \quad f_I^2 = \frac{-1}{y^2+1} \tag{9}$$

where

$$y = \frac{E - E_g}{\Gamma} \tag{10}$$

If the intensity modulation terms are ignored, only two independent lineshape factors (see Eq. (9)) do not vanish. The combined spectral dependence can then be expressed by Eq. (4) with $m = 2$ [15].

The unperturbed dielectric function of a Gaussian profile is given by [17]

$$\varepsilon = 1 + I\left(L_1 + i\,L_2\right) \tag{11}$$

where

$$L_1 = \frac{y}{\Gamma}\Phi\left(1, 3/2, -y^2/2\right)$$
$$L_2 = \sqrt{\frac{\pi}{2}}\,\frac{1}{\Gamma}\exp\left(-y^2/2\right) \tag{12}$$

Φ is the confluent hypergeometric function. In this case, the modulation terms of Eq. (6) can be written as

$$\begin{aligned} f_E^1 &= -\Phi\left(1, 1/2, -y^2/2\right) \\ f_E^2 &= -\sqrt{\frac{\pi}{2}}\, y \exp\left(-y^2/2\right) \\ f_\Gamma^1 &= -2y\, \Phi\left(2, 3/2, -y^2/2\right) \\ f_\Gamma^2 &= -\sqrt{\frac{\pi}{2}}\left(y^2-1\right)\exp\left(-y^2/2\right) \\ f_I^1 &= y\, \Phi\left(1, 3/2, -y^2/2\right) \\ f_I^2 &= -\sqrt{\frac{\pi}{2}}\exp\left(-y^2/2\right) \end{aligned} \tag{13}$$

Hence, for the dielectric function of the Gaussian type one can get

$$\frac{\Delta R}{R} = \left[A f_E^1 + B f_E^2\right] \tag{14}$$

2.3. Intermediate field limit – Franz–Keldysh oscillations

When the low-field criteria are not satisfied, but $eFa_0 << E_g$, the dielectric function can exhibit the Franz–Keldysh oscillations. Although the exact form of $\Delta R/R$ for the intermediate-field case with the broadening is quite complicated, Aspnes and Studna [10] derived a relatively simple expression

$$\frac{\Delta R}{R} \propto \frac{1}{E^2\left(E-E_g\right)}\exp\left[-2\left(E-E_g\right)^{1/2}\frac{\Gamma}{(\hbar\Theta)^{3/2}}\right]\cos\left[\frac{4}{3}\frac{\left(E-E_g\right)^{3/2}}{(\hbar\Theta)^{3/2}}+\chi\right] \tag{15}$$

From the above equation, the position of an n-th extreme in the Franz–Keldysh oscillations is given by

$$n\pi = \frac{4}{3}\left[\frac{E_n - E_g}{\hbar\Theta}\right]^{3/2} + \chi \tag{16}$$

where E_n is the photon energy of the n-th extreme and χ is an arbitrary phase factor [18]. A plot $[4/(3\pi)](E_n - E_g)^{3/2}$ vs. the index number n will yield a straight line with the slope $(''\Omega)^{3/2}$. Therefore, the electric field F can directly be obtained from the period of FKO if μ is known. Conversely, μ can be measured if the electric field is known.

The dominant field in the structure determines the period of the FKO. In the above expressions the nature of that field was not specified. There are two limiting cases to be considered. If modulation is from a flat band, i.e. no presence of a DC field, then the field is clearly the modulating field F_{AC}. A more interesting situation occurs when there exists a large DC electric field in the material and a small modulating field is applied, i.e. $F_{AC} << F_{DC}$. In this case, the period of the FKO is given by F_{DC} and not by F_{AC} [19]. Shen and Pollak [19] even considered the case when F_{AC} is not small compared to F_{DC}. They have shown that even for F_{AC}/F_{DC} as large as 0.15 the first few FKO are still determined by F_{DC}.

3. Experimental details

In Figure 3, a schematic diagram of the photoreflectance apparatus is shown. The probe light is a monochromatic beam obtained from a quartz halogen lamp dispersed through a monochromator. This beam of intensity I_0 is focused on the sample. The laser (pumping) beam illuminates the same spot of the sample. The laser beam is chopped with the frequency of a few hundreds Hz. The photon energy of the pump source should be generally above the band gap of the semiconductor being investigated. A He-Ne laser (the energy range below 1.96 eV) or Ar^+ ion laser (the energy range below 4.5 eV) are used as typical pump sources. The intensity of the laser light can be adjusted by a variable, neutral density filter. The light reflected from the sample is detected by a photodiode or a photomultiplier. In order to prevent the detection of laser light, an appropriate longpass glass filter is used in front of the photodetector. The signal separator, connected to the detector, separates the signal into two components. The DC component is proportional to I_0R, and AC component is proportional to $I_0\Delta R$. The AC component is measured with a lock-in amplifier. A computer divides the AC signal by the DC component giving the photoreflectance spectrum, $\frac{\Delta R}{R}(''\omega)$, where $\hbar\omega$ is the photon energy of the incident beam.

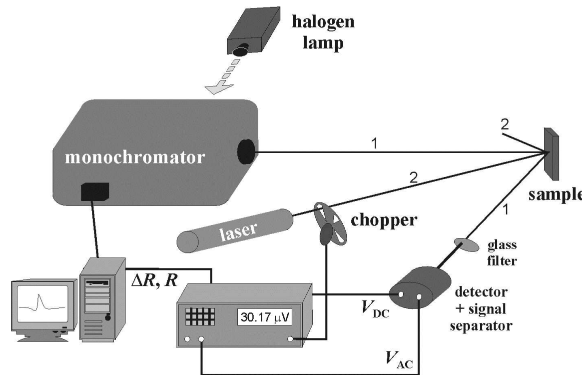

Fig. 3. Schematic diagram of the photoreflectance apparatus

In the case of photoreflectance, efficient filtering of the stray laser light is required, because it has the same frequency (chopped) as the signal of interest and can easily be detected. The scattered pump light can be reduced by means of an appropriate longpass filter in front of the detector. Furthermore, the laser illumination can produce a band-gap photoluminescence, which under certain conditions is more intense than the signal of interest. This problem can be eliminated by using long-focal-length optics or by using a second monochromator running in unison with the probe monochromator [20]. For a double monochromator, two scans are taken: one with the probe light on and one without it. Subtracting the two traces effectively eliminates the PL. An alternative technique involves using a dye laser as the probe beam and a detector placed sufficiently far away from the sample so as to reduce the PL, which is usually emitted isotropically [16, 21]. The spurious photoluminescence background signal can also be reduced or eliminated by approaches such as the use of double detector system [22], sweeping photoreflectance [23], or double pump beam method called differential photoreflectance [24].

4. Properties of semiconductor bulk and epilayers

A study of separated layers (or thin films) and its properties is a preliminary work to the investigation of more complicated structures (e.g. quantum wells, etc.) and, finally, semiconductor device structures. Here we will discuss the use of the photoreflectance spectroscopy to study bulk properties of semiconductors such as the composition of multinary semiconducting compounds, carrier concentration, distribution of the built-in electric field, the influence of perturbations like temperature and strain. Although a number of investigations have actually been performed on epitaxial (or thin) layers, the results do not explicitly depend on the nature of the films but they are the consequence of bulk properties.

4.1. Composition of alloys

One of the extremely important parameters of a semiconductor is the composition of binary A_xB_{1-x}, ternary $A_xB_{1-x}C$ or quaternary $A_xB_{1-x}C_yD_{1-y}$ alloys. The compositional variation of the fundamental transition (E_0) and/or features lying at higher energies (E_1) have been investigated by photoreflectance for a large number of alloys including, $Cd_{1-x}Mn_xTe$ (for $x \le 0.6$) at room and liquid helium temperatures [25], $Al_xIn_{1-x}P$ [26], $CuAl_xGa_{1-x}Se_2$ [27], $CuAl(S_xSe_{1-x})_2$ [28], ZnO on $ScAlMgO_4$ [29], $In_xGa_{1-x}N$ [30] and $Al_xGa_{1-x}As$, for $x \le 0.6$ [31, 32].

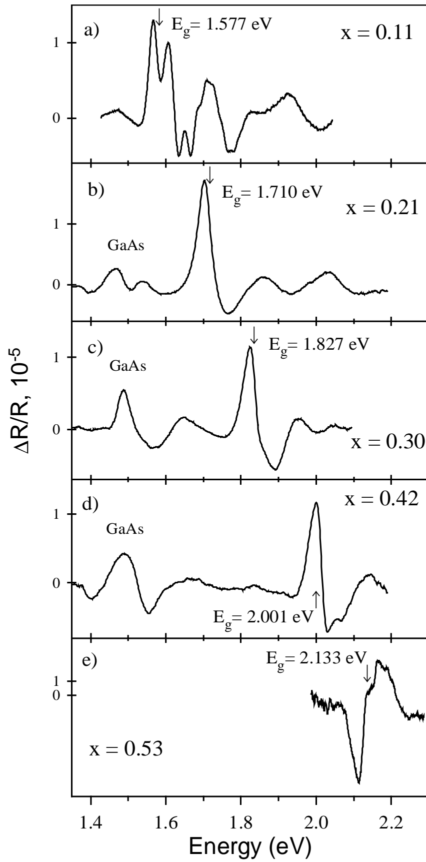

Fig. 4. Room-temperature PR spectra of $Al_xGa_{1-x}As/GaAs$ structures as a function of aluminium content x. Arrows mark the band gap energies of $Al_xGa_{1-x}As$ (after Sitarek et al. [32])

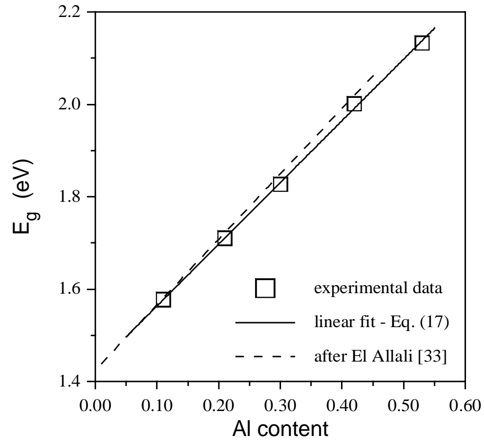

Fig. 5. The band gap energy of $Al_xGa_{1-x}As/GaAs$ vs. aluminium content from PR experiment (squares) (see Fig. 4). Solid line – linear approximation to the experimental data; dashed line – taken after [33] (after Sitarek et al. [32])

In Figure 4, the PR spectra obtained by Sitarek et al. [32] of several $Al_xGa_{1-x}As$ layers grown by MBE (molecular beam epitaxy) on GaAs substrates are shown vs. the aluminium content. The spectra are quite complicated because the Franz–Keldysh oscillations are present and also the signal related to the GaAs buffer is seen. Using the transition energies derived from the spectra, the dependence of the E_0^{AlGaAs} on the composition has been determined as

$$E_0(x) = (1.430 \pm 0.004) + (1.34 \pm 0.02)x \tag{17}$$

Equation (17) was compared with the literature data [33]. The comparison is presented in Fig. 5.

4.2. Carrier concentration

There are few reports on the application of the photoreflectance spectroscopy to the investigation of carrier concentration and relation between dopants concentration and free carrier concentration. Peters et al. [34] used the photoreflectance spectroscopy as a method for calibration of the n-type doping in Si-doped GaAs. Having studied the blue shift of the fundamental band gap of GaAs with the increasing doping concentration, they found a linear correlation between the dopant concentration and the value of the shift of the energy gap. They explained this effect as the result of the competition between the many-body effects and the Burstein–Moss effect related to the filling of the conduction band. Such an effect has also been observed in the n-type [35] and p-type [36] GaAs. Lee et al. [35] extended the results of Peters et al. [34] for Si -doped samples of concentrations from 1×10^{17} cm^{-3} up to almost 1×10^{19} cm^{-3}.

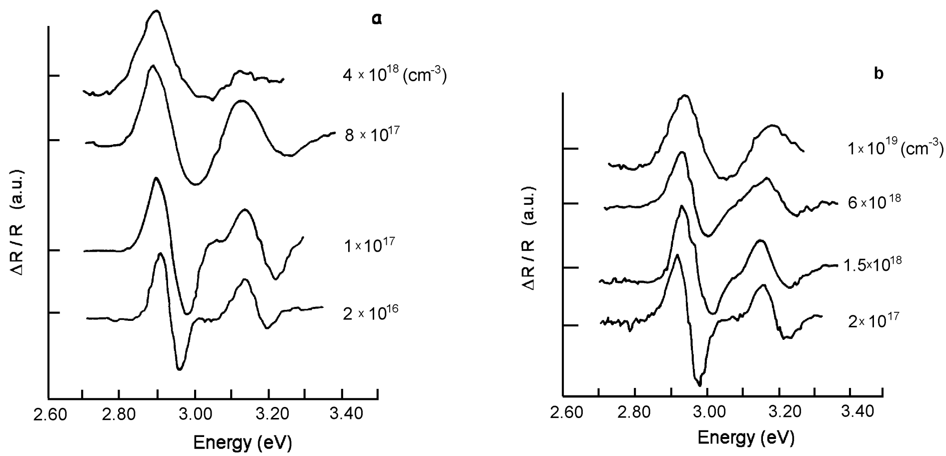

Fig. 6. PR response of GaAs as a function of carrier concentration:
a) for GaAs:Si; b) for GaAs:Zn (after Badakhshan et al. [38])

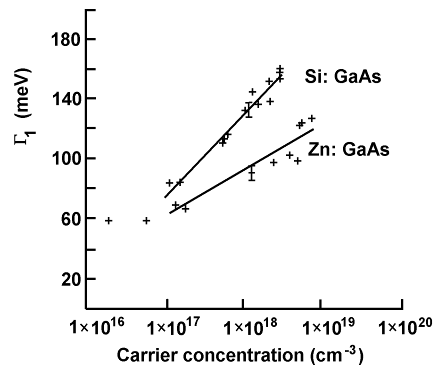

Fig. 7. The PR broadening parameter as a function of carrier concentration (after Badakhshan et al. [38])

Similar effects were investigated using PR for Si-doped GaN layers grown by the metal-organic chemical vapour deposition (MOCVD). In this case, a linear dependence between the fundamental gap transition energy and the cubic root of the carrier concentration has been found [37]. This red shift of the band gap with the increase of the level of Si doping has been fully explained by the many-body effects (the renormalisation of the band gap).

The effects of the carrier concentration manifest themselves not only at the fundamental band gap. Badakhshan et al. [38] investigated the PR spectra of MOCVD-grown GaAs:Si (n-type) and GaAs:Zn (p-type) layers in the range of E_1 and $E_1+\Delta$ transitions. They observed almost no shift in their energy but a very strong increase of the broadening parameter Γ_1 with the increase of the carrier concentration. In Fig. 6, the PR spectra as a function of doping concentration and doping type are shown. In Fig. 7, the linear dependence of broadening vs. logarithm of the carrier concentration is presented.

4.3. Temperature dependence

The temperature dependence of the energy and broadening parameter of the band gap of a semiconductor can be the source of different information about the scattering effects. The two most popular relations describing the temperature dependence of band gap are: the semiempirical Varshni expression [39]

$$E_0(T)=E_0(0)-\frac{\alpha T^2}{\beta+T} \tag{18}$$

and the Bose–Einstein expression [40, 41]

$$E_0(T)=E_0(0)-\frac{2a_B}{\exp(\Theta_B/T)-1} \tag{19}$$

where a_B represents the strength of the electron–average phonon interaction and Θ_B corresponds to an average phonon temperature. The temperature shift $E_0(T)$ contains contributions from both thermal expansion and electron–phonon coupling effects.

The variation of the linewidth (broadening parameter) with temperature can be also expressed by the Bose–Einstein type expression [40, 41]

$$\Gamma(T)=\Gamma(0)+\frac{\Gamma_{LO}}{\exp(\Theta_{LO}/T)-1} \tag{20}$$

The first term of this equation corresponds to the broadening mechanisms due to intrinsic lifetime, electron–electron interaction, impurity, dislocation and alloy scattering effects. The parameter Γ_{LO} is an electron–LO phonon coupling constant and Θ_{LO} is the LO phonon temperature.

The photoreflectance spectroscopy has been used to measure the temperature variation of the energy gap of GaAs [42, 43], InP [44], $Al_{0.18}Ga_{0.82}As$ [42, 45], $In_xGa_{1-x}As$ on GaAs for various values of x [46–49], $In_{0.53}Ga_{0.47}As$ on InP (also for the $E_0+\Delta_0$ transition) [50], $In_{0.515}Ga_{0.485}As$ on InP [51,52], GaSb, $In_xGa_{1-x}As_ySb_{1-y}$ on GaSb [53], CdTe [54], $Cd_{0.72}Mn_{0.28}Te$ [55], $Cd_{0.9}Mn_{0.1}Te$ [25], InAs [56], wurtzite-type GaN [57].

The temperature dependence of the fundamental band gap and broadening parameter of GaSb and $In_xGa_{1-x}As_ySb_{1-y}$ alloys between 14 and 377 K were studied by Muňoz et al. [53]. The four quaternary samples have the compositions (x, y): (0.07, 0.05), (0.09, 0.07), (0.12, 0.11), (0.22, 0.19). The values of $E_0(T)$ obtained from PR measurements for all samples being under study are shown by solid lines in Fig. 8. The quantity $E_0(T)$ was taken from the fit to the experimental data with the Varshni and Bose–Einstein expressions (Eqs. (18) and (19)). As a consequence of the above analysis, Muňoz et al. obtained the correct value (comparable with previous results) for $E_0(0)$ equal to 0.809 eV for GaSb and the corresponding ones for the quaternary compounds.

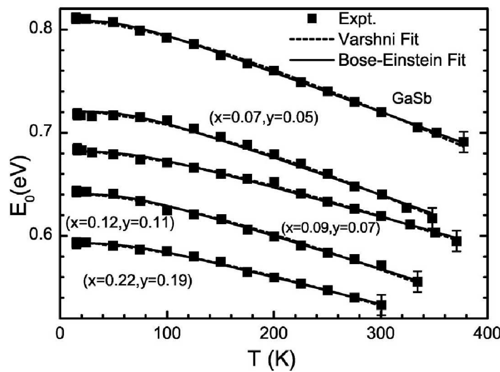

Fig. 8. Experimental values of $E_0(T)$ vs. T for different samples (solid squares); the (x, y) notation – the composition of the quaternary samples; the dashed and continuous lines – the fits according to the Varshni relation (Eq. (18)) and the Bose–Einstein (Eq. (19)) expression, respectively (after Muňoz et al. [53])

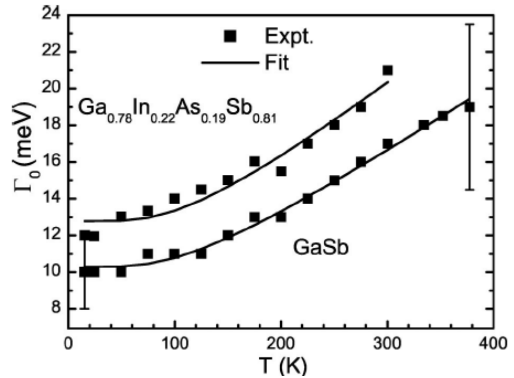

Fig. 9. $\Gamma_0(T)$ vs. T for the GaSb and $In_{0.22}Ga_{0.78}As_{0.19}Sb_{0.81}$ samples (solid squares); the solid lines are the fit according to the Bose–Einstein relation (Eq. (20)). Representative bars are shown (after Muňoz et al. [53])

In Figure 9, closed squares are the experimental values of $\Gamma_0(T)$ for the GaSb and $In_{0.22}Ga_{0.78}As_{0.19}Sb_{0.81}$ samples, respectively. Because of the error bars on the above data, it was necessary to fix the parameter Θ_{LO} in order to obtain two significant quantities $\Gamma_0(0)$ and Γ_{LO} by means of a least-squares fit using a the Bose–Einstein equation (Eq. (20)) – solid lines in Fig. 9.

4.4. Influence of strain

One of the main goals of strained-layer epitaxy is to create metastable thin films with properties different from those of the corresponding bulk materials. Typically, such films are pseudomorphic compound semiconductor structures grown from lattice-mismatch materials by molecular beam epitaxy (MBE) or by metal-organic chemical-vapour deposition (MOCVD). Such structures offer nearly complete flexibility in tailoring their electronic and optical properties and have proven to be highly successful in novel microelectronic and optoelectronic devices. This flexibility is enhanced by the possibility of pseudomorphic growth, where the lattice mismatch between the epilayer and substrate is accommodated by elastic strain. In fact, the in -plane biaxial strain, arising at the interface with the substrate, considerably affects the electronic structure and the optical response of the epilayer. It changes the band gaps, depending on the sign of the strain, reduces or removes the interband or intraband degeneracies (e.g., between the heavy and light hole valence bands at **k** = 0), and also reduces coupling between neighbouring bands.

Concerning the E_0 optical transitions at **k** = 0, the hydrostatic component of the strain shifts the energy gaps between the valence bands and the lowest lying conduction band. In addition, the uniaxial strain component splits the heavy (HH) and light (LH) hole valence bands. The resulting energy gaps between the conduction and the split valence bands are

$$E_0^{HH} = E_0 + \delta E_H - \frac{\delta E_S}{2} \tag{21}$$

$$E_0^{LH} = E_0 + \delta E_H + \frac{\delta E_S}{2} - \frac{(\delta E_S)^2}{2\Delta_0} \tag{22}$$

where

$$\delta E_H = 2a\frac{C_{11} - C_{12}}{C_{11}}\varepsilon \tag{23}$$

$$\delta E_S = 2b\frac{C_{11} + 2C_{12}}{C_{11}}\varepsilon \tag{24}$$

while C_{ij} are the elastic stiffness constants, a and b are the hydrostatic and shear deformation potentials, respectively and ε is the in-plane strain which is given by $\varepsilon = (a_S - a_L)/a_L$, where a_S and a_L are the lattice parameters of the substrate and layer, respectively. The valence band splitting, as measured from the optical spectra, is

$$\Delta E_{\mathrm{split}} = \delta E_S = 2b\frac{C_{11} + 2C_{12}}{C_{11}}\varepsilon \tag{25}$$

The PR spectra showing the heavy- and light-hole splitting generated by strain in GaAs layers deposited on Si substrates [58] are visible in Fig. 10. The quantity ΔE stands for the splitting between light (feature A) and heavy (feature B) hole bands. The value of the splitting increases on lowering the temperature. It has been explained on the base of the difference in the thermal expansion coefficients of GaAs and Si. From the value of the splitting energy expressed by Eq. (25), the value of the in-plane strain was estimated to be 0.12% being in agreement with the X-ray diffraction results.

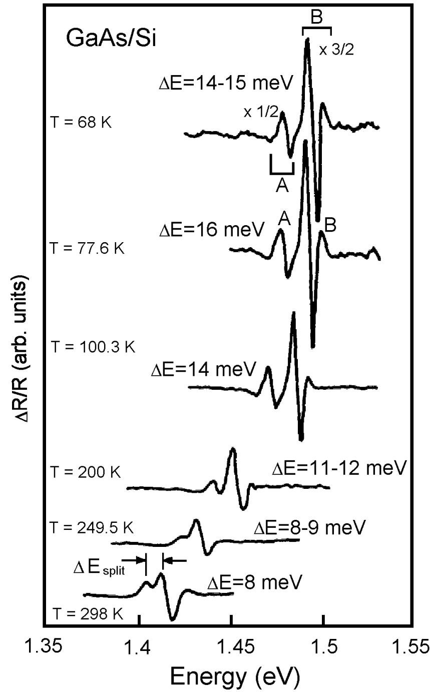

Fig. 10. PR spectra of strained GaAs on Si at several temperatures (after Glembocki [58]). A and B are the light and heavy hole transitions, respectively

The required strain-dependent properties can be achieved only by careful controlling the composition and the epilayer thickness, which should be lower than a critical value d_c to avoid relaxation via misfit dislocations which drastically degrade the layer quality and hence also the device performance. This problem has also been investigated by means of the photoreflectance spectroscopy for $In_xGa_{1-x}As$ layers grown by MOCVD on GaAs substrates [59, 60]. Sęk et al. determined the broadening parameter and the

PR amplitude of the band gap feature of the $In_xGa_{1-x}As$ for several samples with various indium contents and epilayer thicknesses. An example of the spectrum is shown in Fig. 11. The dependences of the broadening parameter and PR amplitude vs. Δd are shown in Figs. 12 and 13. The quantity Δd is defined as the difference between the nominal layer thickness (determined from the growth conditions and X-ray diffraction measurements) and its critical value (taken from the theoretical dependence of the critical thickness vs. indium content of $In_xGa_{1-x}As$ on GaAs [61]). A rapid increase of the broadening and decrease in the amplitude of the PR signal is observed at $\Delta d = 0$ due to the overcoming of the critical thickness and a strong degradation of the layer optical properties.

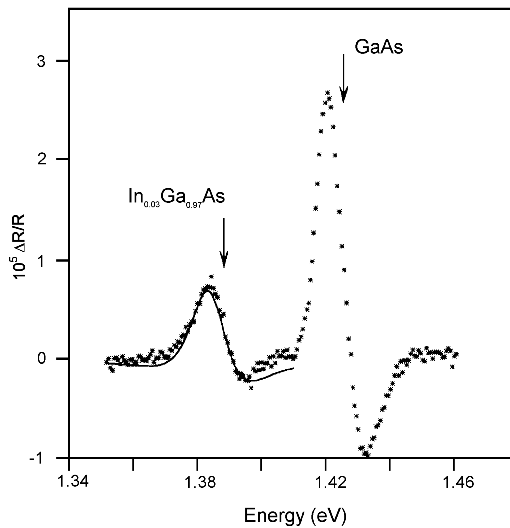

Fig. 11. Room-temperature PR spectrum of 100 nm thick strained $In_{0.03}Ga_{0.97}As$ layer on GaAs substrate (after Sęk et al. [60])

Lastras-Martinez et al. [62] report on photoreflectance-difference (PRD) measurements of n-type (001) GaAs crystals under uniaxial stress along [110]. The authors study the difference between two photoreflectance spectra, one measured with unpolarized light and the other with linearly polarized light along one of the symmetry axis of the crystal. The PRD spectra were recorded in the 2.6–3.6 eV energy range around the E_1 and $E_1+\Delta_1$ interband transitions of GaAs.

In general, PR spectra comprise, both linear electrooptic (LEO) and quadratic electro-optic (QEO) components, with this second component dominating the PR lineshape [62]. For light normally incident on the (001) surface of zinc blende crystal, nevertheless, the PRD spectrum comprises only a LEO component because the QEO term is isotropic for cubic symmetries. In addition to the previously reported LEO component [63], they have found a QEO component when stress is applied.

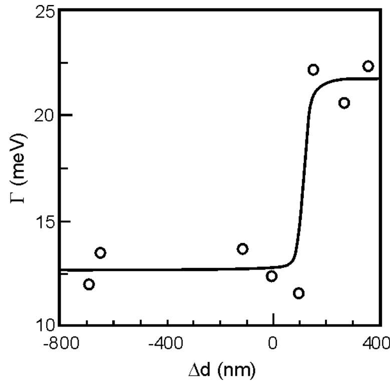

Fig. 12. The broadening parameter of the PR signal of several $In_xGa_{1-x}As$ layers on GaAs vs. Δd (after Sęk et al. [60])

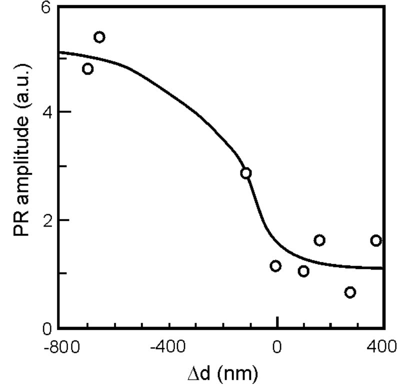

Fig. 13. The PR amplitude of several $In_xGa_{1-x}As$ layers on GaAs vs. Δd (after Sęk et al. [60])

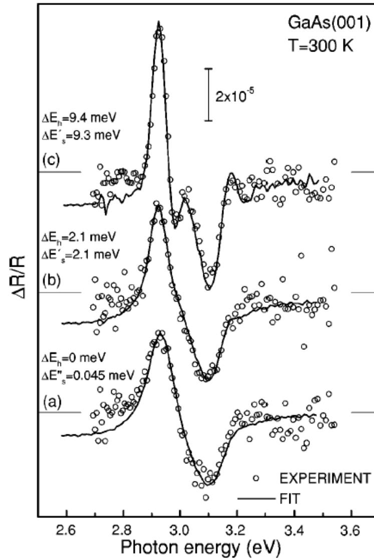

Fig. 14. Photoreflectance difference spectra of GaAs (001) (open circles) for: a) no applied stress and stresses, b) $X = -1\times10^8$ N/m^2, c) $X = -4.4\times10^8$ N/m^2. Solid lines are the fits obtained using adequate formula. The hydrostatic and splitting energy shifts obtained from the fits are also presented (after Lastras-Martinez et al. [62])

The PRD spectra are presented in Fig. 14. The open circles were obtained by subtracting polarized from unpolarized PR spectra for GaAs without strain (the lower spectrum) and with applied stress (two upper spectra). The solid lines are fits to PRD spectra with formula proposed by Lastras-Martinez et al. The QEO term is well resolved for a stress of $X = -4.4\times10^8$ N/m^2 and, in fact, it dominates the PRD spectrum. From the fitting to the PRD spectra, Lastras-Martinez et al. obtained the hydrostatic energy shifts $\Delta E_h = 2.1$ meV and $\Delta E_h = 9.4$ meV, for the spectra in Figs. 14b and c, respectively, and, additionally, the splitting energy shifts $\Delta E_s'' = 0.04$ meV, $\Delta E_s' = 2.1$ meV, and $\Delta E_s' = 9.3$ meV for the spectra in Figs. 14a–c, respectively.

The model proposed by Lastras-Martinez et al. [62] gives an excellent description of the evolution of the PRD spectra with a stress. The results presented give a further evidence that the PRD has its physical origin in a piezo-optic effect and help the development of PRD spectroscopy as a characterization tool of surface electric fields and piezo-optical properties of zinc blende semiconductors.

There is a number of reports on the PR investigations of strain effects in various material systems including: $In_xGa_{1-x}As/GaAs$ [64], $In_xGa_{1-x}As/InP$ [52], $In_xGa_{1-x}As/Al_{0.28}Ga_{0.72}As$ [65], InP/Si [66], ZnTe/GaAs [67], CdTe/GaAs [68], GaN on different substrates [69–74].

4.5. Built-in electric field

As was discussed earlier, the observation of the Franz–Keldysh oscillations in photoreflectance spectra allows the determination of the built-in electric field in the sample. If the sample consists of one or more epilayers on the substrate, the superposition of two or more PR signals from different depths of the structure is probable. It is possible to have different values of the internal electric field at the surface or at a particular interface because of the difference in the density of surface and interface states. If we extract the FKO related to surface or interface, we can independently determine the electric fields.

There are a few methods of the decomposition of PR signal into the surface and interface related contributions. The first one uses the fact that we have two signals from different depths in the sample. In the case of PR signal consisting of two subsignals: from the surface region and from the interface one, the etching procedure changed only one part of the signal measured. The PR subsignal from the interface is changed due to the change in the distance between the surface and interface. For such a case we can write

$$\left(\frac{\Delta R}{R}\right)_1 = \left(\frac{\Delta R}{R}\right)_S + A\left(\frac{\Delta R}{R}\right)_I \tag{26}$$

$$\left(\frac{\Delta R}{R}\right)_2 = \left(\frac{\Delta R}{R}\right)_S + B\left(\frac{\Delta R}{R}\right)_I \tag{27}$$

where 1 and 2 represent the PR signals measured for as-grown sample and after etching, respectively, and S and I mean the signal from the surface and interface, respectively. Following the relations (26) and (27), we can determine the subsignal from interface as the difference between the spectra measured for as-grown and etched samples [75–77]. This subsignal is given with the accuracy of a constant factor. It is sufficient because PR spectra are usually given in arbitrary units. Plotted in Fig. 15 is the example of the PR spectra for GaAs/SI-GaAs homojunction, before etching and

after two sequential etching procedures [76]. In Fig. 16, the decomposition into signals from the surface and from the interface is shown.

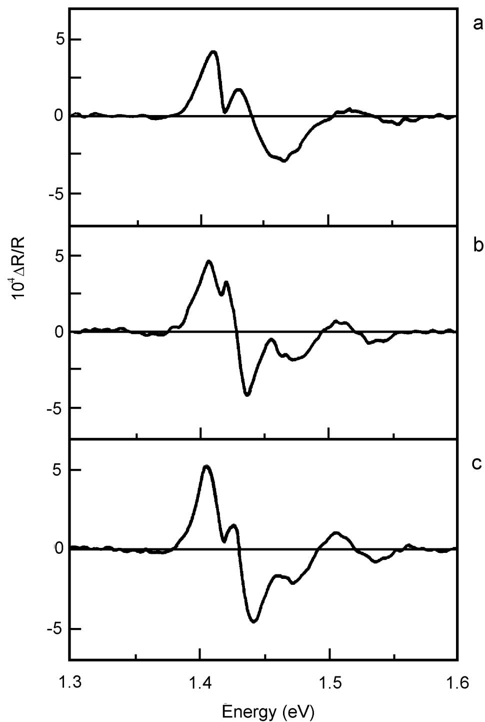

Fig. 15. PR spectra for an n-type GaAs/SI GaAs structure: a) before etching, b) after etching for 1 min, c) after next etching for 1 min (after Jezierski et al. [76])

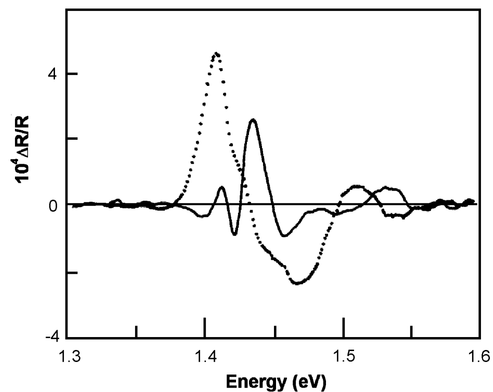

Fig. 16. PR spectra determined by the decomposition of the spectra shown in Fig. 14 into spectrum connected with the internal electric field in the surface region (dotted line) and the spectrum connected with the internal electric field in the interface region (solid line) (after Jezierski et al. [76])

An analogous method may be used in a non-destructive mode when the etching procedure is replaced by two PR measurements with two different wavelengths of the laser pump beam [32, 78–81]. In this case, the situation can be even simpler. If one of the spectra is measured using a very short wavelength of the laser, the signal comes only from the surface (parameter A in Eq. (26) is equal to zero). Then the subsignal from the interface can be obtained by taking the difference between PR signals obtained with longer and shorter laser wavelengths. The example of application of this method is shown in Fig. 17 for the case of $Al_{0.11}Ga_{0.89}As$ layer grown on GaAs substrate [32].

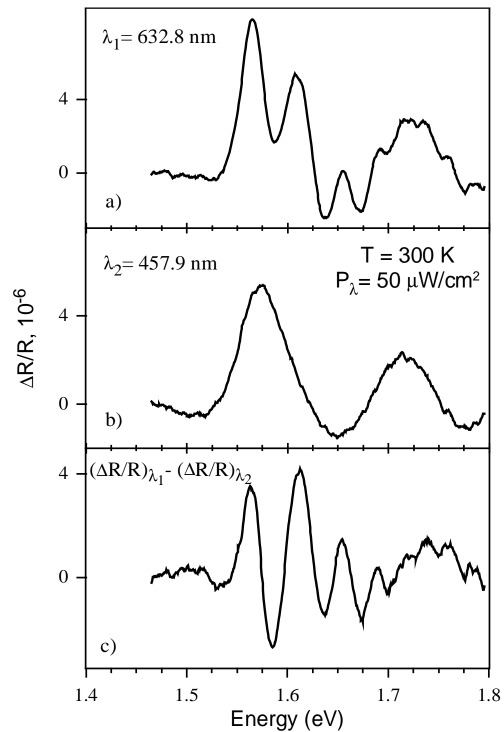

Fig. 17. PR spectra for $Al_{0.11}Ga_{0.89}As$ layers obtained with using the following pump beams: a) 632.8 nm line of the He-Ne laser, b) 457.9 nm line of the Ar^+ laser; c) the difference between the two former spectra giving the Franz–Keldysh oscillations connected with the electric field at the $Al_{0.11}Ga_{0.89}As$/GaAs inteface (after Sitarek et al. [32])

Another method of evaluating internal electric fields from the photoreflectance is the fast Fourier transformation (FFT) of the PR spectrum [82–88]. FFT is applied to the PR spectra in the energy region higher than the band gap energy to obtain the FKO period and than the electric field in the sample.

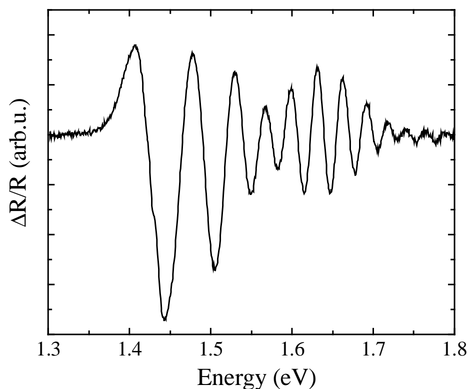

Fig. 18. Room-temperature PR spectrum of the δ-doped GaAs layer (after Nowaczyk et al. [88])

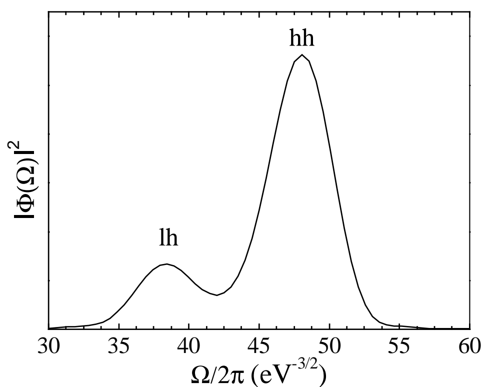

Fig. 19. Fast Fourier transform of the PR spectrum from Fig. 18 (after Nowaczyk et al. [88])

Nowaczyk et al. [88] investigated silicon delta doped (approx. 1×10^{12} cm^{-2}) GaAs MOVPE-grown layers on undoped GaAs substrate. Figure 18 shows the PR spectrum

for this δ-doped sample. A lot of well-distinguished Franz–Keldysh oscillations (more than 20 extrema) above the GaAs band gap energy are seen, demonstrating the existence of a strong uniform electric field in a high quality epitaxial layer. Fast Fourier transform has been applied to this PR spectrum in the energy region higher than the band gap to obtain the FKO period and then the internal electric field. Prior to the Fourier transformation, the experimental PR spectrum was renormalized. A new argument $z = (E - E_g)^{3/2}$ was chosen and then the spectrum was multiplied by $E^2(E - E_g)$ in order to deal with periodic functions and compensate the inherent damping of FKO, respectively. Then the Fourier transform of a new function

$$\gamma(z) = \frac{\Delta R}{R}(z)\left(E - E_g\right)E^2 \tag{28}$$

is calculated as follows

$$\Phi(\Omega) = \int_{z_1}^{z_2} \gamma(z)\exp\left(-i\Omega z\right)dz \tag{29}$$

where $z_1 = (E_1 - E_g)^{3/2}$ and $z_2 = (E_2 - E_g)^{3/2}$ are the left and right boundaries of the window for the Fourier transform. The frequency Ω is directly related to the magnitude of the electric field by

$$\Omega = \frac{4}{3(\hbar\Theta)^{3/2}} = \frac{4\sqrt{2}}{3\hbar q}\frac{\sqrt{\mu}}{F} \tag{30}$$

where $\hbar\Theta$ is defined by Eq. (3). The square of the modulus of the complex Fourier transform is plotted in Fig. 19. Ideally, each built-in electric field should produce two peaks in the FFT corresponding to light hole (lh) and heavy hole (hh) channels of the optical transitions, which is seen in our case.

The width of the peak is inversely proportional to the window selected for the FFT, i.e. to the range of the original PR spectrum. The built-in electric field determined for the GaAs sample, for both heavy and light hole frequencies, is 53 kV/cm. This allowed determining the potential barrier height V_B between the surface and the δ-doped region of the sample. The value of the potential barrier was found to be 0.74 V.

4.6. Influence of annealing, processing and growth

Photoreflectance spectroscopy has become an effective tool to study various process- and growth-induced effects [78, 79, 89–100]. Ga(As,N) presents a new class of semiconductors which are promising materials for optoelectronic devices such as lasers and detectors operating at 1.3 and 1.55 μm. In such an alloy the band structure decreases dramatically due to N incorporation.

Klar et al. [99] used the PR spectroscopy to study the electronic and lattice properties of GaN_xAs_{1-x} epitaxial layers before and after hydrogenation. Five GaN_xAs_{1-x} epitaxial layers with $x = 0.00043$, 0.00095, 0.0021, 0.005, and 0.019 and the thickness of 0.5 μm were grown on (100) GaAs substrates by MOVPE technique. The samples are unintentionally n-type doped. Pieces of all samples were hydrogenated by ion-beam irradiation from a Kaufman source with the sample temperature held at 300 °C.

Figure 20 shows the PR spectra of a GaN_xAs_{1-x} epitaxial layer with $x = 0.005$ before and after hydrogenation, together with the GaAs reference spectrum. The PR spectrum after hydrogenation shows the shift of the E_- band gap toward that of GaAs. The corresponding $E_- + \Delta_0$ band exhibits a comparable blue shift. The E_+ feature disappears after hydrogenation.

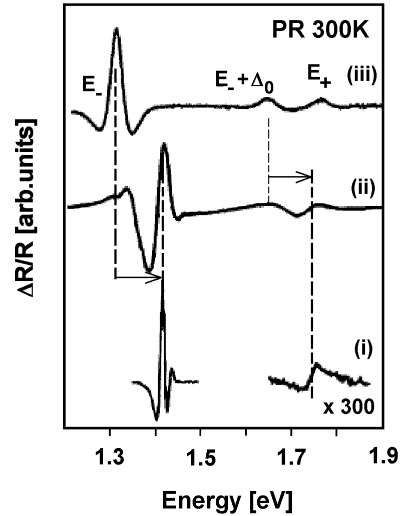

Fig. 20. PR spectra taken at $T = 300$ K of GaAs (i), $GaN_{0.005}As_{0.995}$ (ii) after hydrogenation, and $GaN_{0.005}As_{0.995}$ (iii) as grown (after Klar et al. [99])

The energy positions of the three signals before and after hydrogenation are summarized in Fig. 21. The solid lines are the fit of the level repulsion model to the experimental data. The dashed horizontal lines indicate the position of E_- and $E_- + \Delta_0$ in GaAs.

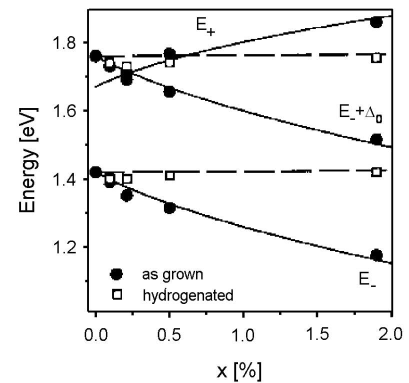

Fig. 21. Energy positions vs. N concentration x of the direct band gap E_-, the spin-orbit split-off band $E_- + \Delta_0$ and the N-induced E_+ band of the as-grown GaN_xAs_{1-x} samples (full circles). The solid lines are the fit of the level repulsion model to the experimental data. Corresponding data for E_- and $E_- + \Delta_0$ of the hydrogenated samples (open squares); there is no E_+ signal after hydrogenation. The dashed horizontal lines indicate the position of E_- and $E_- + \Delta_0$ in GaAs. $T = 300$ K (after Klar et al. [99])

Klar et al. [99] found that hydrogenation leads to an effective removal of the N-related perturbation due to the formation of a NH-complex. Hydrogenation literally reverses all the effects of N on the band structure of the GaAs host.

The influence of the carrier localization on modulation mechanism in photoreflectance of GaAsN and GaInAsN was investigated by Kudrawiec et al. [100]. They recorded the photoreflectance spectra of as-grown layers of GaAsN and GaInAsN from

10 to 300 K. Different modulation intensities and laser beam wavelengths were used. For the interpretation of PR data, the Kramers–Kronig analysis was employed. Kudrawiec et al. observed a decrease in PR signal with decreasing temperature and attempted to explain such a behaviour (observed by others as well) for the first time. They explain the above-mentioned effect as a weakening of the modulation efficiency induced by the carrier localization that has been evidenced earlier in alloys with diluted nitrogen.

5. Photoreflectance study of low-dimensional semiconductor structures

5.1. Quantum wells

Since the middle of sixties, the modulation spectroscopy techniques have proved their high applicability for studying and characterizing properties of bulk semiconductors. During the first decade, the method was recognized as a new, high-resolution technique for the solid state spectroscopy [13, 15, 101].

In the eighties, the modulation spectroscopy had a renaissance. The advantages exploited for bulk studies were applicable also in the semiconductor microstructures fabricated by MBE or MOCVD such as quantum wells (QWs), multiple quantum wells (MQWs) or superlattices (SLs). In 1985, Glembocki et al. [1] showed that multiple quantum wells, grown on semi-insulating substrates, could be studied by the photoreflectance technique.

Lineshape analysis, based on Eqs. (4), (14) and (15) (we will call it further fitting procedure) is an integral aspect of the photoreflectance spectroscopy. These procedures allow analysing complicated photoreflectance spectra in terms of theoretical parameters. Thus, the fitting provides valuable information about the energy gaps and linewidths associated with the optical transitions.

Photoreflectance spectra (dotted lines) of a GaAs/AlGaAs MQW structure (with the well width of 20 nm) at the temperatures of 6 K, 77 K and 150 K in the region of the 11H and 11L features [6, 21] are shown in Fig. 22. The solid and dashed lines are fits to the first-derivative of Lorenzian (first derivative Lorenzian lineshape – FDLL) and Gaussian (first derivative Gaussian lineshape – FDGL) profiles, respectively. At 6 K, the fit of the Lorenzian profile to the data is very good. At 77 K, the data cannot be adequately represented by either profile. An intermediate profile is required to fit the data. A Gaussian dielectric function results in a nearly perfect fit at 150 K.

For quantum wells, because of the enhanced exciton binding energy caused by the reduced dimensionality, the dielectric function has an excitonic character even at elevated temperatures, where the dielectric function broadening, caused by strong exciton–phonon interaction, impurities and defects, changes the absorption profile of excitons

from Lorenzian to Gaussian. Thus, at high temperatures, the Gaussian profile of the dielectric function must be used to fit the experimental data. At low temperatures, the Lorenzian dielectric function is more appropriate. Between 50 K and 150 K the transition from the Lorenzian to Gaussian profile is not abrupt and the lineshapes are of an intermediate form between Lorenzian and Gaussian. Equation (4) with the parameter m = 3 (2D critical point) sometimes is used to reflect the FDGL, providing a reasonable fit to the room-temperature experimental data.

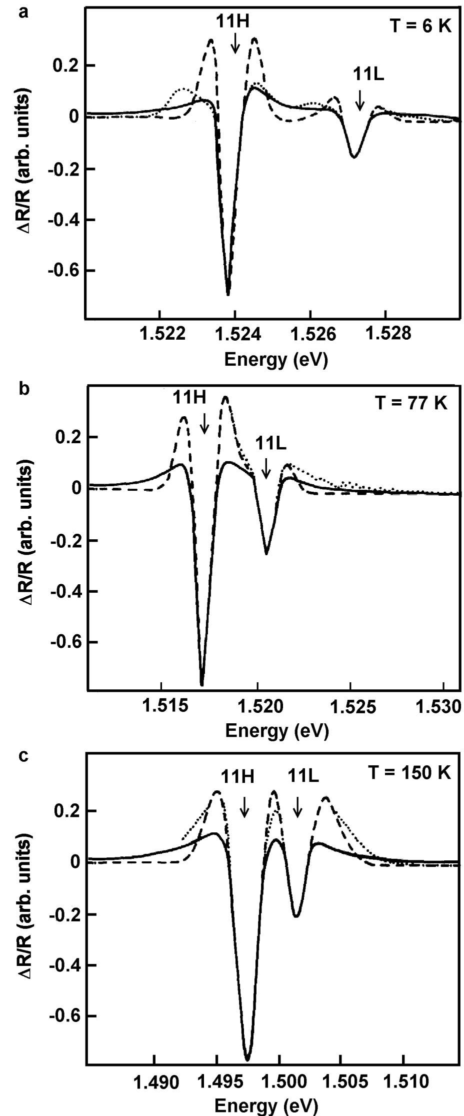

Fig. 22. Photoreflectance spectra (dotted line) at different temperatures from a GaAs/AlGaAs MQW structure. First-derivative Lorenzian (solid lines) and Gaussian (dashed lines) lineshapes are compared (after Glembocki [6])

At the beginning, single QW or MQW structures received most attention in PR studies. In MQW structures, the barrier layer is thick enough to prevent any significant wave function overlap between wells.

In addition to parity-allowed transitions ($m - n = 0, \pm 2, \pm 4, ...$), it has been shown that parity-forbidden transitions can be observed in QWs. The selection rules may be broken, i.e. by nonparabolicities in the valence band states and by electric field (internal and external).

Allowed and forbidden optical transitions in a GaAs/AlGaAs MQW structure were studied by Sitarek et al. [102]. The structure was grown by the MBE on (001) GaAs substrate. The MQW under investigations consisted of 60 periods of GaAs and $Al_{0.35}Ga_{0.65}As$ layers, each 15 nm thick. The PR spectrum measured at room-temperature had a very rich structure. In order to identify all features, a PR measurement was also carried out at a liquid nitrogen temperature. The PR spectrum obtained is shown in Fig. 23.

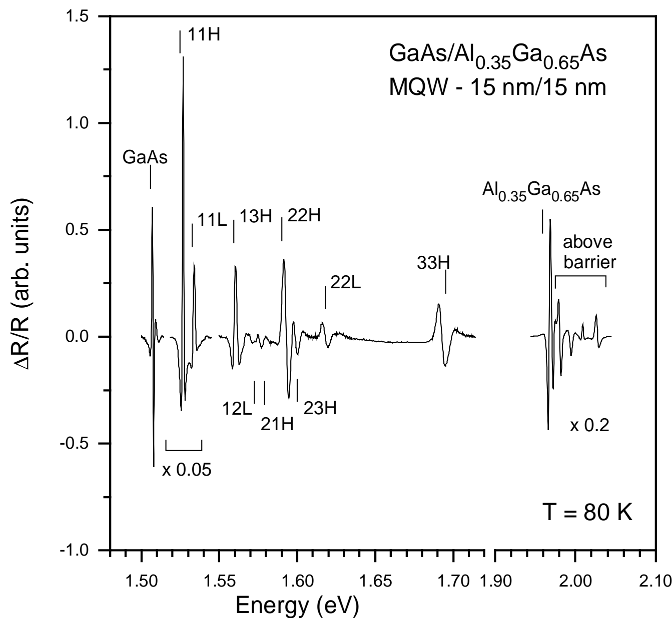

Fig. 23. Photoreflectance spectrum of $GaAs/Al_{0.35}Ga_{0.65}As$ MQW with wells and barriers of 15 nm width measured at 80 K. The vertical lines indicate optical transition energies obtained from the theoretical calculation (after Sitarek et al. [102])

The vertical lines indicate intersubband transitions. Both, the symmetry-allowed and symmetry forbidden transitions are marked in the figure. A small, built-in electric field is probably responsible for the presence of 21H, 23H and 21L symmetry-forbidden transitions in the spectrum, which are much weaker than the symmetry-allowed ones. Because of the finite depth of the well, the 13H transition is parity allowed and its in-

tensity is comparable to the symmetry-allowed transitions. Optical transitions involving unconfined states are present above the feature corresponding to the band gap of AlGaAs [103]. The energies of resonances present in the spectrum were accurately determined by Sitarek et al. through the fit of the first derivative Gaussian lineshape function (14) to the experimental data.

In order to identify the nature of the large number of intersubband transitions observed in the MQW, Sitarek et al. have performed a theoretical calculation based on the envelope function approximation [104]. The energy values obtained from this calculation agree very well with the experimental data.

The temperature dependence of both the energy and broadening of interband electronic transitions can yield important information about, e.g. electron–phonon interactions or excitonic effects. An increase of temperature leads to a red shift of the band gaps and an increase in the linewidth. The temperature variation of the energy gaps can be described by equations involving three parameters such as the Varshni expression or the more recently proposed term containing the Bose–Einstein occupation factor for phonons (Eqs. (18), (19)) [3]. A similar Bose–Einstein equation has also been used to fit the temperature dependence of the broadening function (Eq. (20)).

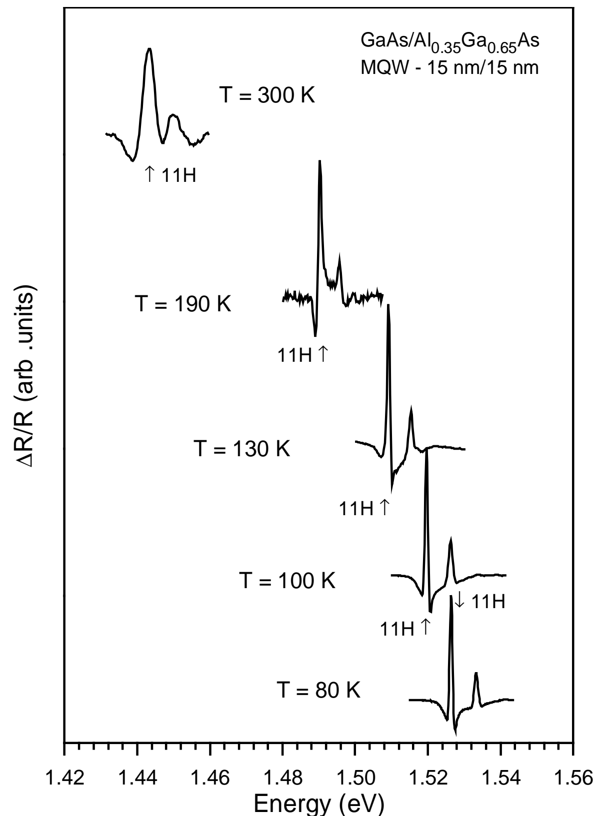

Fig. 24. The photoreflectance spectra of $GaAs/Al_{0.35}Ga_{0.65}As$ MQW structure in the energy range of 11H and 11L transitions measured at different temperatures. Their intensities are not in scale. Arrows mark 11H transition energy (after Sitarek et al. [102])

Sitarek et al. [102] have reported a study of the temperature dependence of PR spectra from $Al_{0.35}Ga_{0.65}As$/GaAs MQW in the 80–300 K temperature range. In Fig. 24, the PR spectra of the 11H and the 11L transitions at different temperatures are shown. From the least-squares fits to the experimental data with FDGL, the values of E_{11H} were obtained. The fit also yielded the broadening parameter Γ.

The parameters in the Bose–Einstein expression such as the strength of the electron–phonon interaction a_B, and Θ_B corresponding to the average phonon temperature, (see Eq. (19)) describe the temperature dependence of 11H transition energies of AlGaAs/GaAs MQW. The values of a_B and Θ_B obtained for 11H transition are very similar to the values for bulk GaAs. In the lattice matched AlGaAs/GaAs heterostructures, the temperature dependence of the band gap of the material forming the wells is the main factor affecting the relation of the transition energy and temperature.

The variation of the broadening parameter with temperature can also be expressed by the Bose–Einstein expression (see Eq. (20)). Parameter Γ_0 contains inhomogeneity contribution resulting from the interface roughness, alloy clustering and strain distribution (a small value of Γ_0 tells us that structure is very homogeneous). For the 11H transition, Sitarek et al. [102] found that $\Gamma_0 = 0.71$ meV.

In the studies of electronic and optical properties of quantum wells (and multiple quantum wells), the major attention was focused on confined states. In quantum well structures, the existence of energy levels formed above (below) the conduction (valence) band of the barriers has been observed in both low-temperature Raman spectroscopy [105] and low-temperature PLE spectroscopy [106]. Using photoreflectance spectroscopy, it is possible to investigate optical transitions involving unconfined states at room temperature [107, 108]. Up to now little work has been done on the study of such subbands.

The features observed at the energies higher than the resonance corresponding to bulk AlGaAs seen in Fig. 23 were under detailed study by Sitarek et al. [103]. A room -temperature PR spectrum for a $Al_{0.35}Ga_{0.65}As$/GaAs MQW with a 15 nm well width, is shown in Fig. 25 for the energies equal and higher than the band gap of the barrier energy. The feature at about 1.87 eV corresponds to the direct band gap of AlGaAs. Three additional features, marked A, B and C, were observed above the resonance related to AlGaAs band gap.

Sitarek et al. [103] reported energy level splitting in the optical transitions between unconfined electron and hole subbands in AlGaAs/GaAs MQWs. The splitting is associated with the energy dispersion in the direction along the MQW growth direction (z-axis). This dispersion leads to the formation of subbands in superlattices (and MQW structures). The width of the subband is determined by the energy difference between the quantized state at $k_z = 0$ (Brillouine zone centre) and $k_z = \pi/d$ (Brillouine zone edge). Here $d = L_W + L_B$ is the sum of the well thickness L_W and the barrier thickness L_B.

In order to obtain the transition energies between subbands, the third-derivative functional form (Eq. (4)) [109, 15] was used to fit the PR experimental data. The solid line in Fig. 25 shows the least squares fit to the TDFF.

The quasibound states at the above-barrier region in type-II ZnTe/CdSe superlattices were observed at room temperature by photoreflectance, contactless electroreflectance, as well as photoconductivity measurements by Tseng et al. [110]. They provide a concrete evidence for the strong localization of the carrier waves in the barrier region. It was found that the barrier-width dependence of the above-barrier ground-state transition energies can be well described by the constructive interference condition. Tseng et al. observed the absorptive spatially indirect transition between electrons confined in the CdSe and holes confined in the ZnTe layers.

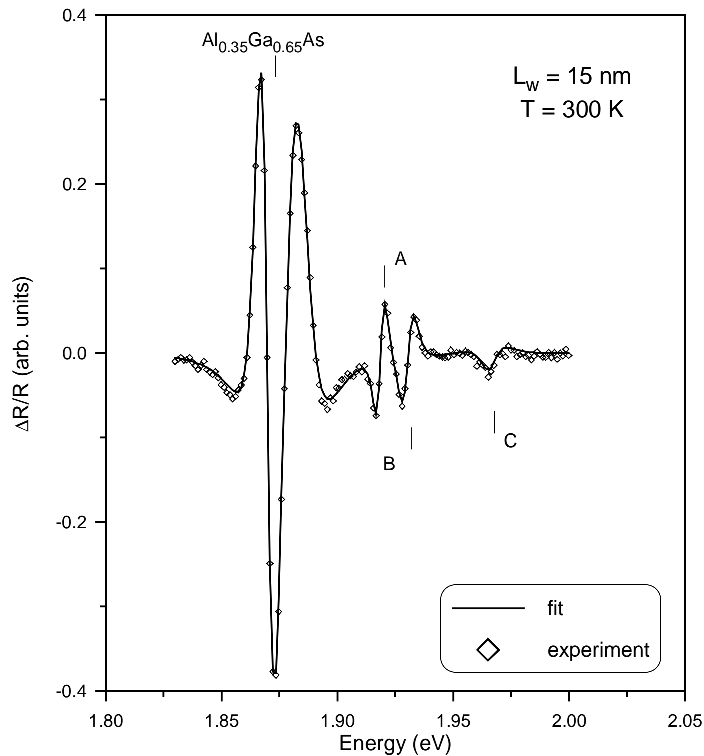

Fig. 25. Photoreflectance spectrum of GaAs/$Al_{0.35}Ga_{0.65}As$ MQW structure in the range above the barrier transitions. Solid line is the fit according to Eq. (4). Vertical lines mark the energies of optical transitions involving unconfined states (after Sitarek et al. [103])

In strained systems, the properties of the electron and hole quantum states depend on both the strain and quantum confinement. It is useful to define the conduction band offset parameter

$$Q_C = \frac{\Delta E_C}{\Delta E_C + \Delta E_V^{HH}} \tag{31}$$

where ΔE_C and ΔE_V^{HH} are the conduction band and the heavy-hole valence band discontinuities, respectively. When thin InGaAs layers are grown on a AlGaAs buffer layer, a biaxial in-plane compression and a corresponding extension (tensile strain) along the growth direction are sustained in InGaAs. Such a strain alters the band structure of InGaAs [111]. The energy band gap increases due to the compressive hydrostatic component of the strain while the tensile, (001) uniaxial strain splits the heavy-light hole degeneracy at the Brillouine zone centre. The relative positions of the bands in the InGaAs/GaAs QWs can lead to two possible configurations of the potential of the well. If the conduction band offset parameter Q_C is less than 0.5, both the electrons and the holes are confined to the InGaAs region. In the other case ($Q_C > 0.5$), the electrons and the heavy holes are in the InGaAs region (configuration of type I), while the light holes are in the GaAs region (configuration of type II).

Sęk et al. [112] studied the InGaAs/GaAs QW structure grown by MOCVD. The structure consisted of five 10 nm $In_{0.115}Ga_{0.885}As$ quantum wells separated with 80 nm GaAs barriers. They also concluded that light holes are confined in GaAs layer configuration of type II.

Because of their potential applications for long-wavelength optoelectronic devices, e.g. high-performance laser diodes emitting at the 1.3 and 1.55 μm optical fibre window, narrow band-gap semiconductors and especially low-dimensional structures based on such semiconductors are widely investigated.

A recent increase in interest in QW structures operating in the 1.3–1.55 μm spectral region caused an increase in applications of the post-growth techniques that produce non-square QWs, for the modification of the operation wavelength of well-known InP-based laser structures. The InGaAsP/InP laser structures grown by gas source MBE have been investigated by Kudrawiec et al. [113]. The structures were modified using the rapid thermal annealing (RTA) technique. The migration of atoms across quantum well interfaces (during RTA) changes the quantum well profile from a square to a rounded well and is responsible for that blue shift (in comparison to as-grown structure) of all optical transitions observed in PR. Thus using RTA (or other techniques) enables tuning the laser structure to a proper wavelength.

Another alloy which may be used for the construction of long-wavelength optoelectronic devices is the quaternary alloy InGaAsN. Compared to the InGaAsP quantum well system, GaInAsN/GaAs QW's have a larger conduction band offset which leads to a stronger electron confinement and hence higher characteristic temperatures. The high-temperature performance of GaInAsN-based laser diodes is expected to be better than that of InGaAsP devices. Due to its possible applications GaInAsN/GaAs QWs have been widely investigated in recent years (see for example [114–119]).

The $In_xGa_{1-x}Sb/GaSb$ strained system has potential applications for example in: trace gas sensing, atmospheric pollution and drug monitoring, medical procedures such as laser surgery and medical diagnostic, absorption spectroscopy or long-haul telecommunications, and especially low threshold current lasers at wavelengths ranging from 1.5 to 2.2 μm.

Single quantum well $In_{0.22}Ga_{0.78}Sb/GaSb$ structure grown by MBE on GaSb substrate was investigated by Kudrawiec et al. [120]. Figure 26 shows a comparison of photoluminescence, reflectance, photoreflectance, transmittance and phototransmittance spectra of a $In_{0.22}Ga_{0.78}Sb/GaSb$ single quantum well recorded at T = 10 K. In the PL spectrum, three peaks are observed. Two high-energy peaks (at 0.776 and 0.790 eV) are GaSb defect-related and were previously observed in GaSb-based quantum well structures. The third, dominating, very narrow (3.5 meV) peak at 0.691 eV, labelled 1C-1HH, originates from the quantum well and represents ground-state heavy-hole exciton radiative recombination. In reflectance spectrum only a feature associated with GaSb band gap exciton (in the buffer and/or cap layer) is clearly observed. Only a very weak trace of the quantum well-related signal is seen. On the contrary, strong and well-resolved features are observed in the photoreflectance and phototransmitance (PT) spectra below the GaSb band gap energy.

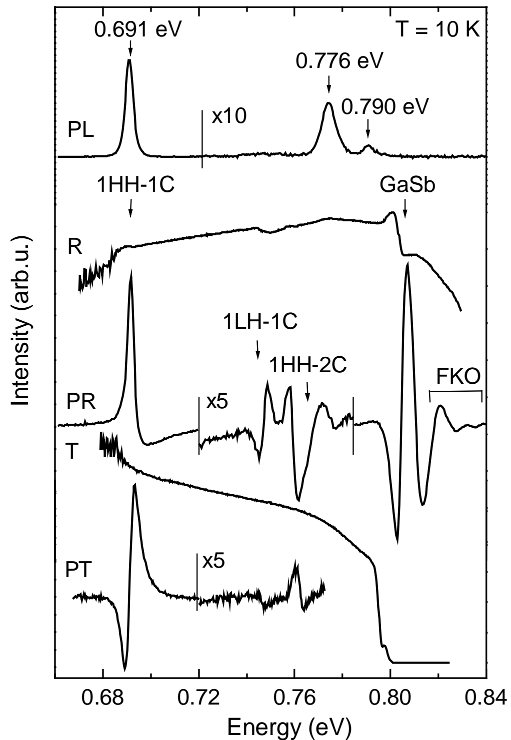

Fig. 26. Comparison of photoluminescence (PL), reflectance (R), photoreflectance (PR), transmittance (T) and phototransmittance (PT) spectra of $In_{0.22}Ga_{0.78}Sb/GaSb$ single quantum well at 10 K (after Kudrawiec et al. [120])

Due to the transparence of the GaSb substrate for light of wavelengths longer than 1.55 μm (at 10 K), it was possible to carry out the photomodulation spectroscopy experiments in reflection and transmission modes and both techniques appeared to probe the single $In_{0.22}Ga_{0.78}Sb$ quantum well. In both derivative spectra (PR and PT), the same quantum well-related transitions are observed. There is only one important difference between photoreflectance and phototransmittance and hence also between their spectra. In PR, a strong GaSb-related feature is seen in the shape of the Franz–Keldysh oscillations, reflecting the existence of a weak built-in electric field at the surface of GaSb or at GaSb buffer–GaSb substrate interface. It is impossible to observe such a signal in PT spectrum due to the strong absorption in the GaSb substrate which starts to increase significantly when the photon energy of the probe beam approaches the energy of GaSb band gap (0.8 eV).

In terms of device applications, wide band-gap semiconductors are very important, especially for so-called "blue optoelectronics". Wetzel et al. [121, 122] have performed enhanced studies of multiple quantum well $In_xGa_{1-x}N$/GaN systems using photoreflectance spectroscopy.

As long as the barriers in multiple quantum wells structure are thick, the coupling between the wells does not occur. The simplest structure containing coupled QWs is double quantum well (DQW). Sęk et al. [123] studied undoped symmetric structure with two GaAs/AlGaAs quantum wells separated by an AlAs mono-layer (ML). The structure was grown by the MBE on a (001) semi-insulating GaAs wafer. In Fig. 27, a room-temperature PR spectrum for the investigated structure is shown. A few resonances related to DQW transitions occur above the feature related to GaAs band gap transition. The transitions are labelled according to the common notation with indices *s* and *a*, where index *s* (*a*) means the transition between symmetric (antisymmetric) states. Sęk et al. [123] obtained a very good agreement between the experimental transition energies and those from theoretical calculations based on envelope function approximation.

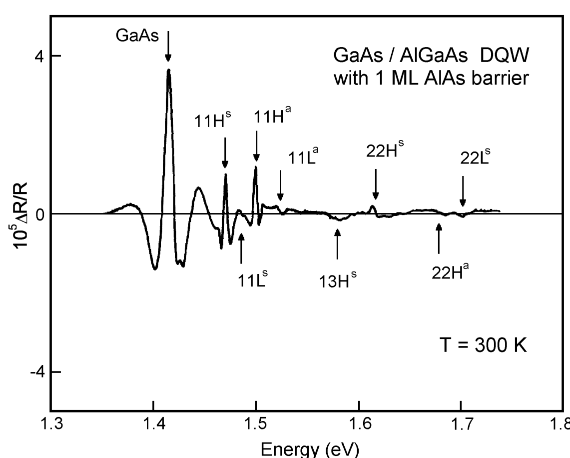

Fig. 27. Photoreflectance spectrum from the GaAs/$Al_{0.3}Ga_{0.7}As$ double quantum well structure. Arrows indicate the experimental transition energies (after Sęk et al. [123])

The $In_{0.045}Ga_{0.955}As$/GaAs DQW structure was investigated by Sęk et al. [124]. They examined the dependence of the intensity of forbidden transitions on the built-in electric field. To change the electric field in the structure, the authors used an additional laser beam (third light beam). They found that the ratio of the intensity of forbidden transitions to the intensity of the fundamental allowed transition depends linearly on the third beam power density and hence approximately linearly on the internal electric field in the region of DQW.

To obtain an enhanced spatial resolution comparing to conventional PR, Cho et al. [125] put forward the near-field scanning optical spectroscopy combined with PR to investigate $Al_{0.3}Ga_{0.7}As$/GaAs quantum well structures.

5.2. Quantum dots

With nanoscale lithographic techniques used to 2D heterostructures, it is possible to obtain quantum dots (QD) – quasi zero dimensional (0D) objects.

Qiang et al. [126] reported room-temperature PR studies of GaAs/$Ga_{0.7}Al_{0.3}As$ quantum dots arrays, fabricated by reactive ion etching. An MBE structure, consisting of a 500 nm of an unintentionally doped GaAs buffer layer followed by 100 periods of GaAs(8 nm)/$Ga_{0.7}Al_{0.3}As$(12 nm) quantum wells, capped by 10 nm of GaAs, was grown on (001) semiinsulating GaAs substrate. Three quantum dot arrays, with the lateral sizes of 500 nm, 400 nm and 230 nm, and MQW control structure have been investigated. The distance between the dots was four times greater than their diameter.

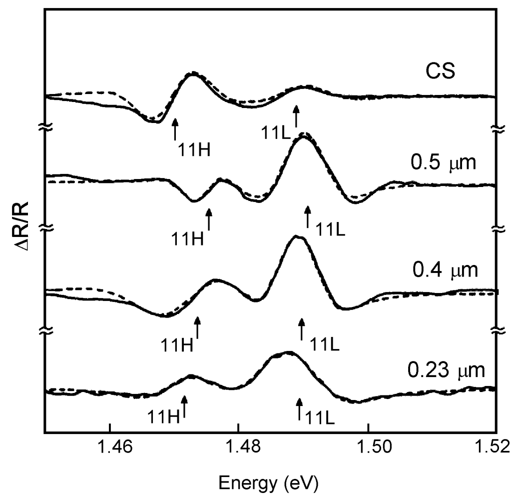

Fig. 28. Photoreflectance spectra at 300 K in the region of 11H and 11L transitions from three GaAs/$Al_{0.3}Ga_{0.7}As$ quantum dot arrays and the spectrum of the control structure (after Qiang et al. [126])

The solid lines in Fig. 28 show room-temperature photoreflectance spectra of the control sample and the QD arrays. The dashed lines are the least-square fits of the data to the first derivative of a Gaussian profile. The calculations yield the energy positions and the broadening parameters of PR features. Energies of 11H and 11L optical transitions obtained from the experiment are denoted by arrows.

The energy positions of 11H and 11L from the control sample are consistent with an 8 nm GaAs quantum well. The energy of the 11L transition varies very little from sample to sample. When compared to the control sample, the energy of 11H optical transition in the 500 nm dot structure is blue shifted by about 5 meV. It decreases to almost its original position (in the control sample) in the 230 nm dot array. The strain induced by RIE is fairly uniform resulting in small differences in the broadening parameters for all resonances.

Qiang et al. explained the behaviour of 11H and 11L transition energies in terms of the strains in the quantum dots. For the 500 nm dots there is a compressive strain of about -7×10^{-4} along the growth direction. A reduction of strain was observed when the lateral dimension of QD decreased. For the structure with the smallest dots the strain was reduced to about -2×10^{-4}.

Gumbs et al. [127, 128] investigated the intersubband transitions from modulation -doped GaAs/GaAlAs quantum dot arrays fabricated by RIE. By using PR performed at 77 K and 300 K, they studied two quantum dot structures with dots of 60 nm and 100 nm in diameter.

Klar et al. [129] investigated high-density patterns of ZnTe/$Zn_{0.93}Mn_{0.07}Te$ quantum dots. Quantum dots with the diameter of 200 nm were prepared by electron lithography followed by Ar^+ ion beam etching from four MBE grown ZnTe/$Zn_{0.93}Mn_{0.07}Te$ MQW structures with 4 nm, 6 nm, 8 nm and 10 nm well widths. Photoreflectance measurements were performed at 10 K. The modulation was carried out with a 632.8 nm (1.96 eV) He-Ne laser (below-bandgap photomodulation). Klar et al. showed that the main effect of the nanofabrication process is a change in the strain of the quantum dot structures when compared with control sample. The parent structure is, in a good approximation, strained to the ZnTe buffer layer whereas quantum dots are unstrained.

For light hole excitons, an increase in the oscillator strength was observed in the QD structures. An electric dipole moment, parallel to the growth direction, introduced by the probe light that can penetrate the QD side walls (the side walls are not perpendicular to the surface) is a possible explanation of this effect.

Klar et al. [129] did not observe any confinement effects due to the reduction of the dimensionality from 2D to 0D. The lateral sizes of dots being under study were too large to observe such confinement effects.

The quantum dot structures, described in the above papers, were obtained by the lithography followed by etching processes. The size of dots and the level of perfection in such structures are limited by the lithographic processing. Using an epitaxial growth of materials with a large lattice mismatch is a way of obtaining islands of small lateral sizes of one material grown on the other material. Quantum dots obtained in such a way are referred as "self-assembled" or "self-organised".

Ulrich et al. [130] used the above method to obtain nanoscale InP islands embedded in $In_{0.48}Ga_{0.52}P$ matrices. The structures were grown by MBE on (001) GaAs substrate. The substrate layer was followed by 200 nm of $In_{0.48}Ga_{0.52}P$ and from three to ten monolayers of InP, covered by another 200 nm $In_{0.48}Ga_{0.52}P$ cap layer. The atomic force microscope (AFM) pictures showed that the island density is of the order of 10^{10} cm^{-2}. This structure, with nominally three monolayers of InP, formed dots (islands) of 20–30 nm in diameter and 5–10 nm high. When the number of monolayers increases to seven, the dot diameter increases up to 40–50 nm.

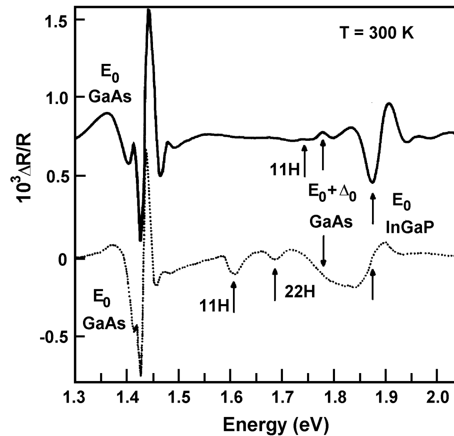

Fig. 29. Photoreflectance spectra of $InP/In_{0.48}Ga_{0.52}P$ island (dot) structures with 3 ML (solid line) and 7 ML (dashed line) of nominal InP thickness (after Ulrich et al. [130])

Figure 29 presents photoreflectance spectra, measured at 300K, for structures with three and seven monolayers of InP, respectively. Both spectra show resonances corresponding to E_0(GaAs), $E_0+\Delta_0$(GaAs) and E_0(InGaP) optical transitions. The transition denoted as 11H is an optical transition between the first heavy hole and the electron states of the InP islands. For the three-monolayer sample, the 11H transition is partially obstructed by the PR feature of $E_0+\Delta_0$(GaAs) transition. The transition labelled 22H is observed in the PR spectrum of the seven-monolayer sample. Ulrich et al. [130] proposed a simple theoretical model, based on the envelope-function approximation, to calculate the subband energies. The transition energies, obtained from the theoretical considerations, agree well with energy values obtained from the experiment for the structures with InP nominal thickness between three and ten monolayers.

Sęk et al. [131] used room-temperature photoreflectance spectroscopy to investigate optical transitions in MOCVD-grown, InAs/GaAs structures with self-organised quantum dots.

Tellurium-doped GaAs substrate was followed by the following layers: 100 nm GaAs buffer, 25 nm $Al_{0.3}Ga_{0.7}As$, 100 nm GaAs and 1.65 nm monolayer of InAs. A strong lattice mismatch between the latter two compounds induces the formation of InAs pyramids. The QD pyramids are covered by 1 nm layer of $In_{0.3}Ga_{0.7}As$. This structure was then covered with the 20 nm layer of GaAs, 25 nm of $Al_{0.3}Ga_{0.7}As$ and capped with 20 nm of GaAs. From the transmission electron microscope measurements, the diameter of the dots is in 10–12 nm range while the height is about 2.5–3 nm.

A room-temperature PR spectrum of the investigated QD structure is presented in Fig. 30 (circles). In the figure, we can see three groups of features related to quantum dots, InAs wetting layer and GaAs band gap, respectively. The features labelled QD1, QD2 and QD3 correspond to optical transitions in quantum dots. The resonances designated as WL1 and WL2 correspond to the 11H and 11L transitions in the step-shaped quantum well, formed in the InAs wetting layer and the $In_{0.3}Ga_{0.7}As$ layer covering the dots.

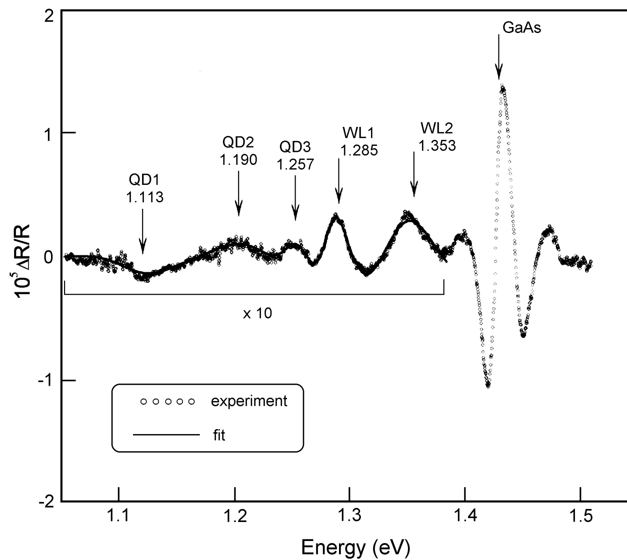

Fig. 30. Room-temperature PR spectrum of InAs/GaAs quantum dot structure (circles). Solid line represents a fit according to the first-derivative Gaussian lineshape to the experimental data. Arrows indicate the transition energies (after Sęk et al. [131])

In order to obtain the transition energy values, fitting of the first derivative of the Gaussian lineshape to the experimental data was performed. The FDGL fit is presented in Fig. 30 as a solid line. The interpretation of QD related transitions was possible after theoretical calculations for buried, pyramid-shaped InAs QD's on (001) GaAs bound to {101} facets. Assuming the pyramidal shape of the dots, accounting for strain distribution, piezoelectricity, valence band mixing and conduction band –valence band coupling, the electronic structure and optical properties were modelled using 8-band **k·p** theory [104]. After extrapolating these results to room temperature

and taking into account the exciton binding energy, the values of transition energy are in good agreement with the experimental results. QD1, QD2 and QD3 transitions were identified as e0-h0, e2–h1 and e1–h3, respectively, where e0 (h0) denotes the ground electron (hole) state.

The vertical stacking of dots in laser structures and the idea of employing coupled dots in quantum computational concepts caused an increase of interest in the investigation of a dot–dot interaction in double dot systems. The photoreflectance turned out to be adequate also in this case. Sęk et al. [132, 133] investigated three self-organized vertically coupled $In_{0.6}Ga_{0.4}As/GaAs$ double quantum dots structures differing only in the thickness L_S of the GaAs separating layer. The spectra of the structures obtained at 10 K PR are presented in Fig. 31.

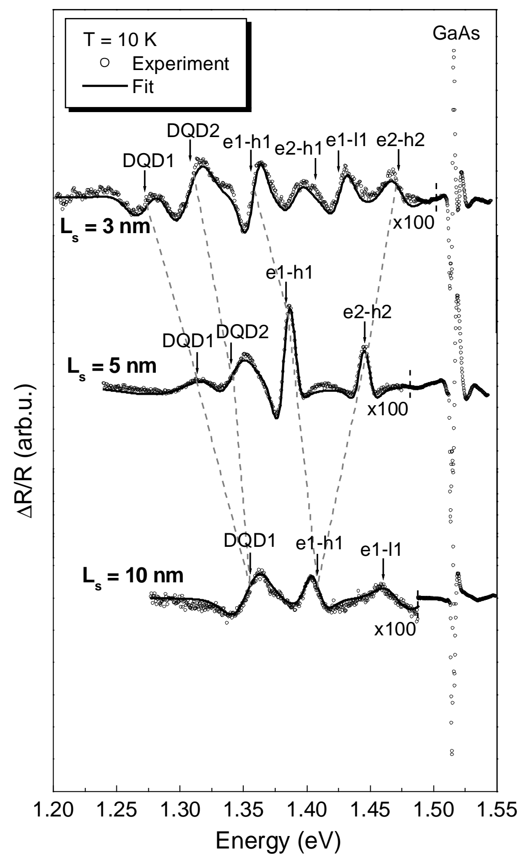

Fig. 31. Photoreflectance spectra of double quantum dot structures for various thicknesses of the separating GaAs layer (after Sęk et al. [132])

The splitting of double wetting layer quantum well and quantum dot states due to the coupling has been observed even though the experiment was carried out on millions of dots and the PR lines were inhomogenously broadened. The DQD's splitting energy has been determined from the experiment and compared to its calculated dependence on

the spacer thickness. A very good agreement was obtained which confirmed that for 10 nm thickness of the separating GaAs barrier the dots are almost uncoupled and structure can be treated as two independent layers of dots.

6. Photoreflectance study of device structures

In the preceding sections, it was shown that photoreflectance spectroscopy is a powerful tool for investigation of characteristic properties of bulk semiconductors and low-dimensional semiconductor heterostructures. The PR technique may be used not only for characterization of the low-dimensional structures but also to examine semiconductor device structures as well. In the next few paragraphs, we will present applications of PR spectroscopy for the studies of high electron mobility transistor (HEMT) structures, pseudomorphic HEMT (PHEMT) devices, heterojunction bipolar transistors (HBT), and vertical/planar light emitting lasers.

6.1. Transistors

A HEMT structure is formed by a charge transfer from a heavily doped AlGaAs layer to an undoped GaAs layer. This process results in placing the electrons in a very pure GaAs layer, resulting in very high electron mobility. A scheme of such a structure is shown in Fig. 32. The electrons transferred to the GaAs layer are confined to the interfacial region and form a two-dimensional electron gas (2DEG) in a nearly triangular potential well. In order to avoid Coulomb interactions between the electrons with enhanced electron mobility in 2DEG and the ionised donors in n^+ AlGaAs layer, an insulating AlGaAs spacer layer usually separates these two layers. The thickness of the spacer determines the number of electrons transferred. The presence of a potential well results in the formation of subband states in the conduction band. The valence band exhibits no confinement and hence has a three-dimensional characteristics.

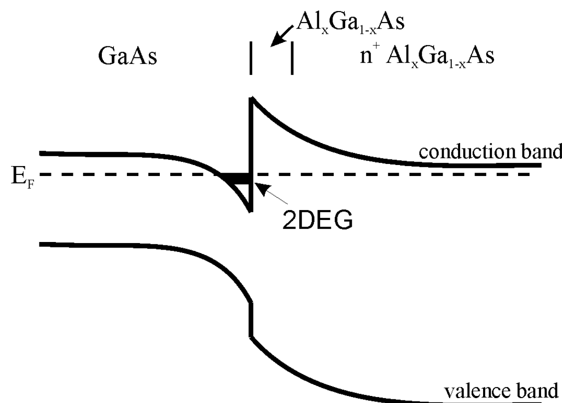

Fig. 32. Schematic diagram
of AlGaAs/GaAs HEMT structure

Soares et al. [134, 135] investigated three AlGaAs/GaAs HEMT structures with different spacer widths. All structures were grown by MBE on a semi-insulating GaAs substrate. The GaAs substrate was followed by 500 nm undoped active GaAs layer, an undoped $Al_{0.3}Ga_{0.7}As$ spacer, an Si-doped $Al_{0.3}Ga_{0.7}As$ barrier layer and an Si-doped GaAs cap layer of donor concentration $N_D = 3\times10^{18}$ cm^{-3}. The widths and donor concentrations of the barrier layers were 50 nm and $N_D = 1\times10^{18}$ cm^{-3} for structure 1 and 40 nm and $N_D = 1.5\times10^{18}$ cm^{-3} for structures 2 and 3, respectively. The thickness of the spacer layer was 0 nm, 6 nm and 8 nm.

Figure 33 presents room-temperature PR spectra of three HEMT structures. Each spectrum exhibits two types of oscillations: short-period oscillations at the fundamental gap of GaAs and wide-period oscillations extending over the whole spectral range. The wide-period oscillations originate from the Franz–Keldysh effect. The strength of the surface electric field, obtained from the period of FKO, is slightly lower than that obtained from the electric field profile calculations (about 750 kV/cm).

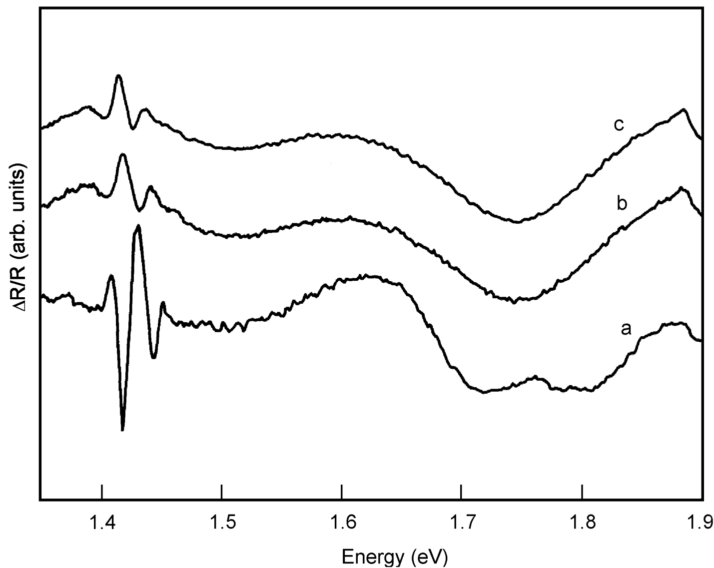

Fig. 33. Photoreflectance spectra from AlGaAs/GaAs HEMT structures
1 (a), 2 (b) and 3 (c) (after Soares et al. [134])

The short-period oscillations in structure 1 differ from oscillations in the other structures. For example, the amplitude of these oscillations for structures 2 and 3 is considerably smaller than for structure 1. The differences between structure 1 and the other structures, concerning GaAs layers, occur only at the AlGaAs/GaAs interfaces. Thus Soares et al. [134] attributed the lineshape discrepancies to different interface

qualities. In the case of sample 1, the interface is of relatively good quality and the charge density, associated with the interface defects, is small. Interface defects and the associated interface charge seem to be present in samples 2 and 3. The quality of the interface influences the electric field profile and hence the PR spectra. The short-period oscillations cannot be traced back to the Franz–Keldysh effect. Soares et al. assumed that the origin of these features is from optical transitions to subband states above the Fermi level. These subbands are formed in AlGaAs/GaAs potential well.

Sęk et al. [136] studied two AlGaAs/GaAs HEMT structures grown by MBE. A buffer layer, 100 periods of GaAs(2.5 nm)/AlGaAs(2.5 nm) superlattice, 510 nm GaAs active layer, AlGaAs spacer layer of 40 or 80 nm width and 200 nm n-doped (1×10^{17} cm^{-3}) AlGaAs layer were grown on a GaAs substrate. The structure was terminated with a 17 nm GaAs cap layer.

A PR spectrum of HEMT structure with an 80 nm spacer layer is presented in Fig. 34. The spectrum can be divided into several independent regions. In the region around 1.42 eV, the main peak corresponds to GaAs band gap transition. A weak peak, visible in the low-energy part of this spectrum, is related to the excitonic transition. The additional resonance at 1.435 eV is probably related to a two-dimensional electron gas. Sęk et al. [136] interpreted the oscillatory signal around 1.6 eV as the Franz–Keldysh oscillations associated with the superlattice (SL) present in the structure. In the presence of an internal electric field, the electrons can be accelerated in the field direction and transitions in short-period SL may be analyzed in terms of the miniband Franz–Keldysh effect. The electric field value, deduced from the period of the oscillations, is 4.4 kV/cm.

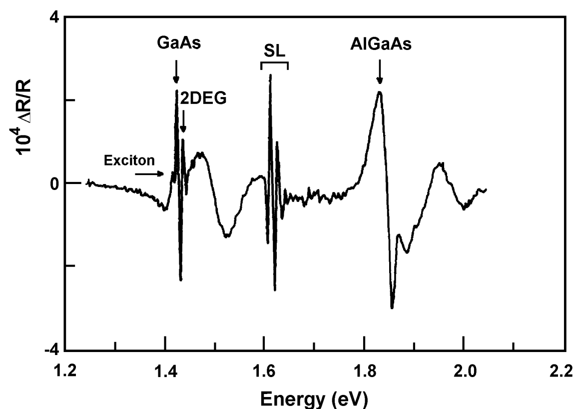

Fig. 34. Room-temperature spectrum from $Al_{0.33}Ga_{0.67}As$/GaAs HEMT structure (after Sęk et al. [136])

Between 1.45 eV and 1.6 eV there is a broad oscillation. Such an oscillation is characteristic of the Franz–Keldysh effect from the fully depleted GaAs cap layer. A feature corresponding to the AlGaAs band gap transition, appears in the spectrum

above 1.85 eV. From the position of this resonance, the Al content was deduced to be 33%. An additional feature is present at about 1.95 eV. This feature probably results from the overlapping of two Franz–Keldysh oscillations associated with AlGaAs band gap resonances from different parts of the structure: from the highly doped AlGaAs layer and the undoped AlGaAs spacer.

The photoreflectance spectrum obtained from the structure with a 40 nm spacer layer was very similar to the previous one. The only difference was in the absence of the excitonic feature due to the higher (6.3 kV/cm) electric field formed in this structure.

One type of HEMT, the pseudomorphic AlGaAs/InGaAs/GaAs modulation doped structure (PHEMT), demonstrated an outstanding power performance. In the AlGaAs /InGaAs/GaAs system, a large electron concentration in the two-dimensional gas can be achieved while the electron mobility remains very high. These structures promise device performance up to a few hundred GHz. The energy band profile of PHEMT structure is shown in Fig. 35.

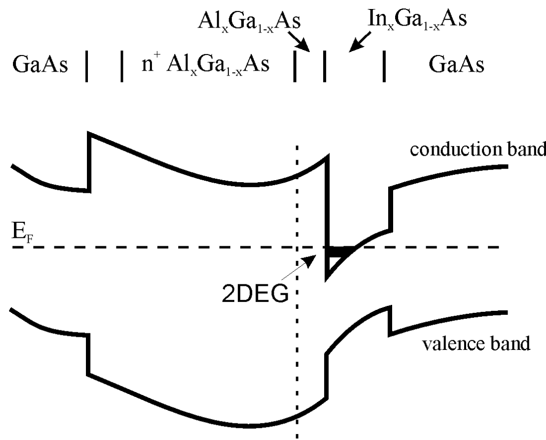

Fig. 35. The energy band profile
of AlGaAs/InGaAs/GaAs PHEMT structure

A detailed study of a pseudomorphic $Al_{0.22}Ga_{0.78}As/In_{0.21}Ga_{0.79}As/GaAs$ HEMT structure in the temperature range from liquid nitrogen to the room temperature was reported by Yin et al. [137]. The structure was fabricated with MBE on (001) GaAs substrate. It has similar profiles as those in HEMTs used for both low-noise and power amplification at 94 GHz. A 300 nm of not-intentionally doped GaAs, followed by 15 nm of $In_{0.21}Ga_{0.79}As$, 3 nm of $Al_{0.22}Ga_{0.78}As$, a planar Si doping layer of 5×10^{12} cm^{-2}, 50 nm of $Al_{0.22}Ga_{0.78}As$ and a 5 nm GaAs cap, was grown on the top of the buffer structure. From Hall measurements, sheet electron densities of $N_s = 2.3\times10^{12}$ cm^{-2} at 77 K and $N_s = 2.5\times10^{12}$ cm^{-2} at 300 K were determined.

Figure 36 shows both the PR and the electroreflectance (ER) spectra of PHEMT structure. The features below 1.4 eV, labelled A, B and C, are associated with InGaAs quantum well. The features between 1.4 eV and 1.45 eV originate from GaAs and those

at about 1.75 eV from the AlGaAs layer. The peaks at energies lower than those from AlGaAs, originate from GaAs/AlGaAs MQW. The part of the spectrum originating from InGaAs quantum well is the most interesting. Lineshapes of A, B and C features are unusual for modulation spectroscopy from a QW system. The traces should have positive and negative lobs but in this case they lie only on one side of the baseline. Also, the peak labelled as A is asymmetric on the high-energy side. This asymmetry property is due to the Fermi level filling factor. This enabled Yin et al. [137] to determine the Fermi energy and hence N_s.

In order to identify the origins of the A, B and C peaks, Yin et al. performed a self-consistent theoretical calculation. They found a very good agreement between ER experiment and theory associating features A, B and C with 21H, 32H and 42H transitions, respectively. Transitions which involve the ground electron subband are not allowed since E_F lies above this level. The densities of two-dimensional electron gas, obtained from the data, are in a good agreement with the Hall results. The Fermi energy (and hence N_s), obtained from the PR studies, is larger than that corresponding to the ER measurements. The discrepancy results from the presence of carriers photoexcited by the pump beam. Decreasing the pump light intensity can reduce the differences between the PR and ER spectra.

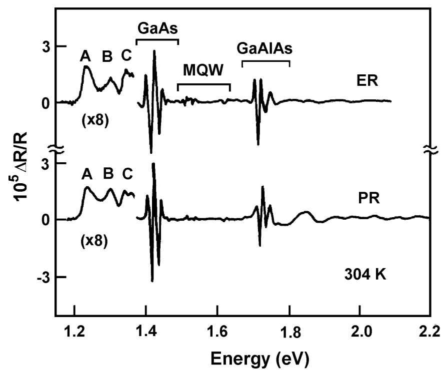

Fig. 36. Photoreflectance and electroreflectance spectra from AlGaAs/InGaAs/GaAs PHEMT structure. Features labelled A, B and C are associated with InGaAs quantum well (after Yin et al. [137])

Yin et al. [138] performed room-temperature PR investigations of three different AlGaAs/InGaAs/GaAs PHEMT structures. Besides the investigations of InGaAs region of the PR spectra, they studied features related to the GaAs and AlGaAs layers. They deduced electric fields corresponding to the GaAs and AlGaAs and also the Al composition. The field related to the GaAs signal is in agreement with the calculated built-in electric field. The Al composition also confirms the intended growth conditions.

Han et al. [139] studied the AlGaAs/InGaAs/AlGaAs PHEMT structures with different doping profiles. The doping on both sides of the InGaAs channel affects the electric field in GaAs and AlGaAs layers. The front side doping (Si delta-doped top AlGaAs layer, 2 nm from AlGaAs/InGaAs interface) influences mostly the Franz–Keldysh oscillations (electric field) in the AlGaAs layer, while back-side doping (Si-doped AlGaAs layer 3 nm below

InGaAs/AlGaAs interface) affects the Franz–Keldysh oscillations of the buffer GaAs feature. Han et al. [139] have not found any relationship between the electric field present in the structure and the channel carrier concentration.

There is a considerable interest in heterojunction bipolar transistor (HBT) technology for use in high-speed digital circuits and efficient microwave devices. The large valence band discontinuity at the emitter-base junction introduces an energy barrier which limits the injection of minority carriers from the base to the emitter. Hence, the emitter injection efficiency and the current gain can be improved significantly. An important drawback of HBT is a large collector–emitter offset voltage resulting from the turn-on voltage difference between the emitter–base heterojunction and base-collector homojunction.

Bottka et al. [140] studied AlGaAs/GaAs HBT structures grown by MOVPE technique. After growth, HBTs were fabricated in a portion of the wafer. In order to assess the transistor performance, current–voltage (*I–V*) and capacitance–voltage (C–V) characteristics were collected.

Figure 37 shows the PR spectra from the sample grown on a thick base layer (low current gain, $\beta = 5$), obtained using 400 Hz modulated 488 and 633 nm laser light. In part (a) of the figure, the damped oscillations between 1.45 and 1.7 eV correspond to the Franz–Keldysh oscillations mainly from the emitter-base space charge region. An electric field corresponding to these oscillations is about 130 kV/cm. In part (b) of the figure, an additional lower period Franz–Keldysh oscillation is observed in the spectral region between 1.44 and 1.5 eV. This feature originates from the base-collector space charge region. The oscillatory structure above 1.79 eV corresponds to the Franz–Keldysh oscillations of the $Al_xGa_{1-x}As$ emitter layer, having an electric field of about 100 kV/cm. The $x = 0.28$ Al mole fraction was deduced from the energy gap.

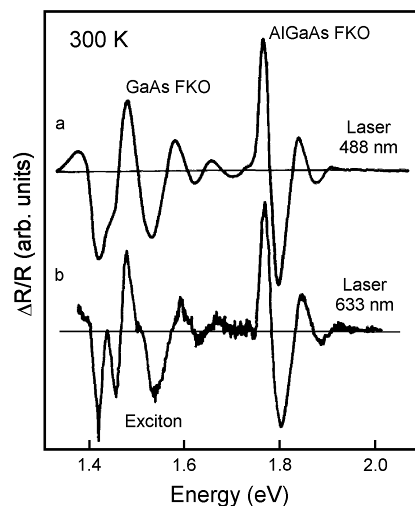

Fig. 37. Room-temperature photoreflectance spectra from a wide base AlGaAs/GaAs HBT structure (after Bottka et al. [140])

The base–emitter region is most critical for the overall device performance. A small difference in the placement of the base-emitter p-n junction can have considerable impact on the device. From the analysis of certain spectral features, Bottka et al. [140] evaluated the built-in DC electric field in both the AlGaAs emitter and in the n^- GaAs collector region.

Sun and Pollak [141] studied the origin of the Franz–Keldysh oscillations, observed in photoreflectance spectra, associated with the electric fields in the AlGaAs emitter and the GaAs collector of graded band gap heterojunction bipolar transistors. They derived analytical expressions for the origins of the Franz–Keldysh oscillations, associated with the fields in the graded emitter and collector regions of AlGaAs/GaAs HBT. The authors found that the oscillations from the collector are the measure of the maximum collector space charge field at the collector-base junction. The Franz –Keldysh oscillations, originating from the graded band gap AlGaAs emitter, are a function of both the space charge field and emitter-base grading dimension.

Compared to GaAs/AlGaAs based structures, lattice matched $InP/In_{0.53}Ga_{0.47}As$ HBT structures have several advantages. Low turn-on voltage, low surface recombination rate and a use of the same substrates as sources and detectors of 1.3–1.55 μm wavelength radiation (favoured in optoelectronics) are some of the examples.

Using PR, Yan et al. [142] investigated a lattice-matched $InP/In_{0.53}Ga_{0.47}As$ HBT structure grown by gas-source MBE. They performed a room-temperature measurement. From the periods of the Franz–Keldysh oscillations, they evaluated built-in electric fields to be 30 kV/cm and 100 kV/cm and corresponding donor levels of 4.5×10^{15} and 3.5×10^{16} cm^{-3} in n-InGaAs collector and n-InP emitter regions, respectively. The energy of the optical transition in InGaAs indicates that this material is lattice-matched to the InP.

A heterojunction bipolar transistor, based on InAlAs/InGaAs, has a break-down voltage lower than the two types of HBTs described above. Because of this fact, the InAlAs/InGaAs HBTs become an interesting topic in low-bias integrated-circuit applications. The simplest way to reduce the offset voltage is the method of inserting an intrinsic spacer, made of material with a small band gap, between the emitter and the base. Confining the two-dimensional electron gas, the spacer reduces the energy spike in the emitter-base junction.

Using photoreflectance spectroscopy, Chen et al. [143–146] studied lattice-matched InAlAs/InGaAs HBTs, grown by MBE. The structures were fabricated on an n^+ InP:Si substrate (001). Two samples, with 30 nm and 50 nm width of the undoped InGaAs spacer layer, have been studied. Figure 38 shows a self-consistent calculated energy band diagram of a sample with the 30 nm spacer layer.

Photoreflectance spectra of the structures studied are presented in Fig. 39. Spectrum #1 comes from the structure with the 30 nm spacer and spectrum #2 is related to the structure with the 50 nm spacer. Features labelled as A and E denote the transitions due to the $In_xGa_{1-x}As$ and the $In_yAl_{1-y}As$ band gaps, respectively. From the energy position of these two features, In contents $x = 0.516$ and $y = 0.540$ were obtained. The quantum

confined excitonic transitions, with excitons formed by electrons confined to the QW in the emitter–spacer junction and unconfined holes in the valence band, are denoted as B. The features denoted as C are due to the electronic transitions between the valence band and a subband edge in the triangular quantum well in the spacer portion. The $E_0 + \Delta_0$ transitions in InGaAs are labelled D. The Franz–Keldysh oscillations near C and E are related to the built-in DC electric field. From the oscillations, Hsu et al. [143] found that the electric field in the InGaAs spacer and InAlAs emitter regions are 50.2 kV/cm and 107.6 kV/cm, respectively, for the sample with $L_S = 30$ nm and 41.4 kV/cm and 107.6 kV/cm for the sample with $L_S = 50$ nm. The electric field associated with C decreases as the spacer thickness increases. The authors estimated that the interface charge carrier density, N_S, is 3.54×10^{11} cm^{-2} for $L_S = 30$ nm and 4.22×10^{11} cm^{-2} for $L_S = 50$ nm.

Photoreflectance studies on the InAlAs/InGaAs HBT structure with $L_S = 30$ nm were continued by Chen and Jan [145]. They analyzed the behaviour of a two-dimensional electron gas at the temperatures between 10 K and 300 K. For the first time, Chen and Jan [145] utilized the temperature dependence of the effective mass to analyze Franz–Keldysh oscillations with the photoreflectance technique. The values deduced from the oscillations were in reasonable agreement with the calculations based on the intended growth condition.

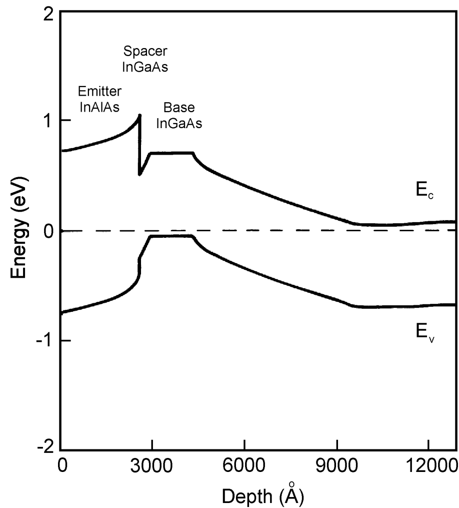

Fig. 38. Self-consistent calculated energy band diagram of InAlAs/InGaAs HBT with a spacer layer of 30 nm (after Chen et al. [144])

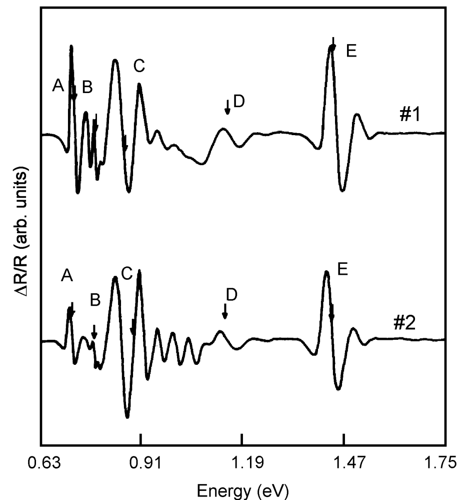

Fig. 39. The photoreflectance spectra from InAlAs/InGaAs HBTs with 30 nm (#1) and 50 nm (#2) spacer thickness. The origin of optical transitions marked with arrows is described in the text (after Hsu et al. [143])

Chen et al. [147] investigated graded InAlAs/InGaAs HBT structures at the temperatures between 8 K and 300 K. Using the Varshni and Bose–Einstein equations, they

described the temperature variation of energy gaps. From the observed Franz–Keldysh oscillations, they evaluated the built-in electric fields in the i-InGaAs collector, i-InGaAs spacer and n-InAlAs emitter regions. In the interfaces between the emitter and base, the electric field values agree with the continuity condition of electric displacements.

The n-p-n double-heterojunction bipolar transistor structure InGaP/InGaAsN/GaAs was characterized by Lin et al. [148] using polarized photoreflectance spectroscopy. The ordering parameter of the InGaP was deduced from the polarization ([110] and $[1\bar{1}0]$) dependence of the PR signals from the emitter region. The ordering-related piezoelectric field was also found to influence the electric field, as evaluated from the Franz–Keldysh oscillations observed in the InGaP emitter region. The field in the emitter region was found to be about 25 kV/cm smaller than the theoretical value that does not take into account the possible ordering induced screening effect, while the field in the collector region agrees well with the theoretical value. In addition, the InGaAsN band gap was also determined by analyzing the PR spectrum of the base region.

6.2. Semiconductor lasers

The vertical cavity surface emitting laser (VCSEL) became recently very important in opto-electronics. VCSEL has several advantageous properties such as single longitudinal mode operation, small beam divergence, low threshold current and ease of integrability.

The photoreflectance results on VCSEL structures were reported by Berger et al. [149, 150]. The samples were grown by a gas source MBE. The structures consisted of an n^+ distributed Bragg reflector (DBR) as the bottom mirror, a cavity with three GaAs/AlGaAs QWs and a p^+ DBR as the top mirror. The full VCSEL structure described above is marked DU. The structure obtained at the same conditions but without top DBR is marked DT.

Berger et al. [149] recorded both the reflected signal RI_0 (not normalized reflectivity) and the modulated signal ΔRI_0. A numerical division of ΔRI_0 by RI_0 gave the PR spectra. Reflected spectra and PR spectra obtained at room temperature for full structure (DU) and the structure without top DBR (DT) are plotted in Fig. 40. The dashed lines represent the RI_0 signal. For the DU structure, the RI_0 signal shows a reflectivity plateau of the cavity. Near 1.58 eV, RI_0 exhibits a slight dip, which is due to the resonance (Fabry–Perot) mode of the cavity. Solid lines represent PR spectra. The PR spectra in Fig. 40 exhibit two groups of features in each structure. A transition attributed to the quantum well occurs around 1.5 eV. Between 1.6 and 1.7 eV is a feature related to the AlGaAs layers. In the energy range of the plateau, both features in the DU spectrum are screened. Therefore, it is not possible to precisely determine the transition energies from this spectrum. The PR spectrum for the DT structure was used to determine the transition energies in the DU spectrum. Berger et al. [149] discovered that the features around 1.5 eV originate from the optical transition between the heavy hole and

the electron subbands. From the energy position of the AlGaAs related feature, the Al content of 16% was determined.

In order to change the quantum well transition energy, the measurements were performed at temperatures down to 9 K. The PR and RI_0 spectra for full VCSEL structure obtained at 300 K, 110 K and 9 K are shown in Fig. 41. In the PR spectra, the AlGaAs related transitions exhibit Franz–Keldysh oscillations, from which the value of the electric field in the cavity is estimated to be 38 kV/cm at a room temperature and decreases to 17 kV/cm at 9 K. At lower temperatures, the AlGaAs related transitions are no more screened. As the temperature decreases, the energy shift of QW transition is larger than the Fabry–Perot cavity mode shift. The intensity of the PR feature corresponding to the 11H transition rises as the temperature decreases. The maximum intensity was observed at 110 K. Two features around 1.57 eV are present in the spectrum recorded at 110 K. The higher energy feature originates from the 11H transition and the lower energy one corresponds to the Fabry–Perot cavity mode [150].

Klar et al. [151, 152] performed photoreflectance and conventional reflectance studies on an InGaAs/GaAs/AlGaAs vertical cavity surface emitting laser structure at a room temperature. The structure was grown by MBE on n^+ GaAs substrate. It was designed for operation at $\lambda = 1$ μm, and consists of a GaAs cavity with a 8.5 nm wide, compressively strained $In_{0.28}Ga_{0.72}As$ quantum well in the centre. The cavity is embedded between bottom (n^+) and top (p^+) distributed Bragg reflectors.

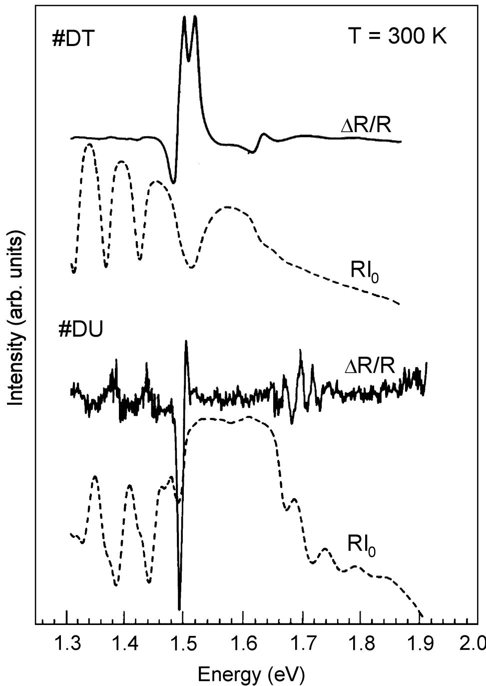

Fig. 40. Photoreflectance spectra at 300 K

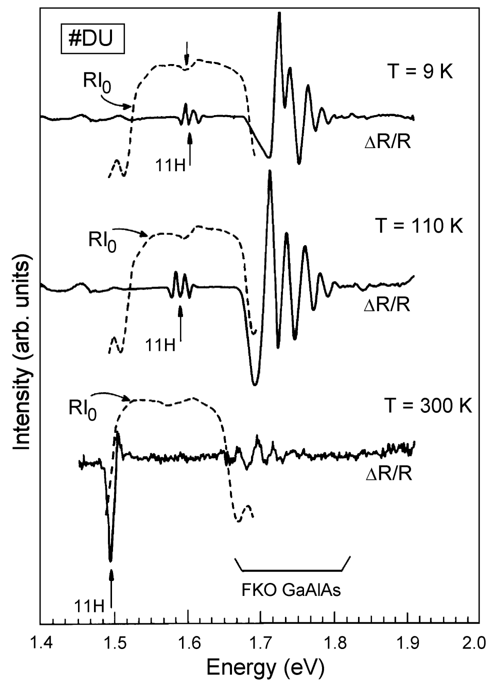

Fig. 41. Photoreflectance spectra from

from the full VCSEL structure (#DU) and structure without a distributed Bragg reflector (#DT) – solid lines. Dashed lines represent reflected signal RI_0 (after Berger et al. [149])

the full structure of a vertical cavity surface emitting laser (#DU) at 300 K, 110 K and 9 K (solid lines). Dashed lines hold for the reflected signal (after Berger et al. [149])

Figure 42 shows a set of room-temperature PR spectra for different angles of incidence of the probe light. The spectra were taken with the lock-in amplifier set to detect $\Delta R/R$ signal, in-phase with respect to the constant PL background from the sample [151]. All the photoreflectance spectra show three prominent features. The first, at about 1.185 eV is 11H exciton transition in the $In_{0.28}Ga_{0.72}As$ quantum well. The second signal moves to a higher energy with increasing angle of incidence. It shows the same angular dependence as the cavity mode in the R spectrum, hence Klar et al. [151] conclude that this PR signal is due to the modulation of the cavity mode. Due to a variation in the In concentration, the ground-state QW transition is about 100 meV lower in energy than the cavity mode. The third signal, above 1.4 eV, is due to the FKO in the GaAs layers.

The strength of the signal from the cavity mode varies with the angle of incidence and is stronger between 30° and 60° than at the angles of 15° and 75°. This may be explained as follows. When the cavity mode feature overlaps in energy with a higher-order quantum well transition, probe light at this energy will be more strongly modulated by the QW than at other angles of incidence (such as 15° and 75°). Thus, one would expect a stronger photoreflectance signal for the cavity mode when it passes through positions of resonance with the higher-order QW transition, which are 12H, 13H, 21H and 22H for the QW being under study [151]. For the ranges of incidence between 30° and 60°, the cavity mode passes through 13H and 21H resonances.

The origin and lineshape of the photoreflectance signal associated with the cavity mode, Klar et al. [151] explained as follows. Due to the modulation-induced changes in the complex refractive index of the cavity layers, the cavity mode feature in the reflectance spectrum gives rise to a corresponding feature in the photoreflectance. Thus, the PR lineshape of this feature corresponds to the first derivative of the cavity mode dip in the reflectance spectrum.

Gosh et al. [153] report the PR studies on the coupling between the Fabry–Perot cavity mode (CM) and the QW ground-state excitonic feature in VCSEL structures. They applied changes in the symmetry of the CM-QW spectral feature by changing the angle of incidence of the probe beam.

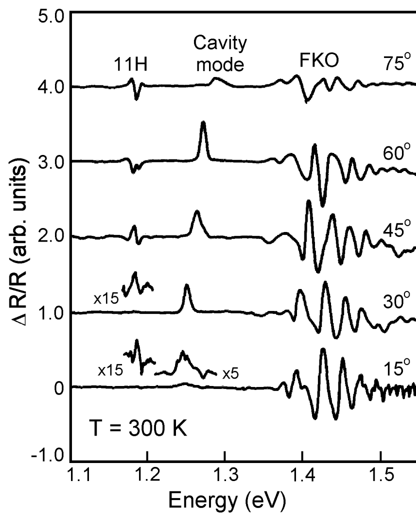

Fig. 42. Photoreflectance spectra from InGaAs/GaAs/AlGaAs VCSEL structure for different angles of incidence of the probe light (values indicated on the right) taken at a room temperature (after Klar et al. [151])

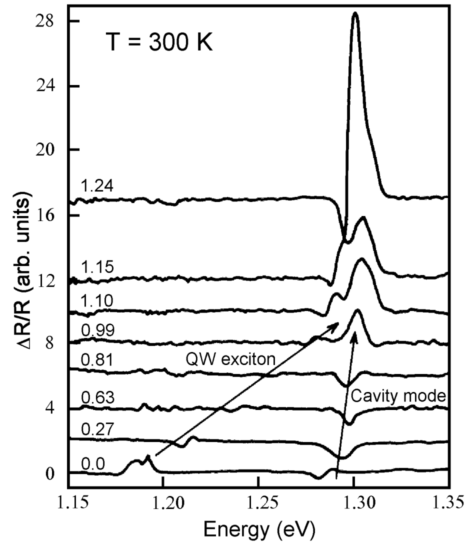

Fig. 43. Photoreflectance spectra from InGaAs/GaAs/AlGaAs VCSEL structure for various hydrostatic pressures. The pressure values in GPa are indicated on the left (after Klar et al. [152])

Klar et al. [152] continued the studies of InGaAs/GaAs/AlGaAs VCSEL structure, measuring the photoreflectance spectra at hydrostatic pressures up to 1.24 GPa. Figure 43 shows a series of photoreflectance spectra for various hydrostatic pressures. All the spectra display two signals. At ambient pressure, the low-energy signal at about 1.19 eV can be assigned to the 11H transition. The high-energy signal, at about 1.295 eV is attributed to the cavity mode. Both signals shift towards higher energy with increasing pressure. Because the energy shift of quantum well exciton feature is bigger than that of the cavity mode feature; at the highest pressure the overlap between those two features is observed.

From the photoreflectance data, Klar et al. [152] calculated the pressure coefficients for the QW exciton and the cavity mode, which are 92 meV/GPa and 15 meV/Gpa, respectively. The pressure coefficient for 11H transition is in agreement with the studies of strained InGaAs QWs embedded in GaAs barriers. The authors found that the value of the pressure coefficient for the cavity mode is mainly caused by the pressure-induced change of the refractive index of the cavity.

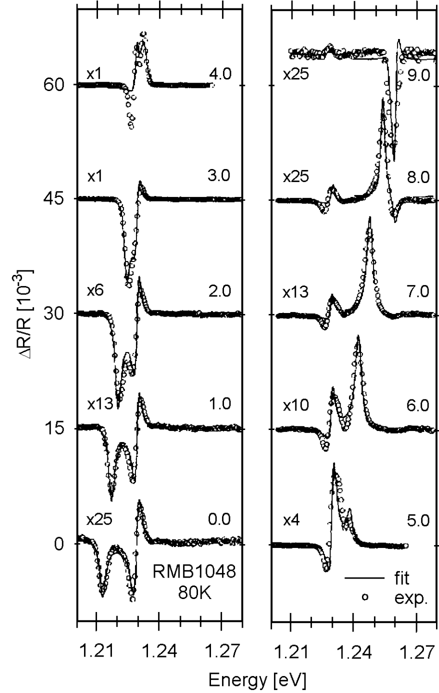

Fig. 44. Position-dependent PR spectra (open circles) of InGaAs/GaAs/AlAs at 80 K. By varying the position of the probe beam on the sample, indicated on the right (in mm), the cavity mode was tuned through resonance with the e1hh1 transition (after Klar et al. [154])

Because of the growth variations across the samples, there may be differences in the cavity mode energy, so that it can be tuned through the position of resonance with the QW ground-state exciton, by varying the position of measurement. Such investigations were performed by Klar et al. [154, 155] on the InGaAs/GaAs/AlAs microcavity VCSEL structures. Figure 44 depicts the PR spectra of VCSEL structure at 80 K in the spectral region near the cavity mode/e1hh1 exciton resonance, as a function of the probe beam position (in mm). The PR spectra clearly show two features which can be assigned to the cavity mode and the e1hh1 exciton. The e1hh1 transition energy does not depend noticeably on the probe position but the cavity feature increases in energy with increasing micrometer setting, crossing the energy of the e1hh1 exciton. The resonance occurs near the 4.0 mm position. From the scaling factor indicated on the left of Fig. 44 it may be seen that the PR signal strength is enhanced at resonance by the factor of 25. Although the PR signals of e1hh1 exciton and cavity mode are clearly distinguishable when they do not overlap, a complicated lineshape arises when they do.

The InGaAs/GaAs/GaAlAs VCSEL structure was investigated using photoreflectance, normal-incidence reflectivity (NIR) and surface photovoltage spectroscopy (SPS) in the temperature range between 15 K and 400 K by Huang et al. [156]. The PR data show only the ground (1C–1H) excitonic transition (and FKOs) while the cavity mode is detected by NIR. The changes of the energy of the ground state and the cavity mode

energy with temperature are shown in Fig. 45. The open circles and squares in Fig. 45 are $E_{1C-1H}(T)$ and $E_{cav}(T)$, respectively, from the SPS investigation.

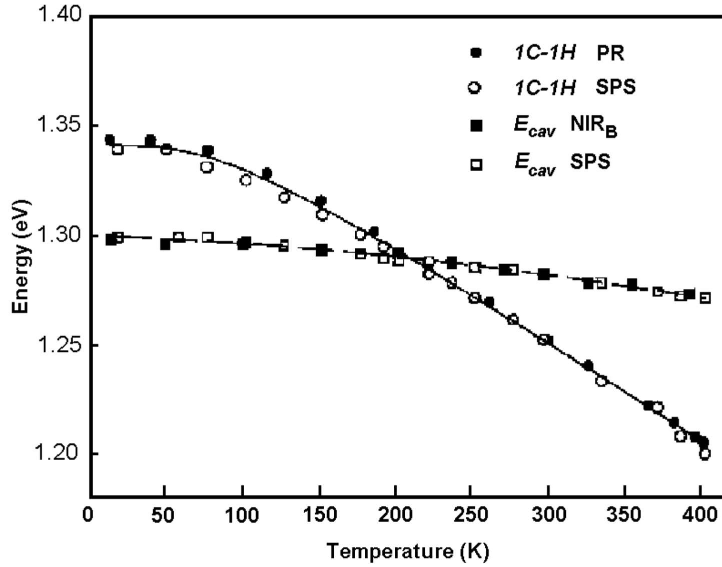

Fig. 45. The changes of the energy of the ground state and the cavity mode energy with temperature. The open circles and squares are $E_{1C-1H}(T)$ $E_{cav}(T)$, respectively, as determined from the SPS. The solid circles and squares are $E_{1C-1H}(T)$ and $E_{cav}(T)$ as determined from PR and NIR, respectively. The solid and dashed lines are least-square fits to a Bose–Einstein-like expression and a quadratic term, respectively (after Huang et al. [156])

The closed circles and squares in Fig. 45 are $E_{1C-1H}(T)$ and $E_{cav}(T)$, respectively, as determined from the PR and NIR spectra. There is a good agreement between the SPS data and the relevant PR/NIR measurements. The solid line in Fig. 45 is a least-squares fit of $E_{1C-1H}(T)$ to a Bose–Einstein-type expression. The quantity $E_{cav}(T)$ has been fit to a quadratic expression. Basing on the above-mentioned structural characteristics for the relevant portions of the sample, the calculated field in the i-GaAs region is 60 kV/cm, what is substantially higher than the field determined from the FKOs.

Pollak et al. [157] investigated multiple quantum well planar emitting laser structures. They performed a room-temperature PR study of two pseudomorphic InGa AsP/InP 1.3 μm MQW laser structures. The structures were fabricated by the MOCVD technique. The first structure was grown on a (001) InP substrate with a n^+ InP buffer. A lattice-matched InGaAsP separate confinement heterostructures (SCH) about 50 nm thick, followed by 6–10 InGaAsP QWs (strained layers) with lattice-matched InGaAsP barriers were grown on the buffer layer. The MQW stack was followed by another lattice-matched InGaAsP SCH and by a p^+ InP layer. The entire structure was covered with a lattice-matched InGaAsP cap.

Figure 46 presents the room-temperature PR spectrum of a structure with 6 nm QWs. The features below 1.1 eV originate from the MQW stack. The signal above 1.3 eV comes from the top InP p^+ layer. The feature exhibits the Franz–Keldysh oscillations which can be used to find information about the built-in electric field in this region. Between these two groups of features is a Franz–Keldysh oscillation originating from the SCH. The built-in electric field in the SCH region is about 41 kV/cm. The band gap of SCH material is 1.104 eV, which means that the materials are lattice-matched.

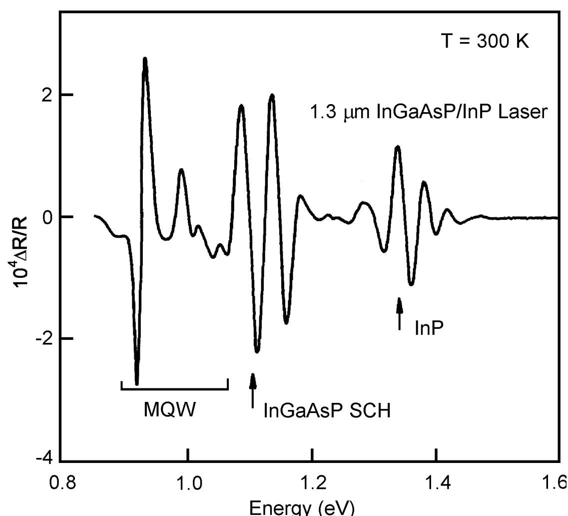

Fig. 46. Photoreflectance spectrum from a pseudomorphic 1.3 μm InGaAsP/InP MQW laser structure with QWs 6 nm wide (after Pollak et al. [157])

A lineshape fit made it possible to accurately determine the energies of five quantum transitions in the MQW. The lowest energy feature is due to the 11H optical transition. This transition is responsible for the lasing frequency of the structure. The energy of 11H transition is 0.925 eV (1.34 μm).

Aigouy et al. [158] evaluated the energy of the fundamental transition (11H) in a 0.98 μm InGaAs/GaAs/InGaP p-i-n quantum well laser, as a function of both the bias applied to the laser, and the position on the laser stripe. They used photoreflectance as well electroreflectance techniques with a spatial resolution of about 10 μm. The laser device was grown by MOCVD on an n^+ GaAs (001) substrate. The active region consisted of two undoped pseudomorphic 7-nm $In_{0.19}Ga_{0.81}As$ QWs separated by a 20-nm undoped GaAs barrier. The active region was surrounded on each side by 85 nm of GaAs, sandwiched between n- and p-type InGaP.

The application of a forward bias results in a blue shift in the 11H transition energy, a decrease in the linewidth and an increase in the amplitude of the spectral feature. Re-

verse bias has the opposite effect. These changes in various parameters are a consequence of the quantum confined Stark effect. At zero bias, the QWs are in the electric field of the p-i-n structure. Application of the bias changes the electric field, giving rise to a shift of the transition energy and to changes of other parameters. Aigouy et al. [158] evaluated the electric field to be 70 kV/cm at zero bias.

They also performed a scan of the 11H transition energy vs. the localization of the probe light spot on the surface of laser structure. They scanned a surface of 750×50 μm and found spatial variations in the 11H transition energy of 6–7 meV over the entire region, which are probably due to inhomogeneities in composition and the electric field distribution.

Dilute-N InGaAs/GaAs based laser structure designed to emit at 1.3 μm was investigated by Choulis et al. [159]. Interdiffusion effects performed by dielectric capping and rapid thermal annealing of the InGaAsP-based laser structures were studied by Kudrawiec et al. [160].

7. Summary

In this article, we presented the review of the experimental, theoretical and instrumentation aspects of photoreflectance spectroscopy. The photoreflectance is extremely useful since it is contactless and does not require any special mounting of the sample. Moreover, photoreflectance can be carried out even at room temperature, providing as much information as other optical methods (PL, PLE) at very low temperatures. It can be utilized under a wide variety of conditions such as elevated temperatures (e.g. in situ monitoring of growth), stress, external electric field or magnetic field.

The emphasis of this paper has been placed on the investigation of the properties of semiconductor bulk, low-dimensional semiconductor structures and semiconductor device structures, mainly in relation to the electronic band structure and its consequences. Refined theories, particularly the low-field first and third derivative formulations and the Franz–Keldysh model of electromodulation, enabled investigators to quantitatively analyze the photoreflectance spectra. The sharp, derivative like features of photomodulated signals made it possible to conveniently investigate the band structure of a wide variety of semiconductors and to explore the influence of different perturbations like temperature, strain, built-in electric field, growth and processing.

Acknowledgements

This work was partly supported by the Centre for Advanced Materials and Nanotechnology, Wrocław University of Technology.

Abbreviations

2DEG – two-dimensional electron gas
CB – conduction band

DBR	– distributed Bragg reflector
DQW	– double quantum well
ER	– electroreflectance
FDGL	– first-derivative Gaussian lineshape
FDLL	– first-derivative Lorenzian lineshape
FFT	– fast Fourier transformation
FKO	– Franz–Keldysh oscillations
HBT	– heterojunction bipolar transistor
HEMT	– high electron mobility transistor
HH or hh	– heavy holes
LH or lh	– light holes
MBE	– molecular beam epitaxy
ML	– monolayer
MOCVD	– metal-organic chemical vapour deposition
MOVPE	– metal-organic vapour-phase epitaxy
MQW	– multiple quantum well
NIR	– normal-incidence reflectivity
PHEMT	– pseudomorphic high electron mobility transistor
PL	– photoluminescence
PLE	– photoluminescence excitation
PR	– photoreflectance
PRD	– photoreflectance-difference
PT	– phototransmittance
QD	– quantum dot
QW	– quantum well
R	– reflectivity
RIE	– reactive ion etching
RTA	– rapid thermal annealing
SCH	– separate confinement heterostructures
SL	– superlattice
SPS	– surface photovoltage spectroscopy
TDFF	– third-derivative functional form
TEM	– transmission electron microscopy
VB	– valence band
VCSEL	– vertical cavity surface emitting laser

References

[1] GLEMBOCKI O.J, SHANBROOK B.V., BOTTKA N., BEARD W.T., COMAS J., Appl. Phys. Lett., 46 (1985), 970.
[2] GLEMBOCKI O.J., SHANABROOK B.V., *Photoreflectance spectroscopy of microstructures*, [in:] D.G. Seiler, C.L Littler. (Eds.), *Semiconductors and Semimetals*, Vol. 36, Academic Press, New York, 1992, p. 221.
[3] POLLAK F.H., GLEMBOCKI O.J., Proc. SPIE, 946 (1988), 2.
[4] POLLAK F.H., QIANG H., YAN D., YIN Y., BOCCIO V.T., Photonics Spectra, 27 (1993), 78.
[5] POLLAK F.H., *Modulation spectroscopy of semiconductors and semiconductor microstructures*, [in:] M. Balkanski (Ed.), *Handbook on Semiconductors*, Vol. 2, Elsevier, Amsterdam, 1994, p. 527.
[6] GLEMBOCKI O.J., Proc. SPIE, 1286 (1990), 2.
[7] MISIEWICZ J., SĘK G., SITAREK P., Optica Applicata, 29 (1999), 327.

[8] MISIEWICZ J., SITAREK P., SĘK G., Opto-electr. Rev., 8 (2000), 1.
[9] PHILLIP H.R., EHRENREICH H., Phys. Rev., 129 (1963), 1550.
[10] ASPNES D.E., STUDNA A.A., Phys. Rev. B 7 (1973), 4605.
[11] KLAR P.J., TOWNSLEY C.M., WOLVERSON D., DAVIES J.J., ASHENFORD D.E., LUNN B., Semicond. Sci. Technol., 10 (1995), 1568.
[12] SERAPHIN B.O., BOTTKA N., Phys. Rev., 145 (1966), 628.
[13] ASPNES D.E., Surface Sci., 37 (1973), 418.
[14] ASPNES D.E., Phys. Rev., 153 (1967), 972.
[15] ASPNES D.E., *Handbook on Semiconductors*, Vol. 2, [in:] M. Balkanski (Ed.), North Holland, Amsterdam, 1980, p. 109.
[16] SHANABROOK B.V., GLEMBOCKI O.J., BEARD W.T., Phys. Rev. B35 (1987), 2540.
[17] HUANG Y.S., QIANG H., POLLAK F.H., LEE J., ELMAN B., J. Appl. Phys., 70 (1991), 3808.
[18] ASPNES D.E., Phys. Rev. B10 (1974), 4228.
[19] SHEN H., POLLAK F.H., Phys. Rev. B42 (1990), 7097.
[20] THEIS W., SANDERS M., LEAK G.D., BAJAJ C.E., MORKOÇ H., Phys. Rev. B37 (1988), 3042.
[21] GLEMBOCKI O.J., SHANABROOK B.V., Proc. SPIE, 794 (1987), 12.
[22] MARKIEWICZ P., Report of the Institute of Physics WUT, SPR 287, (1995), in Polish.
[23] SHEN H., DUTTA M., Appl. Phys. Lett., 57 (1990), 587.
[24] SYDOR M., BADAKHSHAN A., J. Appl. Phys., 70 (1991), 2322.
[25] MISIEWICZ J., ZHENG X.L., BECLA P., HEIMAN D., Solid State Commun., 66 (1988), 351.
[26] ISHITANI Y., HAMADA H., MINAGAWA S., YAGUCHI H., SHIRAKI Y., Jpn. J. Appl. Phys., 36 (1997), 6607.
[27] SHIRAKATA S., CHICHIBU S., ISOMURA S., Jpn. J. Appl. Phys., 36 (1997), 7160.
[28] SHIRAKATA S., CHICHIBU S., ISOMURA S., Jpn. J. Appl. Phys., 36 (1997), 6645.
[29] CHICHIBU S. F., TSUKAZAKI A., KAWASAKI M., TAMURA K., SEGAWA Y., SOTA T., KOINUMA H., Appl. Phys. Lett., 80 (2002), 2860.
[30] SHAN W., LITTLE B.D., SONG J.J., FENG Z.C., SHURMAN M., STALL R.A., Appl. Phys. Lett., 69 (1996), 3315.
[31] SITAREK P., MISIEWICZ J., VEJE E., Proc. SPIE, 3725 (1999), 205.
[32] SITAREK P., MISIEWICZ J., VEJE E., Adv. Mater. Opt. Electr., 10 (1999), 261.
[33] EL ALLALI M., SORENSEN C.B., VEJE E., TIDEMAND-PETERSSON P., Phys. Rev. B 48 (1993), 4398.
[34] PETERS L., PHANEUF L., KAPITAN L.W., THEIS W.M., J. Appl. Phys., 62 (1987), 4558.
[35] LEE C., LEE N.Y., KIM J.E., PARK H.Y., KWAK D.H., LEE H.C., LIM H., J. Appl. Phys., 77 (1995), 6727.
[36] JEZIERSKI K., SITAREK P., MISIEWICZ J., PANEK M., ŚCIANA B., KORBUTOWICZ R., TŁACZAŁA M., Vacuum, 48 (1997), 277.
[37] ZHANG X., CHUA S.J., LIU W., CHONG K.B., Appl. Phys. Lett., 72 (1998), 1890.
[38] BADAKHSHAN A., GLOSSER R., LAMBERT S., J. Appl. Phys., 69 (1991), 2525.
[39] VARSHNI K.P., Physica, 34 (1967), 149.
[40] LAUTENSCHLAGER P., CARRIGA M., CARDONA M., Phys. Rev. B35 (1987), 9174.
[41] LAUTENSCHLAGER P., CARRIGA M., CARDONA M., Phys. Rev. B36 (1987), 4813.
[42] SHEN H., HANG Z., PAN S.H., POLLAK F.H., WOODALL J.M., Appl. Phys. Lett., 52 (1988), 2058.
[43] RÖPPISCHER H., STEIN N., BEHN U., NOVIKOV A.B., J. Appl. Phys., 76 (1994), 4340.
[44] HANG Z., SHEN H., POLLAK F.H., Solid State Commun., 73 (1990), 15.
[45] POLLAK F.H., Proc. SPIE, 1361 (1991), 109.
[46] HANG Z., YAN D., POLLAK F.H., PETTIT G.D., WOODALL J.M., Phys. Rev. B44 (1991), 10546.
[47] CHEN J.H., CHI W.S., HUANG Y.S., YIN Y., POLLAK F.H., PETTIT G.D., WOODALL J.M., Semicon. Sci. Technol., 8 (1993), 1420.
[48] CHI W.S., HUANG Y.S., QIANG H., POLLAK F.H., PETTIT D.G., WOODALL J.M., Jpn. J. Appl. Phys., 33 (1994), 966.

[49] KUAN H., SU Y.K., WU T.S., HUANG Y.S., CHI W.S., Sol. State Electron., 39 (1996), 885.
[50] BOUAMAMA K., HÖRIG W., NEUMANN H., Semicond. Sci. Technol., 13 (1998), 75.
[51] BELLANI V., AMIOTTI M., GEDDO M., GUIZZETTI G., LANDGREN G., Mat. Res. Soc. Symp. Proc., 324 (1994), 225.
[52] GEDDO M., BELLANI V., GUIZETTI G., Phys. Rev. B50 (1994), 5456.
[53] MUNOZ M., POLLAK F.H., ZAKIA M.B., PATEL N. B., HERRERA-PEREZ J. L., Phys. Rev. B62 (2000), 16600.
[54] PAL U., HERRERA PEREZ J.L., PIQUERAS J., DIEGUEZ E., Mater. Sci. Eng. B42 (1996), 297.
[55] SHEN S.C., ZHANG L.J., LU W., BICKNELL-TASSIUS R.N., Sol. State Electron., 37 (1994), 1087.
[56] LIN C.H., SINGER K.E., EVANS-FREEMAN J.H., HEATH K., MISSOUS M., Semicond. Sci. Technol., 12 (1997), 1619.
[57] LI C.F., HUANG Y.S., MALIKOVA L., POLLAK F.H., Phys. Rev. B55 (1997), 9251.
[58] GLEMBOCKI O.J., Mater. Res. Soc. Symp. Proc., 160 (1990), 631.
[59] SĘK G., TALIK S., MISIEWICZ J., RADZIEWICZ D., TŁACZAŁA M., PANEK M., KORBUTOWICZ R., Electron Technol., 30 (1997), 366.
[60] SĘK G., MISIEWICZ J., RADZIEWICZ D., TŁACZAŁA M., PANEK M., KORBUTOWICZ R., Vacuum, 50 (1998), 219.
[61] FITZGERALD E.A., *Properties of Lattice-Matched and Strained Indium Galium Arsenide*, [in:] P. Bhattacharaya (Ed.), IEE EMIS Datareviews Series 8, 1993, p. 6.
[62] LASTRAS-MARTINEZ L.F., CHAVIRA-RODRIGUEZ M., LASTRAS-MARTINEZ A., BALDERAS-NAVARRO R.E., Phys. Rev. B66 (2002), 075315.
[63] LASTRAS-MARTINEZ A., BALDERAS-NAVARRO R.E., LASTRAS-MARTINEZ L.F., VIDAL M.A., Phys. Rev. B59 (1999), 10234.
[64] ANDREANI L.C., DE NOVA D., DI LERNIA S., GEDDO M., GUIZETTI G., PATRINI M., BOCCHI C., BOSACCHI A., FERRARI C., FRENCHI S., J. Appl. Phys., 78 (1995), 6745.
[65] RADHAKRISHNAN K., YOON S.F., LI H.M., HAN Z.Y., ZHANG D.H., J. Appl. Phys., 76 (1994), 246.
[66] MO S., PEINER E., BARTELS A., TANG G.P., SCHLACHETZKI A., KUZMENKO R., HILDEBRANDT S., SCHREIBER J., Jpn. J. Appl. Phys., 35 (1996), 4238.
[67] LEE J.H., JANG K.S., SHIN C.S., PARK H.L., KIM T.W., J. Appl. Phys., 75 (1994), 8216.
[68] HAN M.S., KANG T.W., KIM T.W., Solid. Sate Commun., 105 (1998), 709.
[69] CHICHIBU S., SHIKANAI A., AZUHATA T., SOTA T., KURAMATA A., HORINO K., NAKAMURA S., Appl. Phys. Lett., 68 (1996), 3766.
[70] TCHOUNKEU M., BRIOT O., GIL B., ALEXIS J.P., AULOMBARD R.L., J. Appl. Phys., 80 (1996), 5352.
[71] SHIKANAI A., AZUHATA T., SOTA T., CHICHIBU S., KURAMATA A., HORINO K., NAKAMURA S., J. Appl. Phys., 81 (1997), 417.
[72] ALEMU A., GIL B., JULIER M., NAKAMURA S., Phys. Rev. B57 (1998), 3761.
[73] SITAREK P., KUDRAWIEC R., SĘK G., MISIEWICZ J., PASZKIEWICZ R., KORBUTOWICZ R., PASZKIEWICZ B., TŁACZAŁA M., Mat. Sci. Eng. B82 (2001), 209.
[74] KUDRAWIEC R., SĘK G., MISIEWICZ J., PASZKIEWICZ R., PASZKIEWICZ B., TŁACZAŁA M., Mat. Sci. Eng. B96 (2002), 284.
[75] WANG D.P., SHEN T.L., Jpn. J. Appl. Phys., 33 (1993), 1253.
[76] JEZIERSKI K., MISIEWICZ J., MARKIEWICZ P., PANEK M., ŚCIANA B., TŁACZAŁA M., KORBUTOWICZ R., Phys. Stat. Sol. (a), 147 (1995), 467.
[77] JEZIERSKI K., SITAREK P., MISIEWICZ J., PANEK M., ŚCIANA B., KORBUTOWICZ R., TŁACZAŁA M., Vacuum, 48 (1997), 277.
[78] WANG Z., PAN S., HUANG S., ZHANG C., MU S., ZHOU X., JIAN J., XU G., CHEN Z., J. Phys. D: Appl. Phys., 26 (1993), 1493.
[79] WANG Z., PAN S., MU S., Phys. Stat. Sol. (a), 140 (1993), 135.
[80] JEZIERSKI K., SITAREK P., MISIEWICZ J., PANEK M., ŚCIANA B., KORBUTOWICZ R., TŁACZAŁA M., Acta Phys. Pol., 88 (1995), 751.
[81] YOSHITA M., TAKAHASHI T., Appl. Surf. Sci., 115 (1997), 347.

[82] SCHEIBLER H.E., ALPEROVICH V.L., JAROSHEVICH A.S., TEREKHOV A.S., Phys. Stat. Sol. (a), 152 (1995), 113.
[83] WANG D. P., CHEN C. T., Appl. Phys. Lett., 67 (1995), 2069.
[84] WANG D.P., CHEN C.C., SHEN T.L., HSU T.M., LEE W.C., J. Appl. Phys., 80 (1996), 6980.
[85] NUKEAW J., MATSUBARA N., FUJIWARA Y., TAKEDA Y., Appl. Surf. Sci., 117/118 (1997), 776.
[86] NUKEAW J., FUJIWARA Y., TAKEDA Y., Jpn. J. Appl. Phys., 36 (1997), 7019.
[87] CHANG W.H., HSU T.M., LEE W.C., CHUANG R.S., J. Appl. Phys., 83 (1998), 7873.
[88] NOWACZYK M., SĘK G., MISIEWICZ J., ŚCIANA B., RADZIEWICZ D., TŁACZAŁA M., Thin Solid Films, 380 (2000), 243.
[89] YIN X., CHEN H.M., POLLAK F.H., CHAN Y., MONTANO P.A., KIRCHNER P.D., PETTIT G.D., WOODALL J.M., J. Vac. Sci. Technol., A10 (1992), 131.
[90] OH Y.T., BYUN S.C., LEE B.R., KANG T.W., HONG C.Y., PARK S.B., LEE H.K., KIM T.W., J. Appl. Phys., 76 (1994), 1959.
[91] YAN D., POLLAK F.H., CHIN T.P., WOODALL J.M., Phys. Rev. B52 (1995), 4674.
[92] NAKANISHI H., WADA K., WALUKIEWICZ W., J. Appl. Phys., 78 (1995), 5103.
[93] MOCHIZUKI Y., ISHII T., MIZUTA M., MOCHIZUKI A., LANGER J. M., Phys. Rev. Lett., 77 (1996), 3601.
[94] LOPEZ-LOPEZ M., MELENDEZ-LIRA M., GOTO S., Appl. Phys. Lett., 71 (1997), 338.
[95] LEE W.C., HSU T.M., WANG S.C., CHANG M.N., CHYI J.I., J. Appl. Phys., 83 (1998), 486.
[96] BADAKHSHAN A., ENGLAND J.L., THOMPSON P., CHEUNG P., YANG C.H., ALAVI K., J. Appl. Phys., 81 (1997), 910.
[97] GLEMBOCKI O.J., TUCHMAN J.A., DAGATA J.A., KO K.K., PANG S.W., STUTZ C.E., Appl. Phys. Lett., 73 (1998), 114.
[98] PAGET D., KIERREN B., HOUDRÉ R., J. Vac. Sci. Technol. A16 (1998), 2350.
[99] KLAR P.J., GRÜNING H., GÜNGERICH M., HEIMBRODT W., KOCH J., TORUNSKI T., STOLZ W., POLIMENI A., CAPIZZI M., Phys. Rev. B67 (2003), 121206(R).
[100] KUDRAWIEC R., SĘK G., MISIEWICZ J., LI L.H., HARMAND J.C., Appl. Phys. Lett., 83 (2003), 1379.
[101] CARDONA M., *Modulation Spectroscopy*, Academic Press, New York, 1969.
[102] SITAREK P., SĘK G., MISIEWICZ J., CHENG T.S., Vacuum, 50 (1998), 203.
[103] SITAREK P., SĘK G., MISIEWICZ J., CHENG T.S., Inst.Phys.Conf. Ser., 152 (1998), 657.
[104] BASTARD G., *Wave Mechanics Applied to Semiconductor Heterostructures*, Les Editions de Physique, Paris, 1992.
[105] ZUCKER J.E., PINCZUK A., CHEMLA D.S., GOSSARD A.C., WIEGMANN W., Phys. Rev. B29 (1984), 7065.
[106] SONG J.J., YOON Y.S., FEDOROWSKY A., KIM Y.B., SCHULMAN J.N., TU C.W., HUANG D.M., MORKOÇ H., Phys. Rev. B 34 (1986), 8958.
[107] REDDY U.K., JI G., HENDERSON T., MORKOÇ H., SCHULMAN J.N., J. Appl. Phys., 62 (1987), 145.
[108] JI G., DOBBELAERE W., HUANG D., MORKOÇ H., Phys. Rev. B39 (1989), 3216.
[109] SHEN H., PAN S.H., HANG Z., POLLAK F.H., SACKS R.N., Solid State Commun., 65 (1988), 929.
[110] TSENG S. M., CHEN Y. F., CHENG Y. T., HSU C. W., HUANG Y. S., LIN D. Y., Phys. Rev. B64 (2001), 195311.
[111] PAN S.H., SHEN H,, HANG Z., POLLAK F.H., ZHUANG W., XU Q., ROTH A.P., MASUT R.A., LACELLE C., MORRIS D., Phys. Rev. B38 (1988), 3375.
[112] SĘK G., MISIEWICZ J., RADZIEWICZ D., TŁACZAŁA M., PANEK M., KORBUTOWICZ R., Vacuum, 50 (1998), 199.
[113] KUDRAWIEC R., SĘK G., RUDNO-RUDZIŃSKI W., MISIEWICZ J., WÓJCIK J., ROBINSON B.J., THOMPSON D.A., MASCHER P., Acta Phys. Pol. A102 (2002), 649.
[114] SITAREK P., RYCZKO K., SĘK G., MISIEWICZ J., FISCHER M., REINHARDT M., FORCHEL A., Solid State Electr., 47 (2003), 489.
[115] MISIEWICZ J., SITAREK P., RYCZKO K., KUDRAWIEC R., FISCHER M., REINHARDT M., FORCHEL A., Microelectronics J., 34 (2003), 737.

[116] HEROUX J. B., YANG X., WANG W. I., J. Appl. Phys., 92 (2002), 4361.
[117] KUDRAWIEC R., SĘK G., MISIEWICZ J., GOLLUB D., FORCHEL A., Appl. Phys. Lett., (2003), in press.
[118] KUDRAWIEC R., SĘK G., RYCZKO K., MISIEWICZ J., SUNDGREN P., ASPLUND C., HAMMAR M., Solid State Commun., 127 (2003), 613.
[119] CHOULIS S.A., HOSEA T.J.C., TOMIĆ S., KAMAL-SAADI M., ADAMS A.R., O'REILLY E.P., WEINSTEIN B.A., KLAR P.J., Phys. Rev. B66 (2002), 165321-1.
[120] KUDRAWIEC R., SĘK G., RYCZKO K., MISIEWICZ J., FORCHEL A., Superlattces and Microstructures, 32 (2002), 19.
[121] WETZEL C., TAKEUCHI T., AMANO H., AKASAKI I., Phys Rev. B61 (2000), 2159.
[122] WETZEL C., TAKEUCHI T., AMANO H., AKASAKI I., Phys Rev. B62 (2000), R13302.
[123] SĘK G., RYCZKO K., KUBISA M., MISIEWICZ J., KOETH J., FORCHEL A., Opto-Electr. Rev., 7 (1999), 117.
[124] SĘK G., RYCZKO K., MISIEWICZ J., BAYER M., WANG T., FORCHEL A., Acta Phys. Pol. A100 (2001), 417.
[125] CHO Y-H., KIM D-S., JHE W., Appl. Phys. Lett., 78 (2001), 2306.
[126] QIANG H., POLLAK F.H., TANG Y.S., WANG P.D., SOTOMAYOR TORRES C.M., Appl. Phys. Lett., 64 (1994), 2830.
[127] GUMBS G., HUANG D., QIANG H., POLLAK F.H., WANG P.D., SOTOMAYOR TORRES C.M., HOLLAND M.C., Phys. Rev. B50 (1994), 10962.
[128] WANG D.P., SOTOMAYOR TORRES C.M., HOLLAND M.C., QIANG H., POLLAK F.H., GUMBS G., Mat. Res. Soc. Symp. Proc., 324 (1994), 187.
[129] KLAR P.J., WOLVERSON D., ASHENFORD D.E., LUNN B., HENNING T., Semicond. Sci. Technol., 11 (1996), 1863.
[130] ULRICH C., VES S., GONI A.R., KURTENBACH A., SYASSEN K., EBERL K., Phys. Rev. B52 (1995), 12212.
[131] SĘK G., MISIEWICZ J., RYCZKO K., KUBISA M., HEINRICHSDORFF F., STIER O., BIMBERG D., Solid State Commun., 110 (1999), 657.
[132] SĘK G., RYCZKO K., MISIEWICZ J., BAYER M., KLOPF F., REITHMAIER J. P., FORCHEL A., Solid State Commun., 117 (2001), 401.
[133] MISIEWICZ J., SĘK G., KUDRAWIEC R., Current Appl. Phys., (2003), in press.
[134] SOARES J.A.N.T., BELIAEV D., ENDERLEIN R., SCOLFARO L.M.R., SAITO M., LEITE J.R., Mat. Sci. Eng., B35 (1995), 267.
[135] ENDERLEIN R., Phys. Stat. Sol. (b), 194 (1996), 257.
[136] SĘK G., MISIEWICZ J., CHENG T.S., Adv. Mater. Opt. Electron., 7 (1997), 241.
[137] YIN Y., QIANG H., POLLAK F.H., STREIT D.C., WOJTOWICZ M., Appl. Phys. Lett., 61 (1992), 1579.
[138] YIN Y., QIANG H., YAN D., POLLAK F.H., NOBLE T.F., Semicond. Sci. Technol., 8 (1993), 1599.
[139] HAN A.C., WOJTOWICZ M., PASCUA D., BLOCK T.R., STREIT D.C., J. Appl. Phys., 82 (1997), 2607.
[140] BOTTKA N., GASKILL D.K., WRIGHT P.D., KALISKI R.W., WILIAMS D.A., J. Cryst. Growth, 107 (1991), 893.
[141] SUN W.D., POLLAK F.H., J. Appl. Phys., 83 (1998), 4447.
[142] YAN D., POLLAK F.H., BOCCIO V.T., LIN C.L., KIRCHNER P.D., WOODALL J.M., GEE R.C., ASBECK P.M., Appl. Phys. Lett., 61 (1992), 2066.
[143] HSU K.T., CHEN Y.H., CHEN K.L., LIN H.H., JAN G.J., Appl. Phys. Lett., 64 (1994), 1974.
[144] CHEN Y.H., HSU K.T., CHEN K.L., LIN H.H., JAN G.J., Jpn. J. Appl. Phys., 33 (1994), 2448.
[145] CHEN Y.H., JAN G.J., J. Appl. Phys., 77 (1995), 6681.
[146] CHEN Y.H., JAN G.J., IEEE J. Quantum Electron., 33 (1997), 574.
[147] CHEN K.L., LIN H.H., JAN G.J., CHEN Y.H., Tseng P.K., J. Appl. Phys., 78 (1995), 4035.
[148] LIN C. J., HUANG Y. S., LI N. Y., LI P. W., TIONG K. K., J. Appl. Phys., 90 (2001) 4565.
[149] BERGER P.D., BRU C., BENYATOU T., CHENEVAS-PAULE A., GROSSE P., Proc. SPIE, 2397 (1995), 726.
[150] BERGER P.D., BRU C., BENYATOU T., GUILLOT G., CHENEVAS-PAULE A., COUTURIER L., GROSSE P., Appl. Phys. Lett., 68 (1996), 4.
[151] KLAR P.J., ROWLAND G., SALE T.E., HOSEA T.J.C., GREY R., Phys. Stat. Sol. (a), 170 (1998), 145.

[152] KLAR P.J., VINCENTE P.M.A., SALE T.E., HOSEA T.J.C., ADAMS A.R., RAYMOND A., Solid State Commun., 107 (1998), 97.
[153] GHOSH S., HOSEA T.J.C., CONSTANT S.B., Appl. Phys. Lett., 78 (2001), 3250.
[154] KLAR P.J., ROWLAND G., THOMAS P.J.S., ONISCHENKO A., SALE T.E., HOSEA T.J.C., GREY R., Phys. Rev. B59 (1999), 2894.
[155] KLAR P.J., ROWLAND G., THOMAS P.J.S., ONISCHENKO A., SALE T.E., HOSEA T.J.C., GREY R., Phys. Rev. B59 (1999,) 2902.
[156] HUANG Y. S., MALIKOVA L., POLLAK F.H., SHEN H., PAMULAPATI J., NEWMAN P., Appl. Phys. Lett., 77 (2000), 37.
[157] POLLAK F.H., KRYSTEK W., LEIBOVITCH M., MALIKOVA L., HYBERTSEN M.S., LUM R., VANDENBERG J.M., REYNOLDS C.L., Proc. SPIE, 2693 (1996), 455.
[158] AIGOUY L., POLLAK F.H., GUMBS G., Appl. Phys. Lett., 70 (1997), 2562.
[159] CHOULIS S.A., TOMI S., O'REILLY E.P., HOSEA T.J.C., Solid State Commun., 125 (2003), 155.
[160] KUDRAWIEC R., SĘK G., RYCZKO K., RUDNO-RUDZIŃSKI W., MISIEWICZ J., WÓJCIK J., ROBINSON B.J., THOMPSON D.A., MASCHER P., Physica E17 (2003), 602.

Figures were reproduced by the permission of: American Institute of Physics (Figs. 6, 7, 28, 36, 39, 45), American Physical Society (Figs. 8, 9, 14, 20, 21, 29, 44), Elsevier Science B.V. (Figs. 1, 33, 37, 43), International Society for Optical Engineering (SPIE) (Figs. 22, 40, 41, 46), Japanese Journal of Applied Physics (Fig. 38), Wiley-VCH Verlag GmbH & Co. KGaA (Fig. 42), Materials Research Society (Fig. 10).

Received 23 April 2003
Revised 19 May 2003

Materials Science, *Vol. 21*, *No. 3*, *2003*

Combined SNOM/AFM microscopy with micromachined nanoapertures

JACEK RADOJEWSKI[1*], PIOTR GRABIEC[2]

[1]Faculty of Microsystem Electronics and Photonics, Wrocław University of Technology, Wybrzeże Wyspiańskiego 27, 50-370 Wrocław, Poland

[2]Institute of Electron Technology, al. Lotników 32/46, 02-668 Warsaw, Poland

We describe a new combined SNOM/AFM cantilever probe with the aperture FIB micromachined in a hollow metal pyramid fabricated on its end. The cantilever can be used in a microscopy set-up with the optical or piezoresistive AFM detection system. A processing sequence proposed in the article offers a high reproducibility in batch processing typical of semiconductor technology. Moreover, the angle of the apex cone is close to 50° which renders it possible to obtain a high-aperture optical throughoutput. The probe construction, manufacturing and its basic optical parameters are described.

Key words: *AF; SNOM microscopy; cantilever technology; nanoaperture*

1. Introduction

The concept of the near-field optical microscopy (SNOM) was first published by Synge [1] in 1928. In 1984 Pohl et al. [2] and Lewis et al. [3] used this technology in practice. Since that time many authors have reported their SNOM systems, mainly based on optical waveguides with the nanoaperture fabricated on the end much smaller than the light wavelength λ [4, 5]. The tips usually used in this method are tapered optical fibres coated with metal films in such a way that the very end of the tip is free of the metal layer. The use of nanoaperture as a local probe makes it possible to overcome the $\lambda/2$ diffraction limit which occurs if the light is detected in far field, i.e., when the detector distance is much larger than the wavelength λ of the light used in the experiment. In SNOM systems such a local probe is raster-scanned over the sample surface at a distance much smaller than λ. A simultaneous detection of transmitted, reflected or scattered light makes it possible to image optical properties of the sample.

[*]Corresponding author, e-mail: jacek.radojewski@pwr.wroc.pl.

The main drawback of the tapered-fibre based SNOM systems is the resolution limited by 'shear force' mechanism used to control sample–tip distance [6]. This technique uses an optical fibre probe vibrating parallel to the surface under the test in its dominant mechanical resonance. The vibration amplitude is a few nanometres. The amplitude and phase change due to tip–surface distance variation is used for the distance regulation. Unfortunately, the fabrication process of tapered fibres renders very small angles of the apex resulting in a significant squeezing of the light passing through the tapered region and the aperture itself and consequently in a relatively low throughoutput of the aperture.

In the present paper, we demonstrate a novel technology of combined SNOM /AFM cantilever. Our earlier approach [7] allowed fabrication of a piezo-SNOM/AFM probe but the reproducibility of the process and optical quality of the device were unsatisfactory. In this paper, we report an innovative processing sequence with direct FIB aperture drilling. It offers highly reproducible batch processing, typical of the semiconductor technology and renders it possible to produce cantilevers playing the role of AFM detectors as well as nanoaperture detectors. Moreover, the illumination of the aperture is easier because of wide input opening and its large cone angle. The throughoutput is in the range of 10^{-5} and higher for aperture diameter of 50 nm.

Apertures in hollow pyramids have been formed by a direct ion beam drilling with a focused beam of 30 keV Ga^{+} ions. Direct FIB drilling is a reproducible process for hole formation in the 30–100 nm diameter range. Formation of smaller apertures is possible if special FIB drilling/deposition procedure is applied. Our apertures possess excellent optical properties making it possible to use them in polarization-dependent experiments, as was suggested by Betzig et al. [8], Valaskovic et al. [9] and Husler et al. [10]

2. SNOM/AFM cantilever technology

Based on our experience and having considered examples reported in the literature [11, 12], we have developed an innovative processing sequence, which offers a highly reproducible batch processing, typical of semiconductor technology and silicon micromechanics rendering it possible to produce cantilevers playing the role of AFM detectors as well as optical photo-detectors or nanoaperture detectors.

A number of functional components were integrated in one silicon chip to form the microprobe. The microprobe forms a cantilever beam with a hollow pyramid at the end. A set of force sensitive piezoresistors, placed in the base of the beam, allows detection of small deflections of the beam. A tip-shape platform acts as an atomic force sensitive unit, while a nano-hole in the platform serves for near field optical measurements.

The fabrication process starts from pad oxide formation followed by LPCVD nitride deposition. Then a rectangular mesa in a future beam area is defined and plasma

etched (Fig. 1a). The mesa level remains elevated several micrometers over the whole surface. Next, a sequence of oxidation, photolithography and implantation is used to form a set of piezoresistors in the base of the beam area (Fig. 1b). The post -implantation oxidation is optimized to protect effectively the probe surface against later etching processes. In the next step, membrane areas are defined in the nitride film at the back sides of the wafer, and subsequently etched in hot KOH solution while the front side of the wafer is protected by a special chuck. The membrane thickness of 30 μm (as measured in the thickest part, i.e. in the mesa area) is achieved by etching (Fig. 1c). In the following sequence an inverse hollow pyramid is created.

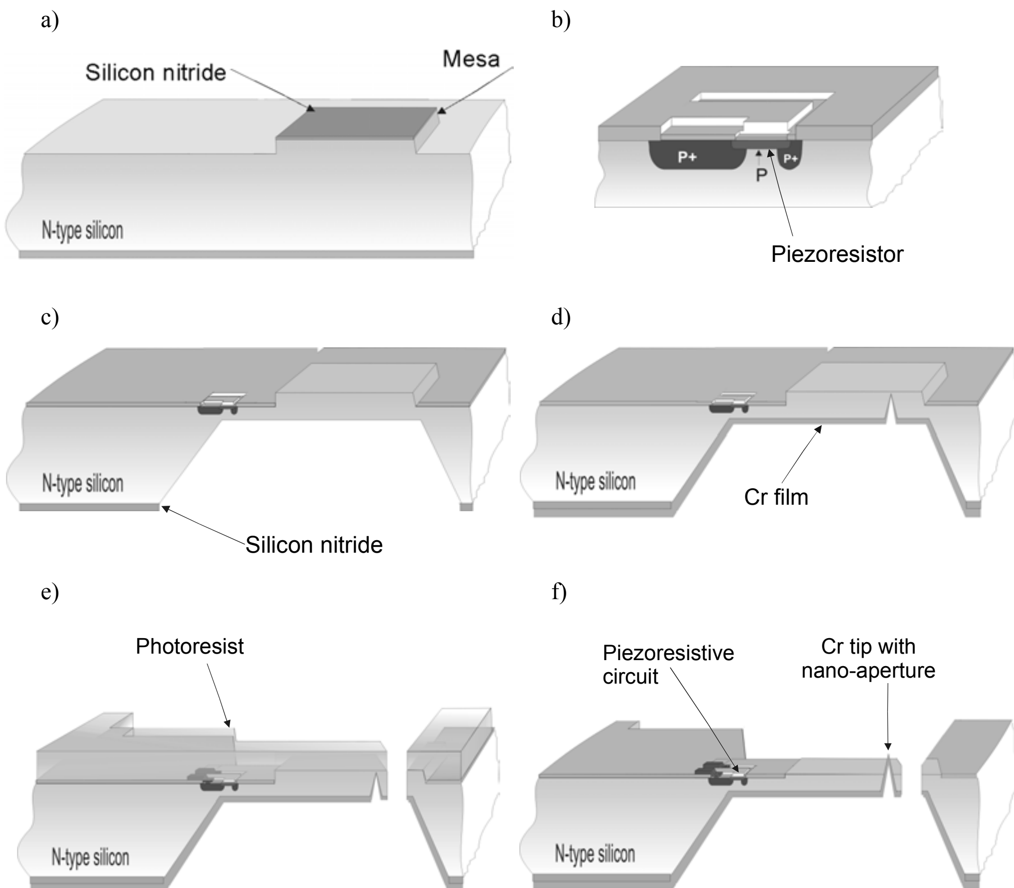

Fig. 1. Scheme of the process sequence of the microprobe fabrication. See text for details

First, a thin nitride layer is LPCVD deposited. A square contour is photolithographically defined at the back side of the membrane, in the future tip location, using SU-8 process followed by thick oxidation, resulting in a LOCOS-like shape. Next, both the nitride and oxide layers are dry etched away from the square area on the back

side of the membrane. Finally, an inverse pyramid hollow is etched in this place where bare silicon was previously exposed. Photolithographic opening of contacts to piezoresistors, followed by the creation of metal connections in standard CMOS IC's processing sequence, completes the formation of the piezoresistor set. Then, the back side of the membrane, including pyramid walls, is covered with chromium layers in magnetron sputtering process (Fig. 1d). In the next step, the probe shape is photolithographically defined at the front side of the wafer, followed by silicon plasma etching and chromium etching (Fig. 1e). Finally, a mask-less plasma etching of the nitride /pad oxide sandwich from the top of the mesa structure is performed, followed by a deep plasma silicon etching, resulting in exposition of the metal pyramid in the former mesa area (Fig. 1f). SEM images of the main microprobe regions are shown in Fig. 2.

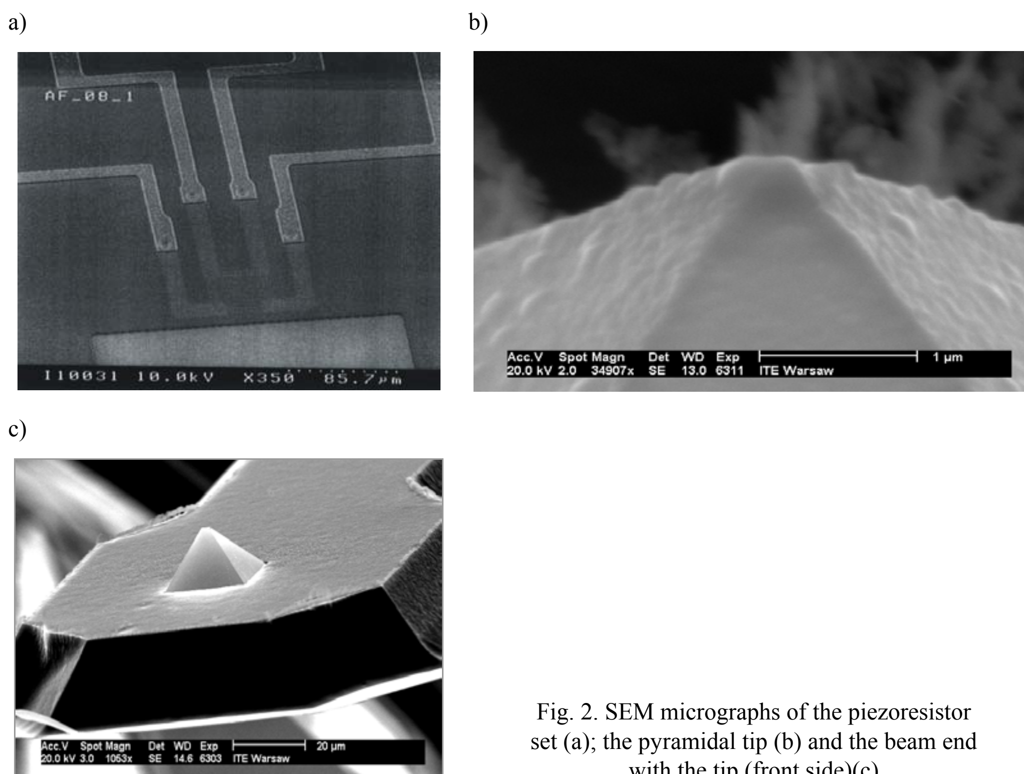

Fig. 2. SEM micrographs of the piezoresistor set (a); the pyramidal tip (b) and the beam end with the tip (front side)(c)

Creation of a small aperture of several tens of nanometres is the last step of the SNOM/AFM microprobe fabrication. A FIB direct ion beam drilling with a focused beam of 30 keV gallium ions is applied to produce a hole in the hollow chromium pyramid tip. The direct FIB drilling is a reproducible process for a hole formation in the 30–100 nm diameter range (Fig. 3). The ion dose for sputtering the hole is about 2×10^9 ions. The positions of specimens in regular arrays can be dialed in automatically, enabling a rapid processing of the samples. The FIB drilling experiments

indicate an aspect ratio limit of about 5:1 but the hole size is independent of the aspect ratio for holes of diameters below 100 nm. The available FIB systems equipped with an *xy*-stage and image recognition allows drilling 360 sensor Cr pyramids on the wafer at a reasonably short time with an excellent reproducibility (size deviation and

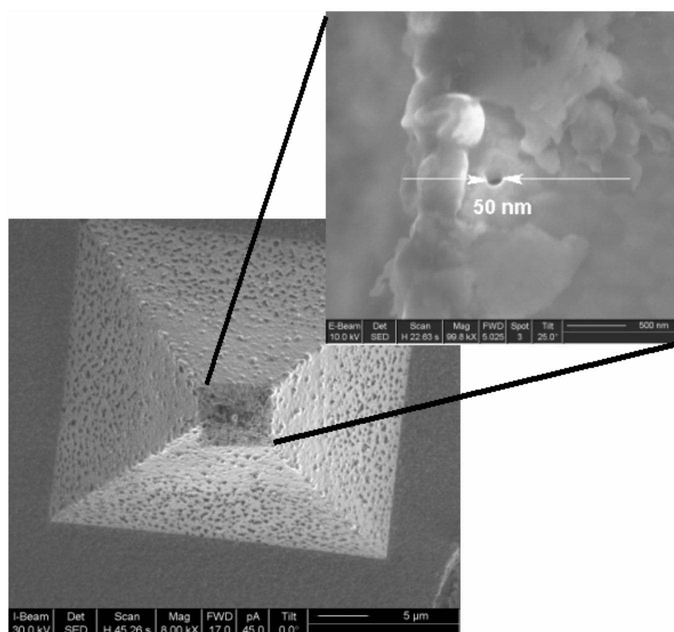

Fig. 3. SEM image of the tip shape
and the aperture obtained by the FIB method

circularity). For the beam geometry of l = 600 μm, b = 210 μm and d = 15 μm we obtained cantilevers with the spring constant k = 113 N/m and the resonance frequency f_r = 50 kHz.

3. Aperture verification

Looking at the SEM images of the tips etched by the FIB method described above (Fig. 3), one can see a well defined aperture on the end face of the pyramidal shaped tip, placed on the end of the piezoelectric cantilever. For a final verification of our tips, we performed polarization measurements of the aperture. For this purpose, we used helium-neon laser light (λ = 0.6328 μm) with the beam power of P = 5 mW. The light beam was coupled to the aperture via a microscopic objective of NA = 0.5. We used a λ/4 plate to convert the linear polarization of the incident light into the circular one, in order to have a possibility to control the input light polarization via a polarizer. The degree of polarization of the light which passed the nanoaperture was tested by an

analyzer placed between the aperture and the photomultiplier. A dummy sample was used in close proximity to the aperture for field conversion purpose (Fig. 4).

From the theoretical point of view [13], an ideally symmetrical aperture possesses two peaks of intensities associated with depolarization fields. They are generated in the regions where the incident field is normal to the core/coating interface. The depolarization field rotates following the orientation of the incident light polarity. As a result, a symmetrical behaviour should be observed in far field for symmetrical apertures. An elliptical or rough rim of aperture coming from metal grains strongly changes the field distribution resulting in an asymmetry in far field [14].

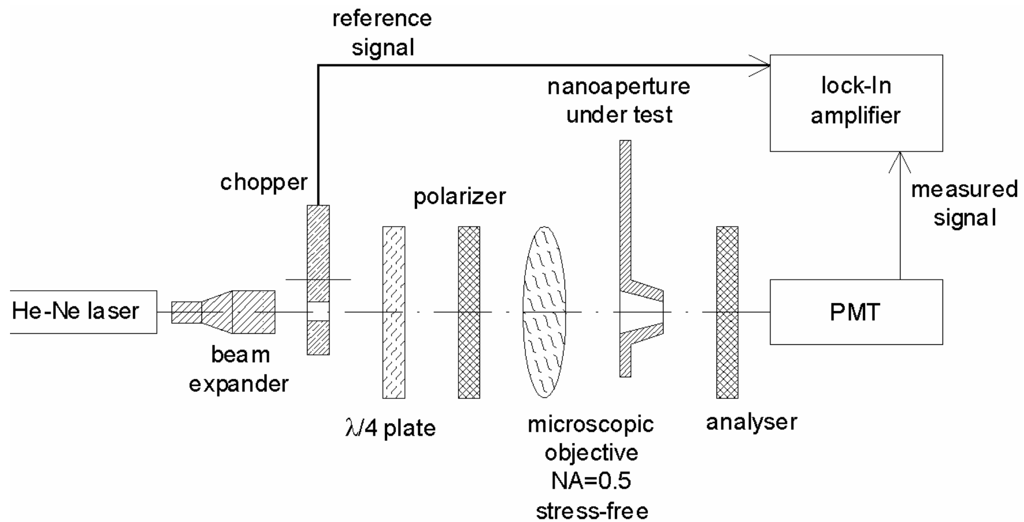

Fig. 4. Set-up for measurements of the polarization behaviour of fabricated apertures

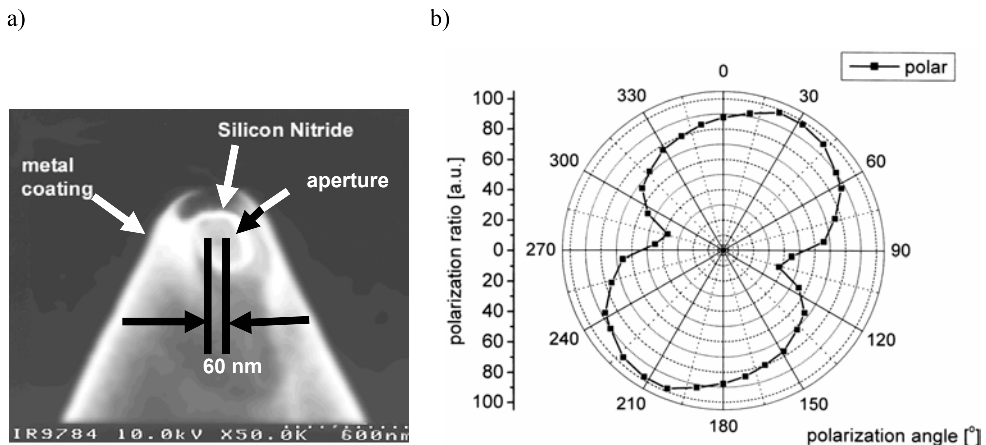

Fig. 5. SNOM nanoaperture probe from the authors' laboratory [7] (a)
and a polarization ratio of 60/80 nm aperture with elliptical shape (b)

In the beginning of our measurements, we tested cantilevers described in [7], elaborated in this laboratory in 2001. After precise measurements of aperture we found an elipticity in its shape. In Fig. 5a, a SEM image of the 60/80 nm tip aperture, and in Fig. 5b – the corresponding polarization ratio graph are shown. We found that the minimum polarization ratio was about 1:38 and the maximum exceeded 1:98. After improving our technology, we expected to obtain better results (minimum to maximum polarization ratio difference factor less than two) due to a better circularity of the aperture opening. In Fig 6a, a relative polarization ratio for the aperture fabricated using our new batch technology is presented. In this case, we found the polarization ratio between 1:77 and 1:98. Thus, a significant improvement of optical properties of our SNOM cantilevers was confirmed.

a)

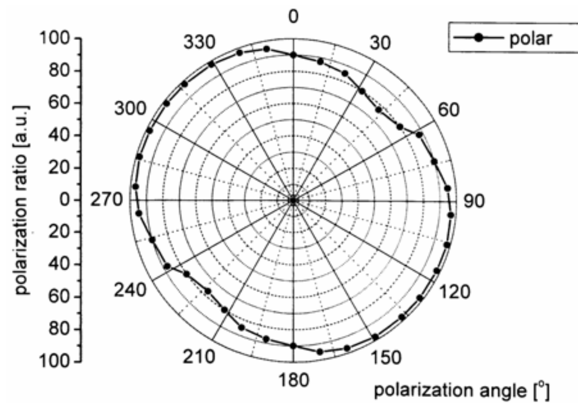

b)

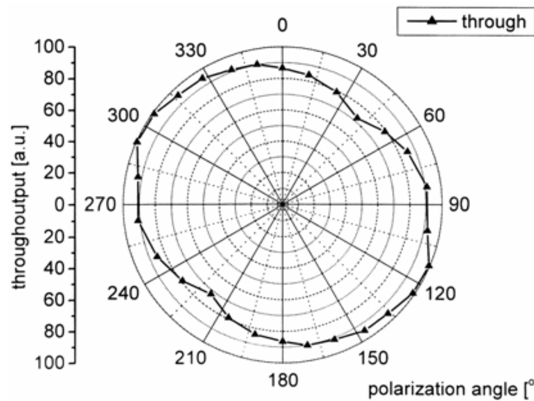

Fig. 6. Normalized polarization ratio of 50 nm aperture fabricated with the improved technology (a) and relative throughoutput of the 50 nm aperture (b)

The transmission coefficient of the apertures shows a strong dependence on its diameter. For example, for the cone angle 50° it is of the order of 10^{-3} for the aperture diameter of 100 nm, decreasing to 5×10^{-7} for the aperture diameter of 10 nm [15]. In our case, we obtained a 50-nm aperture throughoutput ratio of 5×10^{-5} with the values lying within 30% with respect to the polarization direction (Fig. 6b).

4. Microscope measurements

4.1. Microscope set-up

The measuring set-up of our SNOM microscope (Fig. 7) consists of two parts. One is a head support with a piezotable (PXY100, Piezojena) used for fine sample movement (scanning) in the *XY* plane (up to 100×100 μm). The piezotable can be additionally moved in the *XY* plane by means of two DC motorized micrometric screws (Owis). These coarse movements, which can be done on the distances of 5×5 mm, are used to select a place of interest over the sample for the subsequent precise scanning. The head standing on three legs on the head support can be rotated with respect to the sample fixed by *Z* fine movement piezostack to the fine *XY* movement piezotable. One of these legs is a DC motorized micrometric screw which is used to perform coarse *Z* movements of the head (cantilever) with respect to the sample. A fine *Z* movement is realized by the piezostack *Z* mentioned above. The cantilever bending due to force interactions with the sample surface is detected by a standard technique using the light reflected from the cantilever surface and detected by a quadrant detector. For the cantilever in position of a desired interaction force, the light spot is centred on the detector in such a way that the photocurrents from each quadrant are equal. Any movement of the cantilever, detected as a current imbalance signal, is used in a closed feedback loop with the *Z* piezostack to stabilize the interaction force during the scanning. Laser light used for this purpose is supplied via a monomode waveguide coupled to a 780 nm, 5 mW laser by *XYZ* precise single mode fibre coupler (Thorlabs). The laser is mounted in TEC with precisely controlled temperature by a TEC 2000 controller with the temperature stability of 1 mK. The laser power is controlled by a LDC 500 laser driver with 1 μW optical power resolution (Thorlabs). The light bundle from the waveguide end-face is focused by a lens system on the cantilever surface near the aperture. The position of light spot is regulated by an *XY* adjusting system which moves the fibre end with respect to the head body. The fibre is fixed inside a ceramic ferrule, cleaved and polished according to a standard procedure used during the FC/ST fibre connectors fabrication. The second laser light source (S1FC635 fibre coupled laser source) with 3-mW light power and λ = 635 nm, used for the aperture illumination, is coupled to the microscope head via another monomode fibre placed inside the same ferrule, parallel to the first one. The distance of the core centres of two fibres is 125 μm. The spot of 635 nm light is placed directly

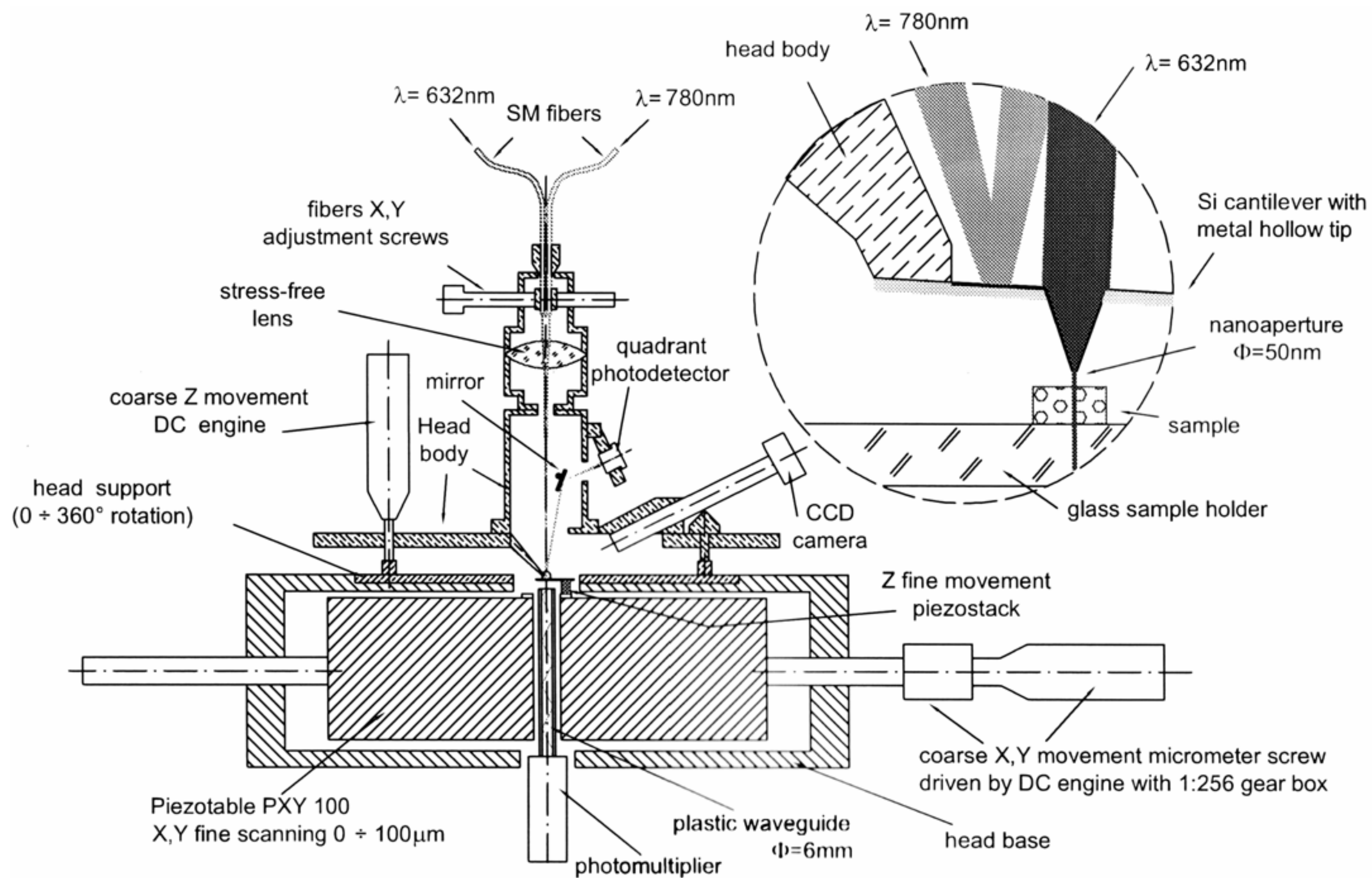

Fig. 7. SNOM/AFM microscope set-up

on the aperture entrance whereas the 780 nm light spot is placed nearby on the cantilever surface using the same lens and the *XY* ferrule adjusting system. The SNOM signal in the transmission mode is collected by a photomultiplier (Hamamatsu) placed under the head support. Light from the nanoaperture, after interacting with the sample surface, is coupled to one end face of 6 mm thick polycarbonate rod placed directly under the sample while the second end of the rod is coupled with the photomultiplier. The rod is passed through the head support via a PXY 100 table opening. The microscope head is connected to a scanning and acquisition electronic system controlled by a PC computer equipped with the ADDA measuring card (DAS 1702 ST-DA, Keithley) and an appropriate software (proximity control, scanning control + image processing) written in our laboratory under the C++ language.

4.2. Results

We performed test measurements using standard latex sphere samples for AFM and optical transmission contrast capability of our system. All experiments were taken in the constant height mode. In this way images are not topography-related. To illuminate the nanoaperture, we used circularly polarized light. The AFM mechanism was used for maintaining the sample-aperture distance on the level of several nanometres to keep the aperture in the proximity region [16].

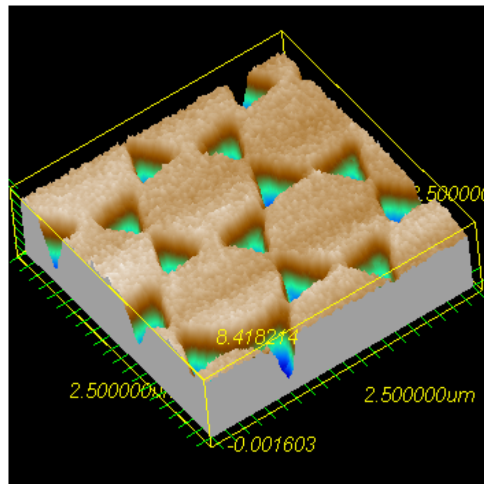

Fig. 8. 3D SNOM image of latex spheres shadows ($\phi = 1$ μm) (Al on mica)

The samples were prepared using aqueous suspension of polystyrene latex spheres [17]. We used triply distilled water with SDS (0.0025% sodium dodecyl sulfate) as a surfactant. In order to obtain a uniform layered structure of latex spheres, the surface of substrate should be hydrophilic (must be wetted by the solution). We used

a)

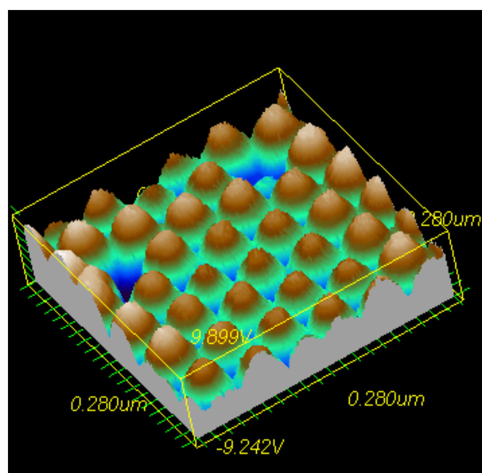

b)

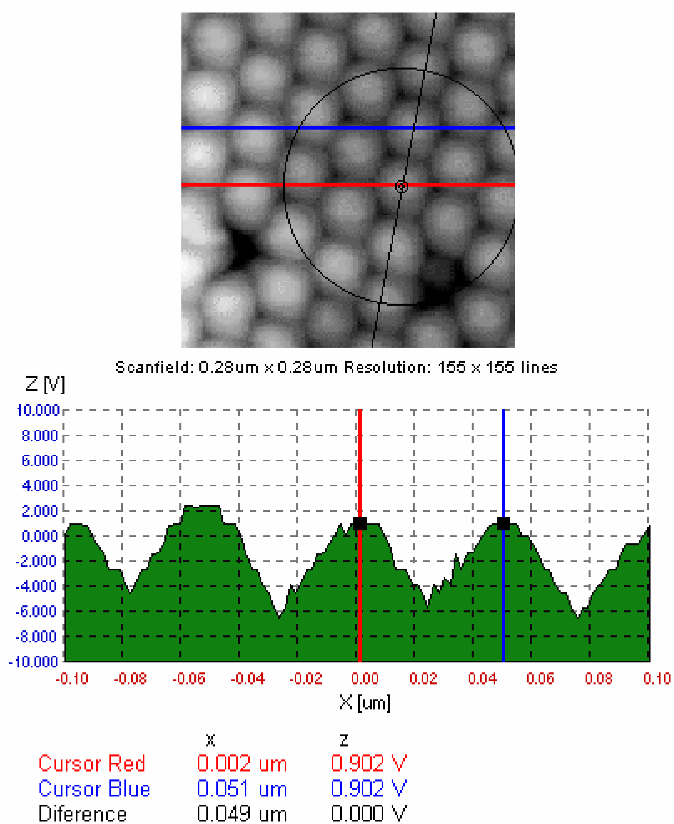

Fig. 9. 3D AFM image of latex spheres ($\phi = 50$ nm)
on mica (a) and measurement of sphere diameter (b)

a)

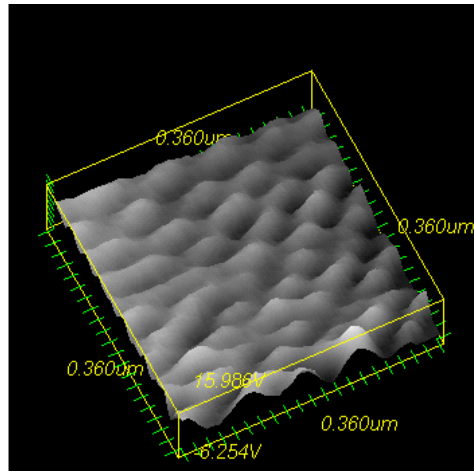

b)

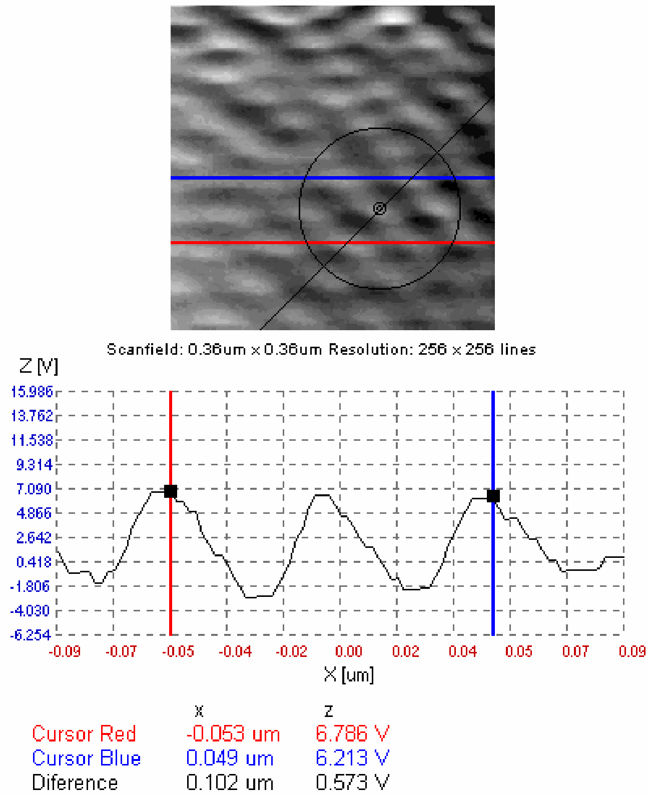

Fig 10. 3D SNOM image of latex spheres ($\phi = 50$ nm) on mica (a) and measurements of sphere diameter (b)

freshly cleaved mica on which the spread-out solution forms a thin film. Upon drying at ambient temperature, the solution evaporates from the surface, the capillary force pulls the spheres together and a film of spheres is formed. In Figure 8, we show a 3D image of the shadows of the latex spheres produced by the lift-off technique. 1 μm latex spheres on the mica surface were covered with an evaporated 20 nm Al layer. The spheres were then removed with methanol in an ultrasonic bath cleaner leaving Al triangular-shaped shadows on the mica substrate. Latex spheres form a hexagonal close-packed (HCP) lattice. It is clearly seen that the optical image contains details smaller than 100 nm. To prove that, we examined a sample containing 50 nm spheres in our system. In Figure 9a, we show a 3D AFM image of such a sample. There are a few defects – vacancies of spheres visible in the image. The sphere diameter measured from the image data (Fig. 9b) equals 49 nm. In Fig. 10a, we show a 3D SNOM image of the same sample (taken in a different place on the surface). The spheres can be distinguished in the image, with edge details lost due to size of the nanoaperture used in the experiment After subsequent diameter measurements, we found the distance between the centres of the spheres equal approximately to 51 nm. The experiments performed show the ability of our system to resolve objects of the size close to the nanoaperture diameter in the optical domain.

5. Conclusions

We presented an improved method of SNOM hollow tip fabrication with nanoapertures down to 50 nm drilled using FIB. The available FIB systems equipped with *xy*-stage and image recognition allow drilling 360 sensor Cr pyramids on a wafer for reasonably short time with an excellent reproducibility (size deviation and circularity). During the measurements, we found the normalized polarization ratios between 1:77 and 1:98. Thus, a significant improvement of optical properties of our SNOM cantilevers was achieved. The transmission coefficient of nanoapertures for cone angle 50° ranges from 10^{-3} for the aperture diameter of 100 nm to 5×10^{-7} for the aperture diameter of 10 nm. In our case, we obtained 50-nm aperture throughoutput ratio of 5×10^{-5} with the values lying within 30% with respect to the polarization direction. Very good optical parameters of the fabricated cantilevers with circular apertures make them very applicable for polarity-dependent experiments which will be performed in a near future.

Acknowledgements

The authors gratefully acknowledge discussion with I.W. Rangelow. They also thank K. Domański and M. Zaborowski for help with the cantilever technology, T. Schenkel for performing FIB ion drilling of nanoapertures, and T. Gotszalk for measurements of cantilever mechanical parameters and many useful discussions. The work was partially done within the Government Project No. 4T11B00224.

References

[1] SYNGE E.H., Phil. Mag., 6, 356 (1928).
[2] POHL D.W., DENK W., LANZ M., Appl. Phys. Lett., 44 (1984), 651.
[3] LEWIS A., ISAACSON M., HAROOTUNIAN A., MURAY A., Ultramicroscopy, 13 (1984), 227.
[4] BETZIG E., TRAUTMAN J.K., Science, 257 (1992), 189.
[5] VAN HULST N.F., SEGERINK F.B., European Microsc. Anal., Jan. 1992, 13.
[6] BETZIG E., FINN P., WEINER S., Appl. Phys. Lett., 60 (1992), 2484.
[7] GRABIEC P., GOTSZALK T., RADOJEWSKI J., EDINGER K., ABEDINOV N., RANGELOW I.W., Microelectronic Eng., 61/62 (2002), 981.
[8] BETZIG E., TRAUTMAN J.K., WEINER J.S., HARRIS T.D., WOLFE R., Appl. Opt., 31 (1992), 4563.
[9] VALASKOVIC G.A., HOLTON M., MORRISON G.H., J. Microsc., 179 (1995), 29.
[10] HUSER T., LACOSTE T., HEINZELMAN H., KITZEROW H.S., J. Chem. Phys., 108 (1998), 7876.
[11] ZHOU H., MIDHA A., BRUCHHAUS L., MILLS G., DONALDSON L., WEAVER J. M. R., J. Vac. Sci. Technol. B, 17 (1999), 1954.
[12] GOTSZALK T., GRABIEC P., RANGELOW I.W., Ultramicroscopy, 82 (2000), 39.
[13] MARTIN O.J.F., PAULUS M., J. Microscopy, 205 (2002), 147.
[14] LACOSTE T., HUSER T., PRIOLL R., HEINZELMAN H., Ultramicroscopy, 71 (1998), 333.
[15] HECHT B., SICK B., WILD U.P., DECKERT V., ZENOBI R., MARTIN O.J.F., POHL D.W., J. Chem. Phys., 112 (2000), 7761.
[16] POHL D.W., FISCHER U.CH., DUERIG U.T., SPIE, Vol. 897, *Scanning Microscopy Technologies and Applications*, 1988, 84.
[17] LI Y., LINDSAY M., Rev. Sci. Instr., 62 (1991), 2630.

Received 25 June 2003
Revised 22 August 2003

Materials Science, Vol. 21, No. 3, 2003

Application of electrostatic force microscopy in nanosystem diagnostics

TEODOR P. GOTSZALK[1*], PIOTR GRABIEC[2], IVO W. RANGELOW[3]

[1]Faculty of Microsystem Electronics and Photonics, Wrocław University of Technology, Wybrzeże Wyspiańskiego 27, 50-370 Wrocław, Poland

[2]Institute of Electron Technology, al. Lotników 32/46, 02-668 Warszawa, Poland

[3]Institute of Technological Physics, IMA, University of Kassel, Heinrich Plett Str. 40, 34132 Kassel, Germany

The current state of art of electrostatic force microscopy is described in the paper. The principle of electrostatic force operation enabling one to analyse local voltage distribution and capacitance is presented. The design and properties of electrostatic force microscopy microprobes are discussed. The application and manufacturing process of piezoresistive cantilevers with conductive tips and of silicon beams with metallic probe are presented. In order to show the capabilities of electrostatic force microscopy methods of investigations of local voltage distribution on surfaces of microelectronic integrated circuits (IC) are described. Improvements of electrostatic force microscopy and of other electrical methods based on scanning probe microscopy confirm an increasing interest in electrical probing at the nanometre scale.

Key words: *electrostatic force microscopy; nanosystem; voltage distribution; capacitance*

1. Introduction

A rapid progress in nanotechnology has been observed over the past twenty years. This progress has also been influenced by the development of new diagnostic methods aimed at testing fabricated nanodevices and materials. In nearly all these investigations, nanometre local resolution of the experiments performed and extremely high measurement sensitivity are needed, as high as those established in macroscale investigations. One of the best known techniques which enables surface measurements with the requirements defined above is the scanning probe microscopy. The development of this

[*]Corresponding author, e-mail: Teodor.Gotszalk@pwr.wroc.pl.

technique was stimulated by the invention of first scanning tunneling microscope (STM) by Binnig and Rohrer in 1981 [1]. Based on the design of STM, the first atomic force microscope (AFM) was developed in 1986 [2]. In this way, the era of structural analysis of surface properties using the scanning probe microscopy begun. Atomic force microscopy, in which force interactions acting on the microtip located upon a spring cantilever on the length scale from 10^{-11} to 10^{-7} are monitored, belongs to scanning probe microscopy methods. In 1988 Martin et al. [3] developed an atomic force microscopy based technique which enabled measurements of electrostatic forces and capacitances between the conductive tip and the surface with spatial resolution of 100 nm. This technique was also applied for potentiometry [4, 5] and detection of charges [6]. In 1991, Abraham et al. [7] demonstrated for the first time that dopant profiles in the range of concentrations between 10^{15} and 10^{20} cm^{-3} can also be measured in a nondestructive manner by means of an electrostatic force microscope with capacitive detection. However, the measurement possibilities are strongly dependent on the parameters of the micro- and nanoprobes applied and on the measurement setup. In this paper, we present a general principle of electrostatic force microscopy (EFM). We demonstrate the application of this technique in voltage measurement on the surface of a microelectronic integrated circuit. Additionally, we present electrostatic force microscopy nanoprobes with conductive microtips which were applied in our experiments. We also consider noise and sensitivity of the developed experimental methods.

2. The principle

In electrostatic force microscope (EFM), the electrostatic forces between the cantilever nanotip and the surface are measured. To maintain the distance over the investigated surface, the cantilever vibrates at its resonance frequency. Due to van der Waals forces, the beam vibration amplitude changes and the microscope controller defines the cantilever height over the sample using a piezoelectric actuator. Simultaneously, in order to measure electrostatic interactions in this setup (Fig. 1), we applied a voltage, consisting of an AC and a DC components: $U = U_{dc} + U_{ac}\sin(\omega t)$ between the tip and the sample which gives rise to an electrostatic force given by:

$$\begin{aligned} F &= \frac{1}{2}\frac{dC}{dz}(U_{dc} + U_{ac}\sin(\omega t))^2 \\ &= \frac{1}{2}\frac{dC}{dz}[(U_{dc}^2 + \frac{1}{2}U_{ac}^2) + 2U_{dc}U_{ac}\sin(\omega t) + \frac{1}{2}U_{ac}^2(1 - \sin(2\omega t))], \\ &= \frac{1}{2}\frac{dC}{dz}(F_{dc} + F_{\omega} + F_{2\omega}) \end{aligned} \tag{1}$$

where C is tip-sample capacitance and ω is the voltage frequency.

Fig. 1. Electrostatic force microscopy – a general principle

Fig. 2. Experimental setup of an electrostatic force microscope

In the force spectrum, three separate frequency components are observed: F_{dc}, F_{ω}, $F_{2\omega}$, which can be measured selectively using lock-in amplifiers. Note that in order to measure the DC potential on a specimen, a sum of auxiliary DC and AC voltages is applied to the conductive cantilever microtip (Fig. 2). The oscillation of the cantilever with the frequency ω should be balanced to zero by controlling the auxiliary DC voltage in a feedback loop. In this way, the DC voltage applied to the microtip corresponds to the voltage on a specimen.

3. Electrostatic force microscopy microprobes

In first electrostatic force microscopy experiments, metal wires fabricated by electromechanical etching were used. Relatively high radii of the cantilever tips and, additionally, large cantilever spring constants and their low resonance frequencies did not make them suitable for routine applications. In later experiments, commercially available highly doped silicon cantilevers were applied in investigations of electrical surface parameters. However, the spatial resolution of 50 nm in surface investigations and the high mechanical wear were not sufficient in many applications. In our experiments, two kinds of electrostatic force microscopy sensors have been employed: piezoresistive silicon cantilevers and silicon cantilevers with metalic tips. Most of EFM systems require optical techniques to detect a subnanometre motion of the microtip. From the demand for simplifying the EFM head, an idea came to build the cantilever with an integrated deflection detector and the conductive microtip isolated from the cantilever body. The microprobe, fabricated in the silicon on insulator (SOI) technology, integrates the piezoresistive bridge deflection sensor whose resistivity changes when the cantilever is bent [8]. In this way, an electrical signal corresponding to the beam deflection is measured and can be fed into a standard microscope control unit.

The device developed is shown in Fig. 3. The dimensions of the sensor are: the length 600 μm, width 210 μm, thickness 15 μm, which corresponds to the spring constant of 113 N/m and the beam resonance frequency of 50 kHz. The voltage measurement sensitivity is limited by the relative high spring constant amounting 50 mV for the design described.

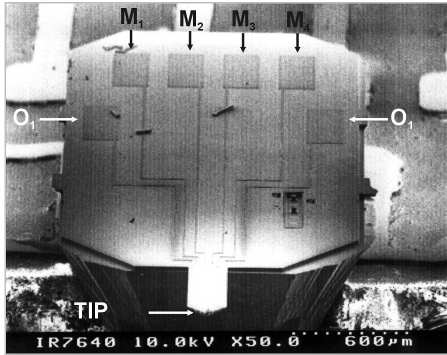

Fig. 3. Piezoresistive cantilever with conductive tip for electrostatic force microscopy. M_1–M_4 are metalization pads for piezoresistive sensor, O_1 – connections strips to the conductive tip

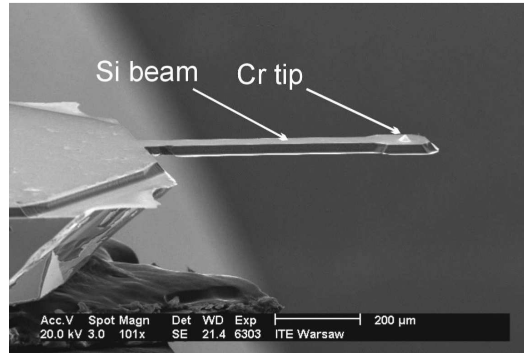

Fig. 4. Microfabricated cantilever with metallic tip for the electrostatic and capacitance microscopy [9]

To perform more sensitive experiments, we developed a cantilever with a metallic tip [9]. The sensor was fabricated in the complementary metal oxide semiconductor (CMOS) technology combined with the surface and bulk micromachining. The microprobe consists of a pyramid-shaped Cr tip and a metal line deposited on a silicon beam (Fig. 4). The narrow metal strip located on the cantilever backside is used for the electrical connection between the microtip and the microscope electronics. The metal cantilever tip makes the sensor suitable in semiconductor investigations like dopant profiling based on capacitance–voltage (*C*–*V*) and electrostatic force measurements. The beam deflection occuring when the cantilever is bent under van der Waals and electrostatic interactions is observed using an optical position sensitive detector with the resolution of 0.05 nm in the band width of 100 Hz.

4. Experimental

The sensitivity of the electrostatic interactions measurement using the piezoresistive cantilever was tested. The Wheatstone piezoresistive bridge cantilever was placed 100 nm above the surface (the distance was controlled by a fibre interferometer) and the beam resonance curves were recorded for the tip-surface voltages of $U = 0$ V and $U =$ 10 V. The electrostatic attractive interaction acts as an additional spring shifting the

beam resonance frequency to lower values. The resonance frequency shift for the parallel tip–surface capacitor is given by the equation:

$$\Delta f = f_r \frac{\varepsilon_0 A U^2}{2kz^3} \tag{2}$$

For the beam with the geometry of l = 600 µm, b = 210 µm, d = 15 µm, spring constant k = 113 N/m, resonance frequency f_r = 50 kHz, cross-sectional area A = 0.1 µm^2, the resonance frequency shift Δf can be estimated to amount to 15 Hz. In Figure 5, the resonance curves measured for the tip-surface voltage of 0 V and 10 V are shown. The resonance frequency shift of 20 Hz was detected under the voltage difference of 10 V.

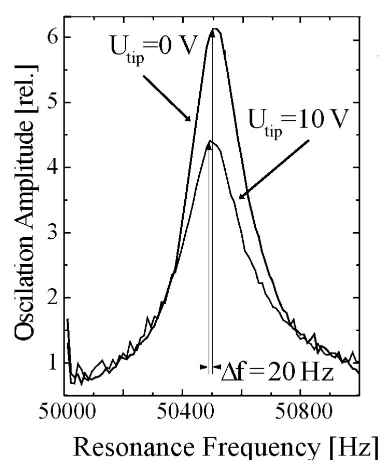

Fig. 5. Resonance frequencies of the piezoresistive cantilever with a conductive tip under various probe voltages [8]

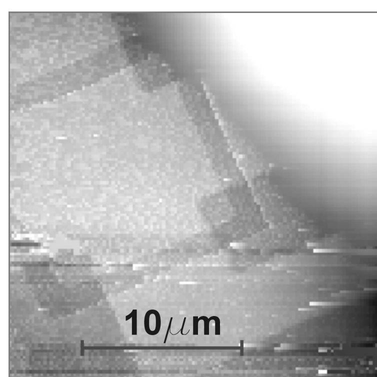

Fig. 6. Topography of the MEMS piezoresistive force detector measured with the fabricated microprobe

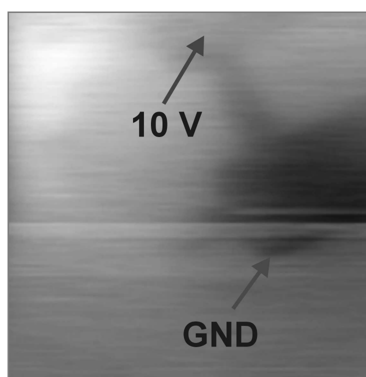

Fig. 7. Electrostatic force microscopy map of the voltages in the area shown in Fig. 6

To present the possibilities of the voltage measurement, we applied the cantilever with a metalic tip in the test measurement of the dc potential on an IC surface. The sample contains four implanted resistors which are connected to form a Wheatstone bridge (Fig. 6). The sample topography was measured based on the resonance vibration reduction under the influence of the van der Waals force interaction. While scanning the surface we also observed the electrostatic force F_ω, when only one bridge resistor was supplied with the voltage of 10 V. The voltage drop along the implemented resistor is clearly seen in Fig. 7.

5. Conclusions

The electrostatic force microscopy based on the scanning probe microscopy methodology, is an established technique for local investigations on insulating and conductive nanosystems. Using this technique, one can study not only the topography but also obtain information about: (i) local work function on the surface (so-called Scanning Kelvin Microscopy), (ii) capacitance between the microtip and the surface, related to the dielectric surface parameters or dopant profiles, (iii) voltage behaviour on an operating structure. The features presented make electrostatic force microscopy important as a tool in nanotechnology and failure analysis. An improvement in spatial resolution is connected with the fabrication and application of cantilevers with spring constants inferior to 5 N/m, upon which tips with the radius of 15 nm are located. The increased measurement sensitivity can be achieved by applying electrical modulation voltage to the tip whose frequency corresponds to a higher eigenmode resonance beam oscillation.

Acknowledgements

The authors would like to thank our colleagues: Dr. A. Sankowska, Dr. J. Radojewski, A. Sikora, A. Marendziak and P. Janus for many useful discussions and comments. This work was sponsored by the Centre of Advanced Materials and Nanotechnology (CMZiN) of the Wrocław University of Technology.

References

[1] BINNIG G., ROHRER H., Helv. Phys. Acta, 55 (1982), 726.
[2] BINNIG G., QUATE C.F.. GERBER CH., Phys. Rev. Lett., 56 (1986), 930.
[3] MARTIN Y., ABRAHAM D.W., WICKRASINGHE H.K., Appl. Phys. Lett., 52 (1988), 1103.
[4] WEAVER J.M.R., ABRAHAM D.W., J. Vac. Sci. Technol. B9 (1991), 1559.
[5] MUELLER F., MUELLER A.D., HIETSCHOLD M., KAEMMER S., Meas. Sci. Technol., 9 (1998), 734.
[6] WATANABE S., HANE K., OHYE T., ITO M., GOTO T., J. Vac. Sci. Technol. B11 (1993), 1774.
[7] ABRAHAM D., WILIAMS C., SLINKMAN J., WICKRAMASINGHE H.K., J. Vac. Sci. Technol. B9 (1991).
[8] GOTSZALK T., DUMANIA P., RADOJEWSKI J., HUDEK P., SHI F., RANGELOW I.W., J. Vac. Sci. Technol. B16 (1998), 3948.

[9] GOTSZALK T., CZARNECKI P., GRABIEC P., DOMAŃSKI K., ZABOROWSKI M., RANGELOW I., paper presented at EIPBN 2003 Conference in Tampa (FL), to be published in J. Vac. Sci. Technol.

Received 1 July 2003
Revised 24 August 2003

Materials Science, Vol. 21, No. 3, 2003

Thermal characterization of copper thin films made by means of sputtering

ROMAN F. SZELOCH*, WITOLD M. POSADOWSKI,
TEODOR P. GOTSZALK, PAWEŁ JANUS, TOMASZ KOWALIW

Faculty of Microsystem Electronics and Photonics, Wrocław University of Technology,
Wybrzeże Wyspiańskiego 27, 50-370 Wrocław, Poland

Copper thin films have been deposited onto Corning glass substrates by means of two kinds of DC magnetron sputtering. The goal of this research was to study differences in thermal characteristics of both kinds of the films. The differences between these layers originate from the technological processes; one of them employs an inert gas – argon – in the vacuum chamber, and the other is the so-called "pure" self-sputtering. Thermal characterization of the layers was performed using the scanning thermal microscopy (SThM) as well as a far field thermographical system.

Key words: *copper, magnetron; sputtering; scanning thermal microscopy*

1. Introduction

Copper metallization of on-chip multilevel interconnects became in last decade an industrial process for new generations of integrated circuits (IC). Copper, compared to aluminium, has a greater resistance to electromigration and a lower electrical resistivity resulting in improved electrical performance, reduced Joule heating and better heat transport. On the other hand, thermal properties of the copper thin films depend on impurities introduced in the process of fabrication [1–4]. This paper presents the results of thermal characterization of copper layers, focusing on the influence of argon impurities. A comparison will be made between Cu thin films obtained by a standard magnetron sputtering (under argon atmosphere) and a self-sustained magnetron sputtering (without any working gas).

---

*Corresponding author, e-mail: rszel@wemif.pwr.wroc.pl.

2. Magnetron sputtering

In the case of films obtained by the standard sputtering process, the argon gas, albeit indispensable in the process (argon mode), may be treated as undesirable impurity. It becomes a factor that essentially modifies the structure (the Thornton's zone model) and electrical parameters of the films deposited. The application of the self-sustained magnetron sputtering (SSS) allows depositing thin films without noble gas contamination, with a very high deposition efficiency [5]. In this mode of sputtering, the discharge is sustained by sputtered metal ions and the working pressure in the chamber is equal to the final pressure of vacuum set. The properties of films deposited in such a way may differ from those prepared under argon. The purity of self-sputtered Cu films depends on the purity of the target material and of rest gases only (argon pressure is equal to zero in Thornton's structure diagram). The absence of any working gas in the sputtering process means, on one hand, elimination of potential impurities in the film being deposited and, on the other hand, deposition of films under new „microgeometry" conditions of the target-to-substrate particle transport (no collision events with the working gas). To deposit Cu films in the self-sustained sputtering mode a very high target power density is necessary (even a few hundreds W/cm^2). Using the WMK-100 magnetron device, about 100 W/cm^2 is necessary to sustain the sputtering without argon presence (SSS) [6, 7].

3. Thermal characterisation

Our thermal characterization of both types of copper thin films employs two methods. One of them is the classical far field thermography [8–10]. An IR far field microscope was applied to determine the IR radiation from the Cu metallization at various sample temperatures. Using the calibration curve, the signals of the IR radiation emitted from the sample surface were processed into emissivity factors. Figure 1 shows the influence of argon impurities on the emissivity factor. In the case of 1 μm film this factor is grater than that in the case of 2 μm film.

Another kind of our experiments was performed using the scanning thermal microscope for measurements of thermal conductivity (diffusivity) of samples with high spatial resolution.

The invention of the scanning tunneling microscope (STM) [11] and the atomic force microscope (AFM) [12] allowed sub-micrometer and, at times, atomic scale spatially resolved imaging of surfaces. The spatial resolution of nearfield techniques (such as AFM) is only limited by the active area of the sensor (which in the case of STM may only be a few atoms at the end of a metal wire). First experiments in scanning thermal microscopy (SThM) were carried out by Williams and Wickramasinghe [13] who employed a heated thin-film thermocouple fabricated of a conventional STM tip. In 1994,

Dinwiddie and Pylkki described first combined SThM/AFM probes which employed resistance thermometry to measure thermal properties [14, 15].

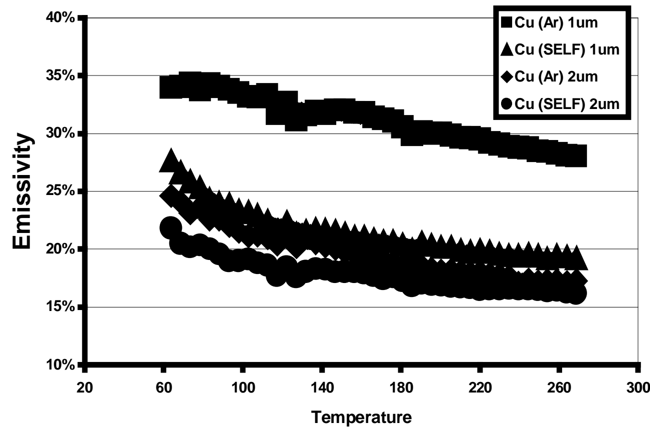

Fig. 1. Emissivity factor of the Cu samples versus temperature

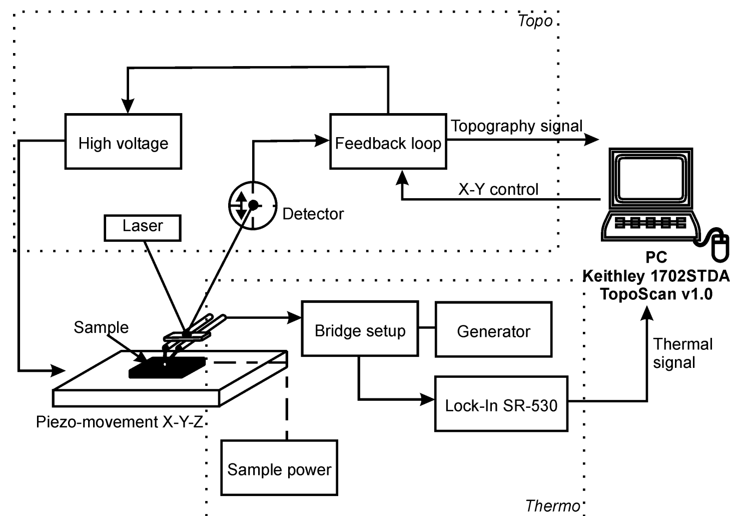

Fig. 2. Wollastone probe and block diagram of SThM system

The thermometers were fashioned and made of the Wollastone process wire, consisting of a thin platinum core (ca. 5 μm in diameter) surrounded by a thick silver sheath (ca. 75 μm). A loop of wire is formed and silver is etched away to reveal a small section of platinum which acts as a miniature resistance thermometer (Fig. 2a). Because of its high endurance, the Wollastone probe is attractive for micro- and nano-materials and microsystems diagnostic. The probe is capable of performing three functions: exerting a force on the sample surface (AFM), acting as a highly localized heat source (either constant or modulated), and measuring heat flow.

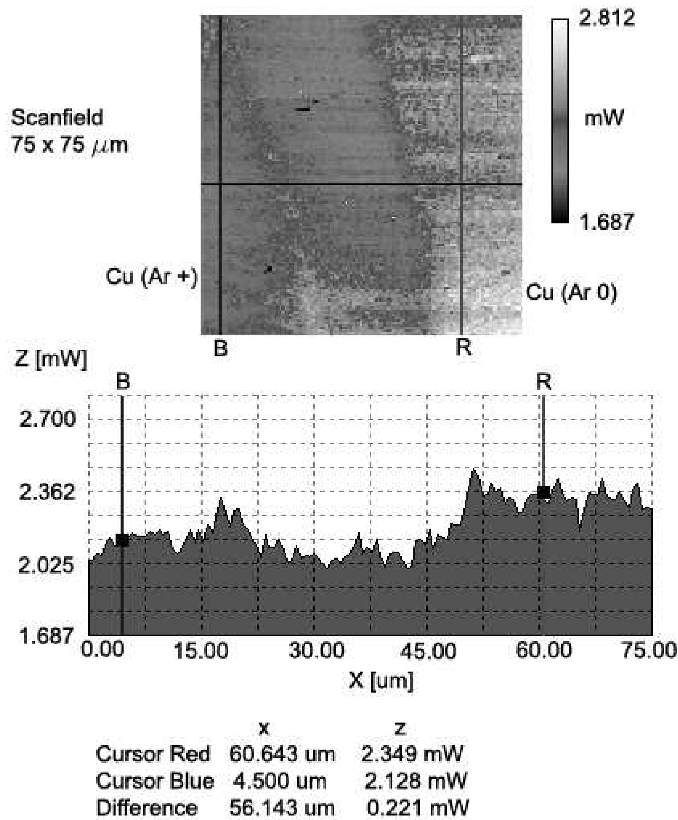

Fig. 3. Distribution of thermal conductance on Cu 0.5 μm films. Influences of Ar impurities in the layers are linked with difference of the signals on left (cursor blue B) and right (cursor red R) sites of the figure

The block diagram of our SThM apparatus is shown in Fig. 2b. The system can operate in two modes; as a passive thermosensing element (by measuring its temperature using a small current c.a. 500 μA) or as an active heat flux meter. In the latter case, a larger current (sufficient to raise the temperature of the probe above that of the surface – over 30 mA) is passed through the probe. The power required to maintain a constant temperature gradient between the tip and sample is monitored by means of an electrical bridge circuit. This power is related to the local thermal conductivity (diffusivity) of the sample [16, 17]. The SThM system allows us to measure local temperature with the thermal resolution 5 mK and thermal conductivity with the resolution of 10^{-2} W/mK. Dedicated software modules TopoScan and TopoGraf are used for measurement control and data processing [16].

The active mode of SThM is a promising method for thermal investigations of metals as well as of wide gap materials (i.e. GaN). A correlation between low threading

dislocation density and high thermal conductivities was established [13]. We applied the SThM apparatus in active mode to measure local thermal conductivity of copper samples. Although the calibration procedure was not developed for copper samples in our system, it was nevertheless possible to use our microscope for the evaluation of local differences in values of thermal conductivity as well as of the geometrical topography of the sample as is shown in Fig. 3.

4. Conclusion

We applied our Scanning Thermal Microscope in active mode for the diagnostic of copper thin films. The measurements have been performed on two kinds of the Cu layers made by two kinds of magnetron sputtering. The topography and local diffusivity distribution shows the influence of argon impurities in the body of the Cu films. Thermal diffusivity can be determined with sub-micron spatial resolution.

Acknowledgements

The authors acknowledge the support from the Polish Committee for Scientific Research (KBN), grant No. 4 T11B 00224.

References

[1] VINCI R.P., ZIELINSKI E.M., BRAVMAN I.C., Thin Solid Films, 262 (1995), 142.
[2] GUTMAN R.J., CHOW T.P., KOLOYEROS A.E., LANFORD W.A., MURAKA S.P., Thin Solid Films, 262 (1995), 177.
[3] MCCUSTER N.D., GAMBLE H.S., ARMSTRONG B.M., Microelectronics Reliability, 40 (200), 69.
[4] WEISS A., GRÖGER V., KHATIBI G., KOTAS A., ZIMPRICH P., STICLER R., ZAGAR B., Sensors and Actuators A 99 (2002), 172.
[5] POSADOWSKI W.M., Vacuum, 46 (1995), 1017.
[6] POSADOWSKI W.M., Vacuum, 53 (1999), 11.
[7] POSADOWSKI W.M., Thin Solid Films 392 (2001), 201.
[8] SZELOCH R.F., GOTSZALK T.P., GUMIENNY Z., Proc. of the Seminar Thermic '98, Zakopane (1998), p. 45.
[9] SZELOCH R.F., GOTSZALK T.P., RADOJEWSKI J., JANUS P., ORAWSKI W., PĘDRAK R., Proc. of Micro-Mat 2000, Berlin (2000), p. 1257.
[10] SZELOCH R.F., GUMIENNY Z., SOŁTYSIAK R., REGEŃCZUK R., Proc. of ISHM Conf., Warsaw, Poland (1990), p. 78.
[11] BINNIG G., ROHRER H., Helv. Phys. Acta., 55 (1982), 726.
[12] BINNIG G., QUATE C.F., GERBER CH., Phys. Rev. Lett. 56, (1986), 930.
[13] WILLIAMS C.C., WICKRAMASINGHE H.K., Appl. Phys. Lett., 49 (1986), 1587.
[14] DINWIDDIE R.B., PYLKKI R.J., WEST P.E., Thermal Conductivity 22 (1994), 668.
[15] PYLKKI R.J., MOYER P.J., WEST P.E., Jpn. J. Appl. Phys., 33 (1994), 3785.
[16] SZELOCH R.F., GOTSZALK T.P., JANUS P., Microelectronics Reliability, 42 (2002), 1719.
[17] www.thermomicro.com *Scanning Thermal Microscopy (SThM) and its Application in Thermal Characterization of Semiconductor and Advanced Material Surfaces*.

Received 28 June 2003
Revised 20 August 2003

Materials Science, *Vol. 21*, *No. 3*, *2003*

Wavelet shrinkage-based noise reduction from the high resolution X-ray images of epitaxial layers

JANUSZ KOZŁOWSKI[1*], JAROSŁAW SERAFIŃCZUK[1], ANDRZEJ KOZIK[2]

[1]Faculty of Microsystem Electronics and Photonics, Wrocław University of Technology,
Wybrzeże Wyspiańskiego 27, 50-370 Wrocław, Poland

[2]Institute of Engineering Cybernetics, Wrocław University of Technology,
Wybrzeże Wyspiańskiego 27, 50-370 Wrocław, Poland

This paper presents advantages of employing the wavelet method in X-ray high-resolution image analysis of nanostructures. It is shown that many more details of the structure examined can be distinguished in rocking curves (RC) as well as in reciprocal space maps (RSM) after application of the numerical procedure. The method proposed seems to be particularly suitable for imperfect epitaxial layers having significant lattice mismatch with respect to substrate. By means of the wavelet analysis of the X-ray images using de-noising procedure details invisible in raw pictures can be detected such as thickness fringes, gradient of lattice parameters etc., and duration of measurements can be shortened.

Key words: *wavelet, X-ray; epitaxial layer*

1. Introduction

The wavelet method has been widely applied in several signal analyses, e.g. human speech, seismic tremors, engine vibrations, and medical images. All types of signals have to be efficiently encoded, described and modelled. For the first time, the method is applied to X-ray high-resolution image analysis of optoelectronic structures. It seems to be very promising in the case of noised X-ray diffractometric images that are typical of the epitaxial layers having a large lattice mismatch with respect to substrate. In these cases, a diffuse scattering appears, obscuring the readability of the X-ray image.

[*]Corresponding author, e-mail: janusz.kozlowski@ pwr.wroc.pl.

2. Brief introduction to wavelets

Wavelets are a family of basis functions that can be used to approximate other functions by expansion in orthonormal series. They combine such powerful properties as orthonormality, compact support, varying degrees of smoothness, localization both in time and scale (frequency), and fast implementation. One of the key advantages of wavelets is their ability to spatially adapt to features of a function such as discontinuities and varying frequency behaviour. In statistics, the interest in wavelets arose after Daubechies [1] and Mallat [2] connected the wavelets with discrete data processing, and when Donoho and Johnstone [3] showed that wavelet shrinkage has desirable statistical optimality properties in problems connected with reduction of noise. We present here a brief overview to the orthogonal discrete wavelet transformation (DWT) and wavelet shrinkage techniques. For detailed review of the subject we direct the reader to Daubechies [4] and Nason [5].

2.1. Discrete wavelet transformation

Let the function $f(x)$ be sampled at N equally spaced points. In addition, let $f = (f(1), f(2), \ldots, f(N)) = (f_1, \ldots, f_N)$ be an element of the Hilbert space $\ell_2(N)$ of all square sum able sequences of the length N.

Let us define **H** and **G** operators $\ell_2(2M) \to \ell_2(M)$ coordinate-wise via

$$a \notin \ell_2(2M) \quad (Ha)_k = \sum_m h_{m-2k} a_m$$
$$(Ga)_k = \sum_m g_{m-2k} a_m$$

These operators correspond to lowpass (**H**) and highpass (**G**) filtering (convolution) followed by downsampling (throwing away every other sample). The inverse process (signal reconstruction) is possible, since for quadrature mirror filters $\{h_k\}$ and $\{g_k\}$ the perfect reconstruction conditions are satisfied:

$$\mathbf{H}\mathbf{G}^* = \mathbf{G}\mathbf{H}^* = 0, \qquad \mathbf{H}^*\mathbf{H} + \mathbf{G}^*\mathbf{G} = \mathbf{I}$$

where $\mathbf{H}^*$ and $\mathbf{G}^*$ are adjoin operators to **H** and **G**, and **I** is an identity operator on $\ell_2(N)$. The elementary wavelet decomposition/reconstruction step (shown in Fig. 1) results in cA (approximation coefficients) and cD (detail coefficients) sequences corresponding to a low and high frequency content of signal, respectively.

Since the decomposition step can be iterated many times (say, J), the discrete wavelet transformation (DWT) of f is an $\ell_2(N)$ sequence

$$\beta = \left(Gf, GHf, \ldots, GH^{J-1}f, H^J f\right) = \left(cD_1, cD_2, \ldots, cD_J, cA_J\right)$$

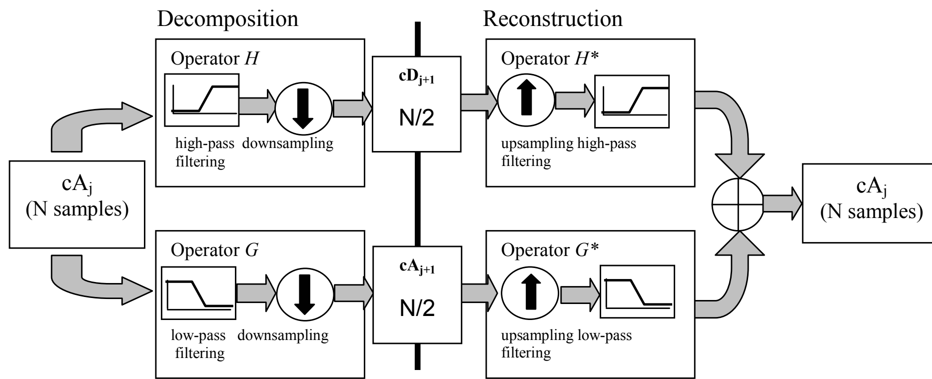

Fig. 1. Wavelet decomposition/reconstruction step

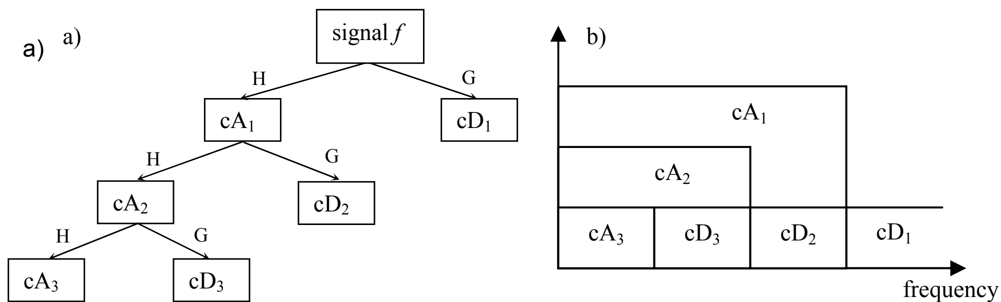

Fig. 2. Decomposition tree (DWT at level 3) (a) and frequency contents of coefficients (b)

The multi-level decomposition process (referred to as decomposition tree) is shown in Fig. 2a. Figure 2b shows the frequency content of the wavelet coefficients at different decomposition levels.

2.2. Wavelet shrinkage

The wavelet shrinkage methods achieve asymptotically near optimal minimax mean-square error for a wide range of signals corrupted by an additive white Gaussian noise. The methods derive from the basic idea that the energy of a signal (with some smoothness) will often be concentrated in a few coefficients in wavelet domain while the energy of noise is spread among all coefficients in wavelet domain. Therefore, the nonlinear shrinkage function in wavelet domain will tend to keep a few larger coefficients representing the signal while the noise coefficients will tend to reduce to zero.

The wavelet shrinkage can be described as three-step procedure:

1. A noisy signal is transformed to the wavelet domain by DWT.
2. The coefficients representing details (cD_1, ..., cD_J) are shrunk.
3. The shrunk wavelet coefficients are returned to the time domain by the inverse DWT. The result is a wavelet shrinkage estimator of the denoised signal.

Donoho et al. [3] showed that in estimating denoised signals simple shrinkage rules have asymptotic optimality properties for a rich class of function spaces. Examples are hard and soft thresholding rules, given by

$$\delta^{\text{hard}}(x,\lambda) = x \cdot 1(|x| > \lambda) \tag{1}$$

$$\delta^{\text{soft}}(x,\lambda) = (x - \text{sign }(x)\lambda) \cdot 1(|x| > \lambda) \tag{2}$$

where λ is a threshold parameter and $1(\cdot)$ is an indicator function.

For a fixed shrinkage policy, the parameters of shrinkage (eg. threshold λ) can be selected in many ways. The method of selecting threshold λ in soft thresholding rule (2) proposed by Donoho et al. [3] has a form:

$$\lambda = \frac{\hat{\delta}}{\sqrt{n}} \sqrt{2\log n} \tag{3}$$

where $\hat{\delta}$ is the estimator of standard deviation of details coefficients, and n is the number of details coefficients.

2.3. Wavelet shrinkage basing approach to denoising X-ray images

In our approach to noise suppression in X-ray high-resolution images we use the wavelet decomposition described in section 2.1. The decomposition level J is dependent on the number of samples in the denoised signal (N); we apply $J = 3$ for $N \approx 600$ and $J = 5$ for $N \approx 2000$. The chosen family of wavelet basis functions (determining the quadrature mirror filters) is dependent on the appearance of noisy signal, e.g. smoothness, discontinuities. We make use of Daubechies, Coifmann and Symlet wavelets families. A detailed information about families of filters can be found in [6].

The noise suppression is based on hard-thresholding rule (1). Since the method (3) of selecting the shrinkage threshold λ tends to underfit the signal (the threshold λ is too high and it shrinks too many details coefficients), we empirically found a rule for setting the threshold, which is a modification of (3):

$$\lambda = \frac{\hat{\delta}}{n} \sqrt{2\log n} \tag{4}$$

3. Experimental

Two kinds of samples were investigated:

- AlN buffer layers deposited on sapphire substrates in manufacturing high quality nitride semiconductors (e.g. GaN, (Al,Ga)N, (In,Ga)N) (the lattice mismatch in AlN/sapphire structures is about 16%). The AlN layers were deposited by the two-step pressure MOCVD process [7].

• Quantum wells (QW) based on $In_xGa_{1-x}As/GaAs$ structures deposited by the MOVPE process (lattice mismatch in such structures quickly increases with indium content and reaches 15% for InAs/GaAs structure).

A high resolution Philips diffractometer, equipped with four Ge crystal bounce Bartels monochromator in the incident beam optics and two Ge crystal bounce analyzers (RSM measurement) or receiving slit (RC measurement) in the diffracted beam optics was used for data collecting. $Cu_{K\alpha 1}$ radiation was applied. Rocking curves as well as reciprocal space maps were analyzed.

4. Results

AlN buffer layer deposited on the sapphire substrate was examined as a first example. Figure 3 shows the SEM picture of the layer cross-section parallel to the [0001] direction. The thickness observed of the AlN buffer is about 600 nm.

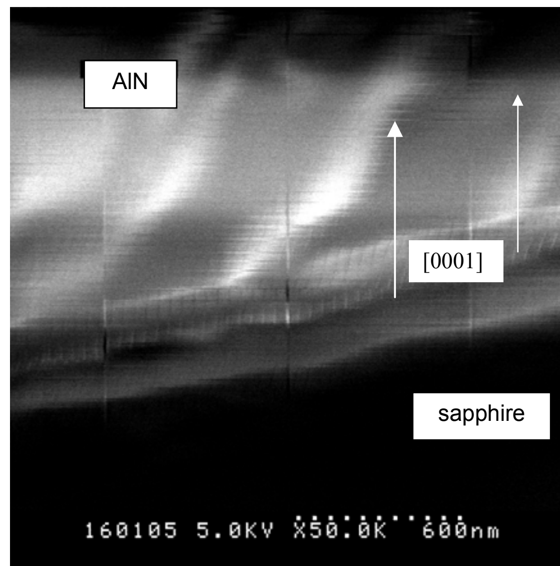

Fig. 3. SEM image of AlN buffer layer recorded perpendicular to the [0001] axis

For the same structure, the (00.2) reciprocal space map was measured. Before applying the wavelet shrinkage, a very noisy image is visible (Fig. 4a). It is obtained in a relatively short period of time (0.2 sec/step). Thanks to the wavelet analysis it was possible to extract an additional information about the examined structure from the measured map. Figure 4b shows the same map after the wavelet analysis. We can find here the thickness fringes as well as the gradient of the parameter c which is connected with a streak along 2theta/omega axis. The thickness of the layer, calculated from Eq. (5) [8], is equal to 608 nm ($\Delta\theta = 0.0075°$).

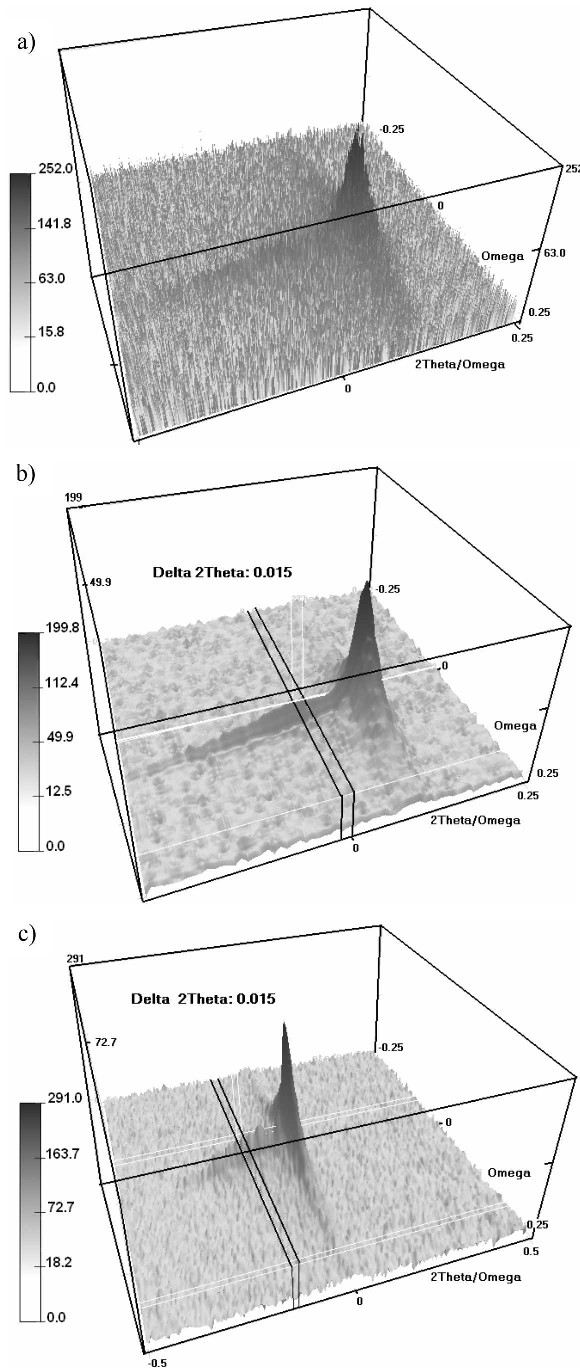

Fig. 4. (00.2) reciprocal space maps of AlN buffer layer deposited on sapphire substrate: a) measured in short time per step – 0.2 sec; b) map (a) after wavelet analysis (Daubechies wavelet (level 3)); c) measured in long time per step – 2.85 sec

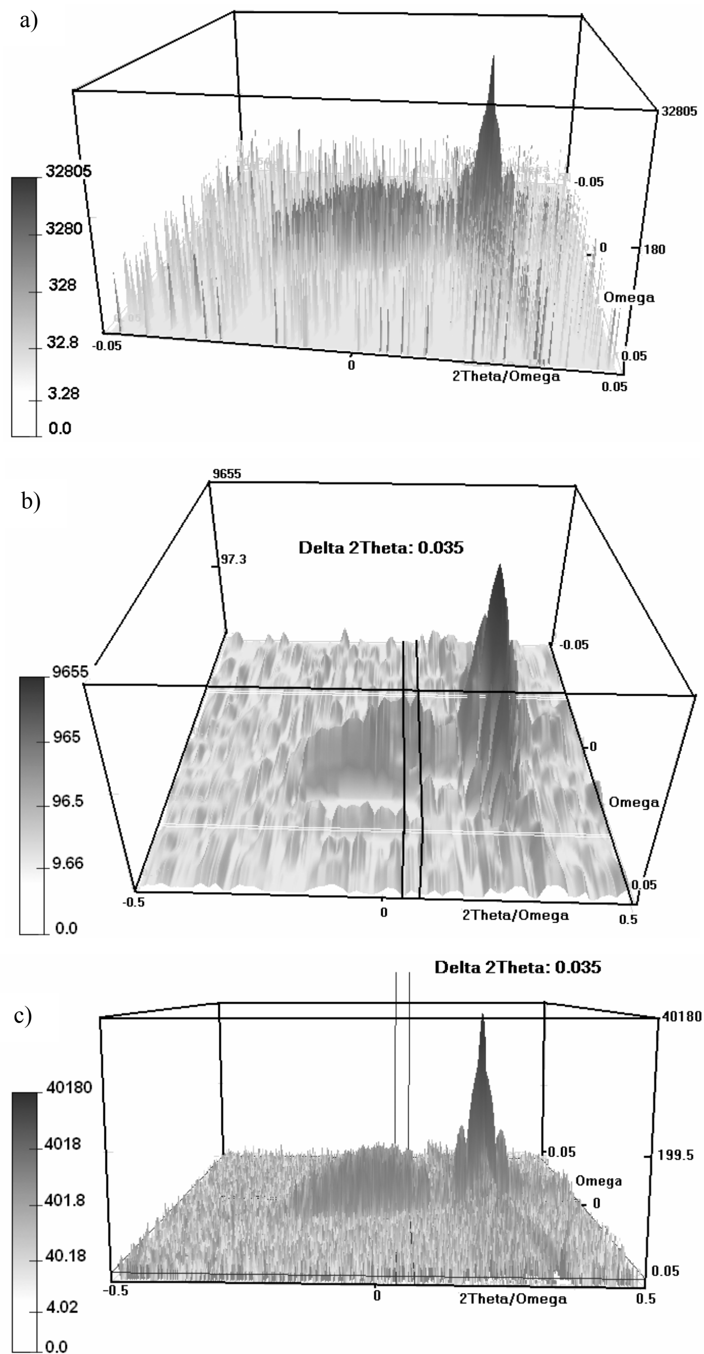

Fig. 5. (004) reciprocal space maps of quantum well GaAs/In_xGa_{1-x} As/GaAs: a) measured in short time per step – 0.05 sec; b) after wavelet analysis Symlet wavelet (level 3); c) measured in long time per step – 1.05 sec

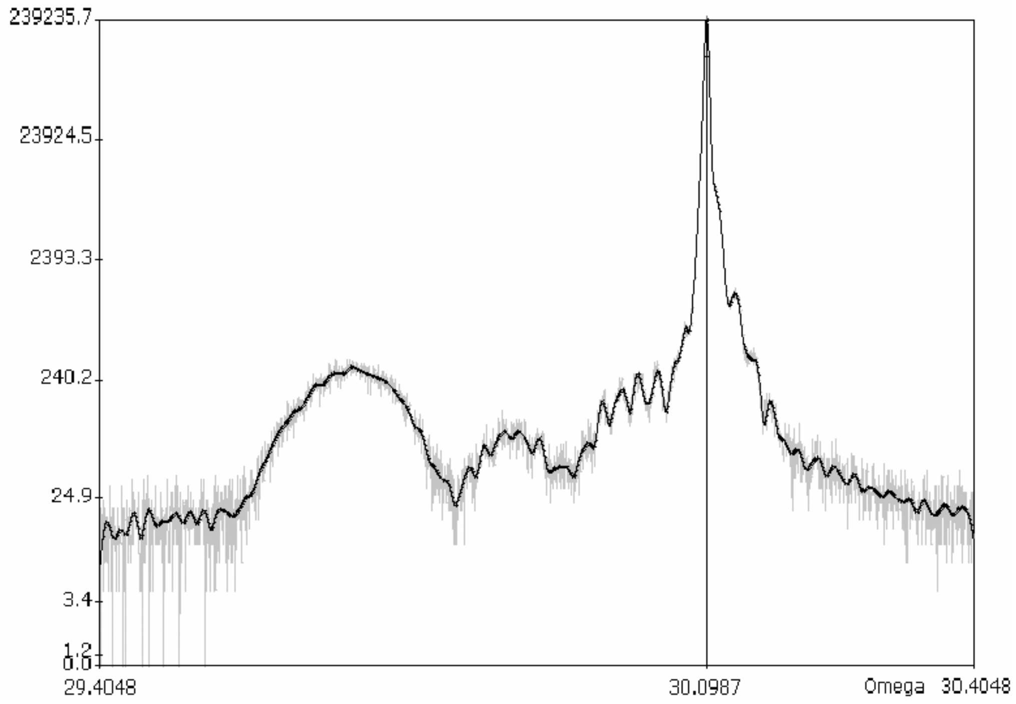

Fig. 6. Rocking curves of quantum well of GaAs/In_xGa_{1-x}As/GaAs (x = 0.083) measured (grey line) and after wavelet analysis (black line)

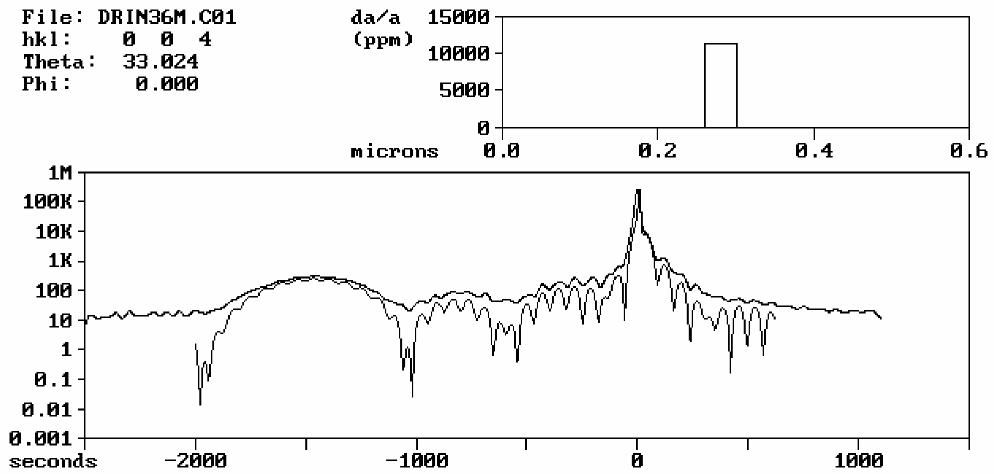

Fig. 7. Rocking curves of quantum well GaAs/In_xGa_{1-x}As/GaAs (x = 0.083) calculated (lower line) and after wavelet analysis (upper line)

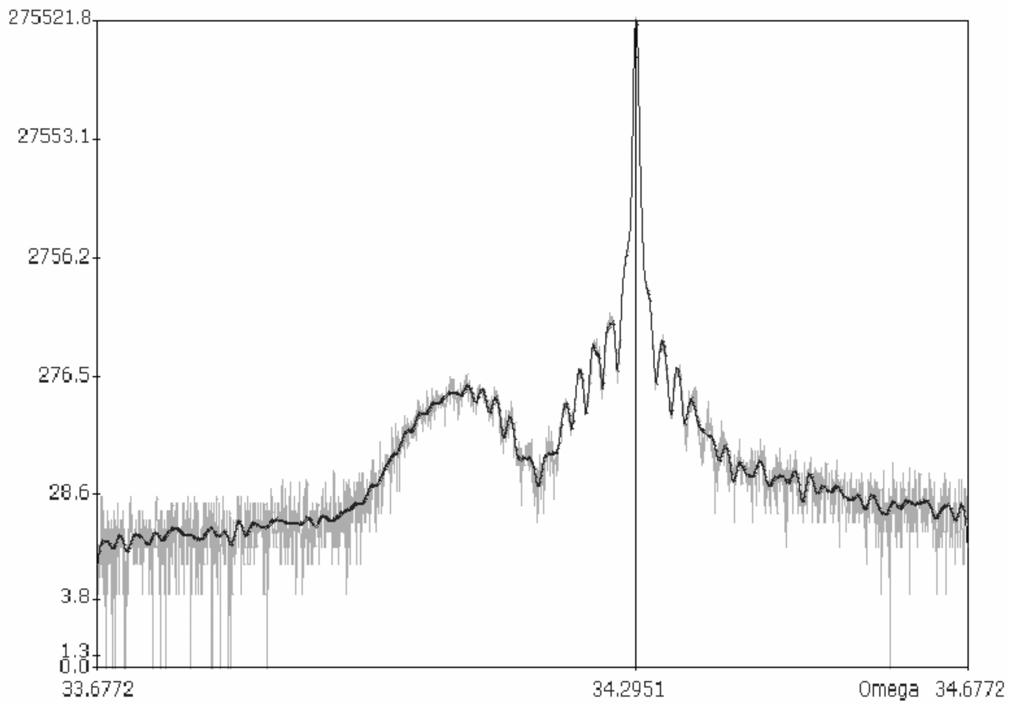

Fig. 8. Rocking curves of quantum well of GaAs/In_xGa_{1-x}As/GaAs (x = 0.0445) measured (grey line) and after wavelet analysis (black line)

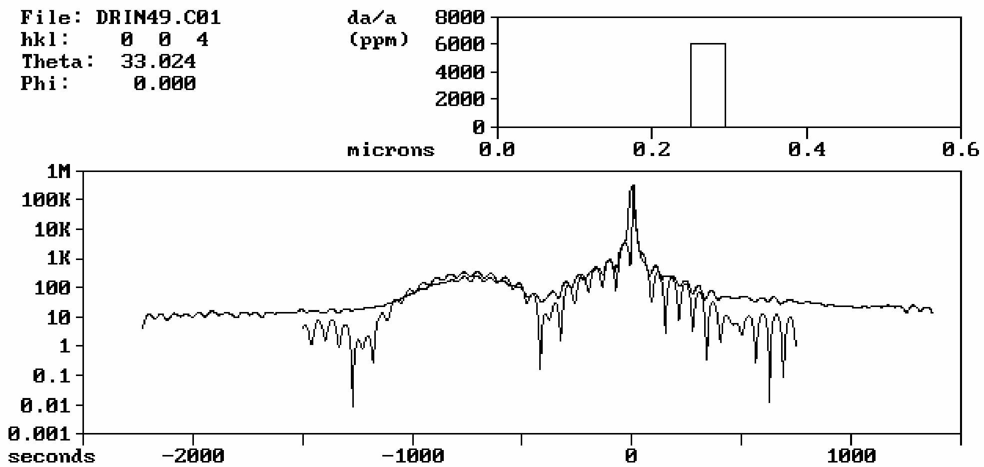

Fig. 9. Rocking curves of quantum well of GaAs/In_xGa_{1-x}As/GaAs (x = 0.0445) calculated (lower line) and after wavelet analysis (upper line)

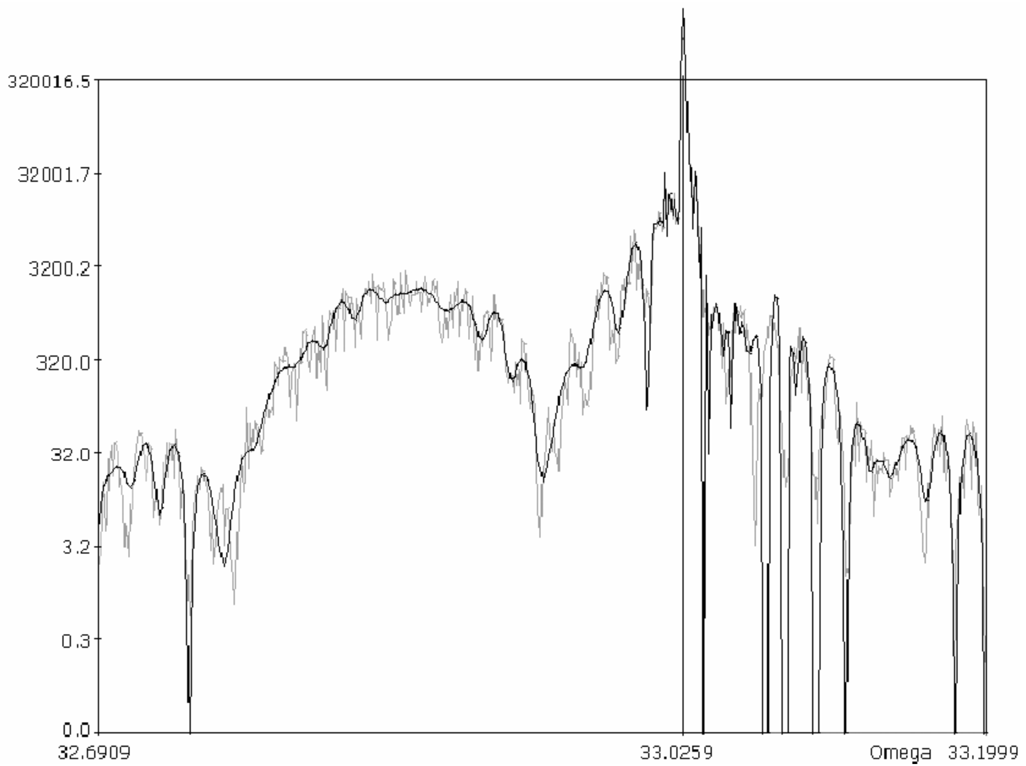

Fig. 10. Rocking curves of quantum well of GaAs/In$_x$Ga$_{1-x}$As/GaAs (x = 0.034) randomly noised (grey line) and the same curve after wavelet analysis (black line)

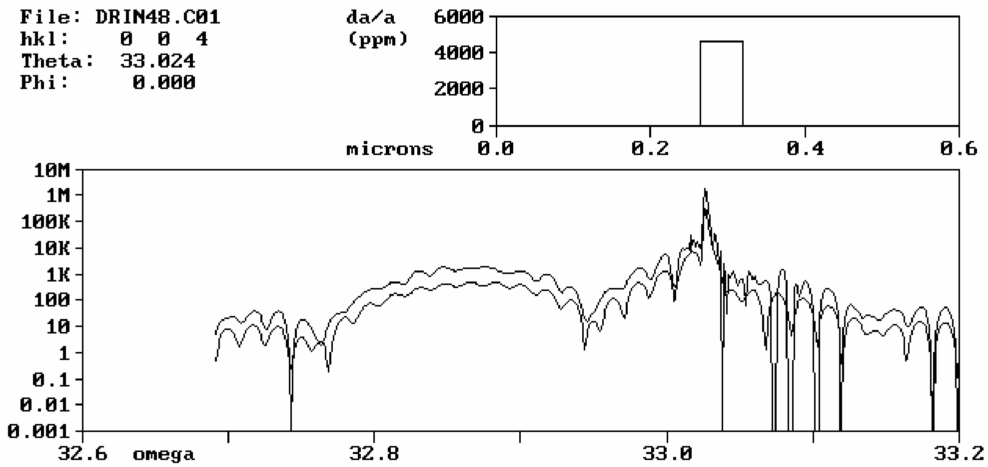

Fig. 11. Rocking curves of quantum well of GaAs/In$_x$Ga$_{1-x}$As/GaAs (x = 0.034) calculated (lower line) and denoised after wavelet analysis (upper line)

$$t = \frac{\lambda \sin \varepsilon}{\Delta\theta \sin 2\theta} \tag{5}$$

where: t – thickness of the layer [Å], λ – X-ray wavelength [Å], ε – angle between the diffracted beam and the wafer surface [rad], θ – Bragg angle of the used reflection, $\Delta\theta$ – angle space between neighbouring fringes [rad].

Similar information can be obtained after a much longer time of scan (Fig. 4c) (2.85 sec/step). Additionally, the picture obtained from the SEM (Fig. 3) confirms the calculated thickness of the AlN buffer layer.

The next structure tested (QW) was examined on the basis of (004) RSM. Figure 5 shows the maps obtained in 1 h, 1 h after wavelet analysis and measured for 15 h. This example once again proves that it is possible to save time of measurements when the wavelet shrinkage based noise reduction is used. The details which can be observed in the denoised images are exactly the same as those in the long-time scan. The distance between the nearest interference peaks in both cases (Fig. 5b, c) is equal to 0.035° in 2 theta scale.

Figures 6–9 show the rocking curves obtained for quantum wells of GaAs (0.26 μm)/$In_xGa_{1-x}As$ (0.0421 μm, x = 0.083)/GaAs (0.235 μm) and GaAs (0.25 μm) /$In_xGa_{1-x}As$ (0.045 μm, x=0.044) /GaAs (0.277 μm), respectively. It can be seen that after the denoising procedure many more details appear which are confirmed by the theoretical calculations realized using the Takagi–Taupin equations (Figs. 7, 9).

Finally, the procedure described above was employed to denoise simulated curves obtained by superimposing a noise from a random generator onto theoretical rocking curves (Fig. 10) and the curve obtained was compared with the input curve (Fig. 11). The test also confirmed that the proposed denoising method gives credible information.

5. Conclusions

The wavelet transform was applied to the analysis of epitaxial layers of high resolution X-ray diffraction images. Rocking curves as well as reciprocal space maps were examined using the method described. It has been shown that the transformed X-ray image yields much more information about the crystallographic structure, than raw picture obtained directly from the measurements. E.g. thickness of the layer, gradient of the lattice parameters and theirs discontinuities can be obtained in this way. Particularly, the method proposed seems to be promising for the layers having large lattice mismatch with respect to substrate. All maps were visualized using OpenGL Technology. The method proposed allows a significant saving the time of measurements.

References

[1] DAUBECHIES I., Commun. Pure Appl. Math., 41 (1988), 909.
[2] MALLAT S., IEEE Trans. Pattern Anal. Machine Intel., 11 (1989), 674.

[3] DONOHO D., JOHNSTONE I., Biometrica, 91 (1994), 429.
[4] DAUBECHIES I., *Ten Lectures on Wavelets*, SIAM, Philadelphia, 1992.
[5] NASON G., *Choice of the threshold parameter in wavelet function estimation*, [in:] A. Antoniadis and G. Oppenheim (Eds.), *Wavelets and statistics,* Lecture Notes in Statistics 103, Springer, New York, 1995, p. 261.
[6] MISITI M., MISITI Y., OPPENHEIM G., POGGI J.M., *Wavelet Toolbox User's Guide*, The MathWorks Inc., Natick, 1996.
[7] PADUANO Q., WEYBURNE D., Jpn. J. Appl. Phys., 42 (2003), 1.
[8] FEWSTER P.F., Semicond. Sci. Technol., 8 (1993), 1915.

Received 28 June 2003
Revised 24 August 2003

Materials Science, *Vol. 21*, *No. 3*, *2003*

Hydrogenation process of Gd_3Ni

NATALYA V. TRISTAN[1], TOMASZ PALEWSKI[1*],
HENRYK DRULIS[2], LUCYNA FOLCIK[2], SERGEY A. NIKITIN[1, 3]

[1]International Laboratory of High Magnetic Fields and Low Temperature,
95 Gajowicka St, 53-421 Wrocław, Poland

[2]Institute of Low Temperature and Structure Research, 2 Okólna St, 50-950 Wrocław, Poland

[3]Faculty of Physics, Moscow State University, Vorobievy Gory, 119899 Moscow, Russia

Reaction of intermetallic Gd_3Ni with hydrogen and transformation of the crystal structure depending on hydrogen concentration is investigated. It is shown that Gd_3Ni belongs to the group of intermetallic compounds which are thermodynamically unstable during hydrogenation and undergo a decomposition into the rare earth hydride and the transition metal. Nickel plays a role of the catalyst in the reaction and supports the formation of GdH_3 at low temperatures.

Key words: *$(Gd_3Ni)H_x$; hydrogenation; structural transformation; structural instability*

1. Introduction

It is well known that many rare earth intermetallic compounds absorb large amounts of hydrogen. The incorporation of hydrogen into the crystal lattice usually gives rise to an increase of the unit cell volume. Besides, a charge transfer between the hydrogen atom and other atoms in the lattice is possible. Combination of such factors results in drastic changes of the physical properties of the hydrogenated intermetallic compounds. Thus, for example, cases are known where a diamagnet becomes a ferromagnet or an electronic conductor turns into an insulator [1]. All these features make the study of hydride phases very interesting and prospective.

The outcome of the reaction of intermetallic compounds with hydrogen is not always predictable. Usual is the situation when the hydrides have the same crystal structure as the parent intermetallic compounds. On the other hand, in numerous cases the hydrides

*Corresponding author, e-mail: paltom@alpha.mlspmint.pan.wroc.pl.

become amorphous or form new crystal structures. Decomposition of the parent intermetallic compound to components of completely different stoichiometries has also been reported [2, 3].

Compounds of the R_3M stoichiometry, where R is a rare earth atom and M is Ni or Co, are able to absorb up to about 9 hydrogen atoms per formula unit [4]. It was suggested that the hydrogenation under low pressures (< 100 kPa) and at low temperatures (243–253 K) could lead to the synthesis of the R_3NiH_x compounds which preserve the crystal structure of the initial intermetallic compound [5, 6]. Our recent investigations show, however, that the previous chemical syntheses and the analysis of the X-ray patterns have not been accurate enough and, therefore, more precise measurements and analysis should be undertaken.

The purpose of the present work was to investigate the reaction of the intermetallic compound Gd_3Ni with hydrogen and to obtain accurate information on the transformation of the crystal structure in function of the amount of absorbed hydrogen.

2. Experimental

The parent Gd_3Ni compound was obtained by high-frequency melting of the constituent metals in a purified argon atmosphere under the pressure of 1.5 atm followed by cooling at the rate of ~1–2 K/sec. The purities of gadolinium and nickel were 99.9 and 99.99%, respectively. Hydrogen used for the syntheses was obtained by thermal decomposition of a $LaNi_5$ hydrogen storage.

The hydrogenation was performed at room temperature under a low hydrogen pressure. Before hydrogenation, all Gd_3Ni samples were powdered and heated under vacuum at 695 K for 2 h. Hydrogen was let into the working volume at room temperature in small portions (p ~ 1–4 kPa) in order to avoid a violent reaction between the powdered sample and the gas. After the whole amount of hydrogen had been absorbed, the samples were homogenized at room temperature for about 60 h. The concentration of the absorbed hydrogen was calculated volumetrically. Some hydride samples were synthesized at low temperature; X-ray diffraction patterns of these samples were similar to the patterns of samples synthesized at room temperature. The former patterns, however, exhibited significant distortions typical of insufficiently annealed compounds.

The X–ray measurements were carried out using a DRON–2 diffractometer with a cobalt radiation source. An additional verification of the elemental composition of each sample was performed using the EDAX 9800 and Philips SEM515 sets.

3. Results and discussion

The X-ray diffraction pattern of the parent powdered Gd_3Ni sample is shown in Fig. 1a. It is a single phase sample crystallizing in an orthorhombic Fe_3C-type structure (the *Pnma* space group) with the lattice parameters a = 0.694 nm, b = 0.969 nm and c = 0.635 nm.

Using the step-by-step hydrogenation procedure, we obtained a number of hydride samples with various compositions $(Gd_3Ni)H_x$, where $0 \leq x \leq 8.8$. The X-ray diffraction patterns of some of the hydrides obtained are shown in Figs. 1b–f. One can see that insertion of a small amount of hydrogen (Fig. 1b) leads to diminishing of the intensities of the lines corresponding to the Gd_3Ni and to appearance of a few new peaks, their intensities increasing with the hydrogen concentration. When, on average, four hydrogen atoms per formula unit are absorbed by the sample, the initial X-ray pattern of orthorhombic structure totally disappears from the diffractogram and only the lines characteristic of a cubic crystal lattice structure remain (see Fig. 1c). When the hydrogenation process is continued and a larger amount of hydrogen is absorbed, another crystallographic transformation takes place and a few new peaks appear in addition to the peaks of the cubic diffraction pattern (Fig. 1d). Their intensities increase with increasing hydrogen concentration while intensities of the peaks belonging to cubic structure weaken (see Figs. 1e–f).

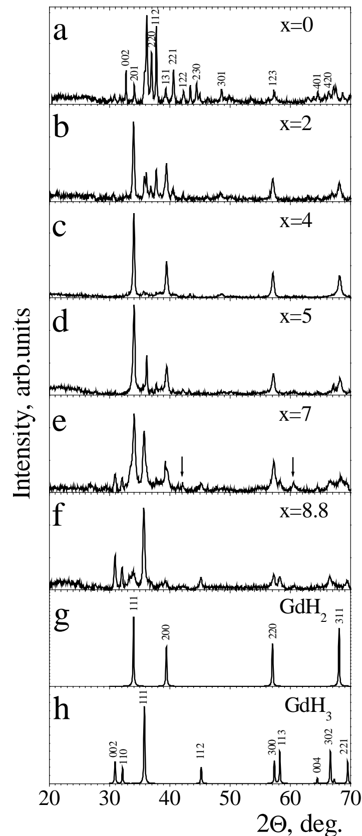

Fig. 1. X-ray diffraction patterns of the parent Gd3Ni compound (a), of hydrides $(Gd_3Ni)H_x$ with different hydrogen concentrations (b–f) and theoretical X-ray diffraction patterns for GdH_2 (g) and GdH_3 (h). The arrows in Fig. 1e indicate peaks of the "intermediate" phase (see the text for explanation)

Let us focus on some X-ray diffraction patterns obtained. First, the cubic structure, shown in Fig. 1c, has a lattice parameter a = 0.530 nm, what is in exact agreement with the value expected of the dihydride GdH_2 [7]. Secondly, the pattern structure shown in Fig. 1f can describe a two-phase equilibrium region. There are ~70% of the hexagonal phase, with the lattice parameters a = 0.646 nm and c = 0.671 nm, corresponding to GdH_3 [7], and ~25% of cubic $GdH_{2+\delta}$ dihydride phase with the lattice parameter a ranging between ca. 0.530 and ca. 0.550 nm. To support our analysis, theoretical diagrams for both GdH_2 and GdH_3 phases are presented in Figs. 1g, h, respectively.

X-ray diffraction patterns of $(Gd_3Ni)H_x$ compounds with $5 \leq x \leq 7$ (Figs. 1d–e) contain a few peaks which belong to neither parent compound Gd_3Ni nor to GdH_x (x = 2, 3) hydrides. A few diffraction peaks belonging to this "intermediate" phase are marked with arrows in Fig. 1e. The low intensity of the peak does not allow us to identify the phase and we could only speculate that it might be a solid solution of hydrogen in

Gd_3Ni or in any of Gd–Ni alloys which possibly could be formed in the process of the decomposition of the parent compound.

Another interesting finding is that the X-ray diffraction patterns do not contain any traces of the diffraction lines corresponding to crystalline nickel nor to any known crystalline alloys of nickel with gadolinium. At the same time, the elemental analysis showed that nickel is distributed uniformly with no visible precipitation. These facts incline us to suppose that nickel transforms to a dispersed phase not detectable in the reported X-ray experiments.

For the sake of completeness, an X-ray diffraction pattern of a sample synthesized at T = 220 K with the maximal hydrogen concentration x = 8.8, is presented in Fig. 2. One can find that at least three phases, GdH_2, GdH_3 and an unidentified "intermediate" phase, are present in this case. As was already mentioned, the X-ray pattern exhibits significant distortions typical of insufficiently annealed or partially amorphous compounds.

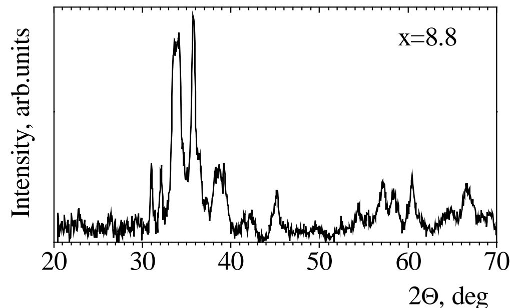

Fig. 2. X-ray diffraction pattern of a $(Gd_3Ni)H_{8.8}$ sample with the highest available hydrogen concentration per formula unit, obtained by hydrogenation at low temperature T = 220 K without homogenization at room temperature

Summarizing the results described above, we conclude that Gd_3Ni belongs to the group of intermetallic compounds which are thermodynamically unstable in the hydrogenation process undergoing the decomposition into the pure rare earth hydride phases with precipitation of the transition metal (Ni) as a dispersed phase:

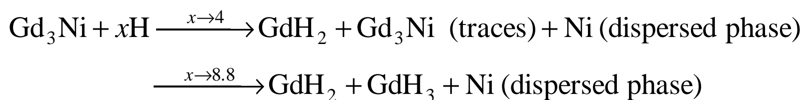

$$\mathrm{Gd_3Ni} + x\mathrm{H} \xrightarrow{x\to 4} \mathrm{GdH_2} + \mathrm{Gd_3Ni}\ \text{(traces)} + \mathrm{Ni}\ \text{(dispersed phase)}$$

$$\xrightarrow{x\to 8.8} \mathrm{GdH_2} + \mathrm{GdH_3} + \mathrm{Ni}\ \text{(dispersed phase)}$$

Considering the observed reaction kinetics, it is obvious that metallic nickel plays the role of a catalyst in the formation of GdH_3 at low temperatures, since usually this hydride can be synthesized only at the temperature higher than room temperature [8, 9].

4. Conclusion

On the basis of the results presented we can state that it is impossible to synthesize the Gd_3Ni hydride in a standard reaction procedure between gaseous hydrogen and Gd_3Ni. Unfortunately, our previous conclusion concerning the crystal structure of hydride samples [5, 6] was based on incorrect interpretation of the X-ray diffraction patterns for $(Gd_3Ni)H_{8.5}$ hydride obtained at low temperature.

Acknowledgements

The authors wish to thank Prof. R. Horyń for his support in the X-ray measurements, Dr. M. Walcyrz for the diffraction analysis software and useful discussions, Mr. K. Nierzewski for help with the elements analysis of the samples (they are all from the Institute of Low Temperature and Structure Research of the Polish Academy of Sciences, Wroclaw, Poland) and Dr. K. Skokov (Tver State University, Russia) for the preparation of the parent Gd_3Ni.

References

[1] SHENOY G.K., SCHUTTLER B., VICCARO P.J., NIARCHOS D., J. Less Common Met., 94 (1983), 37.
[2] BURZO E., KIRCHMAYER H.R., *Magnetic Properties of Metals*, [in:] H.P.J. Wijn (Ed.), *Landolt-Börnstein Numerical Data and Functional Relationships in Science and Technology*, New Series III/19d2, Springer, Berlin, 1990, p. 469.
[3] WIESINGER G., HILSCHER G., *Magnetism of Hydrides*, [in:] K.H.J. Buschow (Ed.), *Handbook of Magnetic Materials*, North Holland, Amsterdam, 1991, Vol. 6, p. 511.
[4] BUSCHOW K.H.J., SHERWOOD R.C., J. Appl. Phys., 49 (1978), 1480.
[5] NIKITIN S.A., VERBETSKY V.N., OVCHENKOV E.A., SALAMOVA A.A., Int J. Hydrogen Energy, 22 (1997), 255.
[6] NIKITIN S.A., TRISTAN N.V., PALEWSKI T., SKOURSKI YU.V., NENKOV K., VERBETSKY V.N., SALAMOVA A.A., J. Alloys Comp., 314 (2001), 22.
[7] ECKERLIN P., KANDLER H., *Structure Data of Elements and Intermetallic Phases*, [in:] K.-H. Hellwege, A.M. Hellwege (Eds.), *Landolt-Börnstein Numerical Data and Functional Relationships in Science and Technology*, New Series III/6, Berlin, 1971, p. 143.
[8] ŻOGAL O.J., J. Less Common Met., 130 (1987), 187.
[9] BRILL M., HALEVY I., KIMMEL G., MINTZ M.H., BLOCH J., J. Alloys Comp., 93 (2002), 330.

Received 8 May 2003
Revised 14 July 2003